Fakultät für Physik und Astronomie

Ruprecht-Karls-Universität Heidelberg

Diplomarbeit
im Studiengang Physik

vorgelegt von
Jonas Binding
aus Heidelberg

2008

Adaptive Optik in der Zwei-Photonen-Mikroskopie

Die Diplomarbeit wurde von Jonas Binding
am Max-Planck-Institut für medizinische Forschung
unter der Betreuung von
Herrn Prof. Dr. Winfried Denk
ausgeführt.

ZUSAMMENFASSUNG

Adaptive Optik in der Zwei-Photonen-Mikroskopie

Adaptive Optik wird in der Astronomie, in der Augenheilkunde und anderen Gebieten erfolgreich eingesetzt. Die Technik scheint auch für die Lichtmikroskopie vielversprechend, jedoch wurde die Relevanz von Aberrationen für viele biologische Proben noch nicht untersucht. Um die Bedeutung der adaptiven Optik für in-vivo Zwei-Photonen-Kalzium-Bildgebung in tiefen Kortexschichten im Nagergehirn abzuschätzen, wurden die von der Probe verursachten Aberrationen mittels Raytracing berechnet, und der sich ergebende Signalverlust abgeschätzt. Astigmatismus sowie die beiden niedrigsten Ordnungen der sphärischen Aberration stellten sich als dominant heraus; ihre Korrektur sollte das Fluoreszenzsignal erhöhen.

Um diese theoretischen Ergebnisse zu überprüfen, wurden ein deformierbarer Spiegel und ein Wellenfrontsensor in ein Zwei-Photonen-Mikroskop integriert. Die Charakterisierung des Systems ergab, dass sich Wellenfronten im notwendigen Bereich mit einem RMS-Fehler von $\lambda/25$ produzieren lassen, wenngleich der Betrieb als offener Regelkreis während der Zwei-Photonen-Mikroskopie noch Verbesserungen bedarf. Beim Mikroskopieren von Proben, die starke Aberrationen verursachen, werden durch die adaptive Optik Signalzunahmen von bis zu 150% erzielt; vollständige Korrektur der Aberrationen war jedoch nicht möglich. Höchste Fluoreszenzintensität wird bei Zernike-Koeffizienten beobachtet, die deutlich unter den theoretisch vorhergesagten Werten liegen. Mögliche Gründe für diese Diskrepanz werden diskutiert.

ABSTRACT

Adaptive Optics in Two-Photon Microscopy

Adaptive optics is successfully being used in astronomy, ophtamology and other fields. The technique holds promise also for optical microscopy, but the role aberrations play in many biological samples has not yet been determined. To estimate the relevance of adaptive optics for deep in-vivo two-photon calcium imaging in the rodent brain, the sample-induced aberrations were calculated using geometrical ray-tracing and the resulting signal loss was estimated. It was found that astigmatism and two orders of spherical aberration should dominate, and that their correction would increase the fluorescence signal.

To test these theoretical results, a deformable mirror and a wavefront sensor were integrated into a custom-designed two-photon microscope. Characterization of the system shows the ability to produce wavefronts in the necessary range with a residual RMS error of $\lambda/25$, but open-loop operation during two-photon imaging still requires some improvements. When imaging in strongly aberrating samples, signal improvements of up to 150% are achieved, but complete compensation of the aberrations was not possible. Peak intensities are found at Zernike coefficients that were substantially smaller than predicted by calculations. Possible reasons for the discrepancy are discussed.

Contents

1. Introduction

There is an increasing number of topics in biology where significant advances in research are based on improvements in observation techniques, oftentimes probing the boundaries of what is physically possible in a given biological context. In many of these cases, a detailed understanding of the underlying physics is crucial to the development of such observation techniques. This is the point where cooperation between physicists and biologists seems to have the most potential: to develop methods to get the most information possible out of a given system.

To understand information processing in the mammalian brain, information about neuronal activity in many parts of the brain is likely to be crucial. Neuronal circuits are thought to exist on several different scales, all of which are potentially interesting. Invasive studies have the ability to look at arbitrary areas of the brain but are hampered by the damage they do to the tissue they intend to observe.

Therefore, one interesting line of research goes towards trying to “see” as much as possible about neuronal activity without interfering with the normal functioning of the brain by slicing it or cutting holes into it.

Two photon fluorescence microscopy[13] has increased penetration depth into unperturbed biological tissue to $500\,\mu$m with conventional Ti:Sa lasers and is routinely used for measuring neuronal activity using Ca^{+2} imaging. The possibility to reach depths as large as $1000\,\mu$m has been demonstrated[40], but has not been used for calcium imaging so far. Investigations of the fundamental imaging-depth limit in two-photon microscopy[39] suggest that a given staining fraction will always limit imaging depth due to near-surface fluorescence generation. However, effects of refractive index mismatch were neglected in these studies.

Mismatch of refractive index between the objective’s intended immersion medium and the sample can lead to significant deterioration of image quality and, in two-photon imaging, signal level. Such sample-induced aberrations could potentially be corrected by the use of adaptive optics. For a recent and rather helpful review on adaptive optics in microscopy, see [5].

In some biological microscopy applications, signal and resolution improvements through adaptive optics have already been demonstrated[33]. The question remains whether the in-focus signal in two-photon fluorescence microscopy of the mammalian brain is significantly reduced by aberrations. If so, implementation of an adaptive optics system into a deep imaging setup could further improve the penetration depth, making a larger part of the cortex accessible to calcium imaging. Specifically, correction of specimen-induced aberrations would increase the signal-level at a given depth, while leaving the near-surface background constant. This increase in S/N ratio would effectively push the experimental penetration depth towards the limit discussed in [39].

The aim of this diploma thesis was to integrate adaptive optics into a two-photon microscope suitable for deep imaging and to evaluate experimentally and theoretically the improvements which can be expected from such a system for thick biological samples, such as intact brains of rodents.

In chapter two, some theoretical results are presented, arguing that deep imaging (defined here as depths beyond 800 μm or 4 mean free path lengths in brain tissue) should indeed be affected by specimen-induced aberrations. It is also argued that a large part of the aberrations should have low spatial frequencies. Therefore, static (relative to the scan time of a single image frame) correction of these low spatial frequency modes without correcting any field-dependent components is a reasonable first step.

The third chapter is concerned with the experimental setup used, basically explaining the integration of a deformable mirror, a wavefront sensor and the interface electronics to a two-photon microscope.

Chapter four describes the different software components that are necessary to operate the setup and which allow flexible wavefront control during animal experiments as well as on-line and off-line data analysis.

Measurements in different phantoms are presented in the following chapter, illustrating the capabilities of correcting low order aberrations likely to be relevant in in-vivo brain imaging.

The concluding chapter discusses the results obtained and the directions in which to continue.

2. Theory

Signal strength in nonlinear microscopy depends strongly on the spatial and temporal structure of the excitation light(Denk et al. in [29], pp.535-538). To maximize the fluorescence excitation in two-photon imaging for constant average power, temporal and spatial focusing is therefore important.

While the temporal profile of the illumination is mainly affected by group velocity dispersion in glass elements along the beam path, the spatial profile at the focus can depend not only on the optical setup, but also on the sample. This has been described in detail for aqueous samples in combination with high-NA oil-immersion objectives [7, 19, 26].

For biological samples with water immersion objectives, the effect of refractive index mismatch has so far usually been neglected[39]. However, figure 3 of [7] suggests a quadratic increase in signal loss with increasing depth in index-mismatched samples. Therefore, even a small mismatche in refractive index causes a significant decrease in two-photon fluorescence signal if measurements are done at greater and greater depths.

The aim of this chapter is to estimate the expected aberrations for 2P imaging in a depth of $1000\,\mu$m in the mouse cortex with a high NA long working distance water immersion objective (A NA 1.0 was used in numerical calculations and experiments). The resulting decrease in signal should also be estimated. This will give an indication which amount of signal improvement can be expected in this system from the implementation of adaptive optics. Furthermore, the dynamic range that a wavefront correction element would need to preempt these aberrations is thereby established.

As detailed in the following section, different brain geometries will be discussed. For the rotationally symmetric geometries (flat and spherical brain surface), an integral formula for the wavefront is derived. For the flat case, it can be solved algebraically and reduces to a generalization of two formulae found in the literature. For the spherical case, no closed form could be obtained, but numerical solutions are presented.

For the cylindrical and general ellipsoidal geometries, two-dimensional ray-tracing is not sufficient to estimate the wavefront to the desired order. Therefore, 3D-ray tracing with Optica3 (Optica Software, Champaign, USA) for a simplified model of the objective was performed. The results were shown to agree to within about 13% with the results for the more complete objective model for the flat case, and give an order-of-magnitude estimate for astigmatism and spherical aberration.

2.1. Mouse Brain: Refractive Index and Geometry

For all of these calculations, a reliable value for the refractive index of brain tissue is necessary. While several methods for measuring the refractive index of biological samples have been proposed over the last twenty years [2, 20, 37], only few results specifically for brain tissue are available, which are summarized in table 2.1. The spatial variability of refractive index in the brain can be estimated from figure 1c of [21], yielding a range of $\Delta n = 0.02$[1], roughly symmetric around the mean.

In summary, the best guess for brain refractive index is $n = 1.37 \pm .01$, where the latter value characterizes the expected variability within the tissue. Since this variability is a factor of 4 smaller than the difference of the average brain refractive index to the refractive index of the immersion medium (essentially water, $n = 1.333$, with changes due to physiological amounts of solutes only at the fourth decimal), the variability will be completely neglected in the following study.

Given the assumption of a homogeneous refractive index of $n = 1.37$ for the brain, the only aberrations are introduced at the surface of the brain. The geometry of this surface was estimated from a brain atlas [18]. On the relevant length scale of 2 mm (corresponding to the surface spot diameter of excitation light focused at 1 mm depth inside the brain with an angular aperture of roughly 45°, as is the case for a NA 1.0 water immersion objective), the cortex surface can be approximated by an ellipsoidal surface. When viewed in coronal sections, it appears to have a radius of curvature of about 5 mm, while sagittal sections show a radius of curvature well above 20 mm.

Of course, the curvature can be significantly increased by swelling in open-skull preparations. Thin-skull preparation, on the other hand, will avoid swelling of the brain, but suffer from additional aberrations created by the remaining skull

---

[1] The FWHM $\Delta\varphi_{cer}$ of the cerebrum phase histogram of figure 1c of [21] is approximately 1/3 of the difference $\bar{\varphi} = \bar{\varphi}_{cer} - \bar{\varphi}_{PBS}$ between the mean values of both histograms. Using the equation $\bar{n} = (\bar{\varphi}/2\pi)(\lambda/h) + n_{PBS}$ given in the text, $\Delta n = 1/3 * (n - n_{PBS}) = 0.02$.

Table 2.1. – measurements of refractive index of brain tissue from different literature sources

Sample	**n**	**Source**
human brain, gray matter	1.36	[24], cited in [44]
human brain, white matter	1.38	ibid.
human brain, white and gray	1.37	ibid.
mouse brain slice (5 μm, fixed)	$1.368 \pm .007$	figure 2f of [21]; figure 2a of the same reference, stating a slightly larger value, is a misprint (Gabriel Popescu, private communication)
mouse cortical neurons in culture (2 cells)	1.3751/1.3847	[30]

layer (refractive index $n = 1.5...1.6$;[1]) and dura mater. Neither effect will be considered here.

Consequently, the most complicated geometry treated will be an ellipsoidal refracting surface representing the brain, with inner refractive index of $n = 1.37$ and radii of curvature of 5 mm and 20 mm(figure 2.1). As extreme cases, the flat, cylindrical and spherical brain geometries will also be discussed.

2.2. Assuming the sine condition (and defining notation)

In order to calculate the optimal wavefront for a given geometry, the behavior of the objective has to be known. Since no detailed information about the inner design of the objectives was available, the objective was assumed to follow the sine condition. Specifically, in figure 2.2, the destination (radial position) in the back focal plane (BFP) for a ray leaving the focus under the angle α_{IMM} to the optical axis is given by

$$r = f n_{IMM} \sin \alpha_{IMM}. \tag{2.1}$$

Generally, quantities with index IMM correspond to the immersion medium water, while quantities with index SMP correspond to the sample. For a point in the focal plane with a distance x_N to the optical axis, all rays will be tilted in the BFP by an angle θ, with

$$\begin{aligned} \tan \theta' &= \frac{x_N}{f n_{IMM}} \\ n_{IMM} \sin \theta' &= \sin \theta \\ \Rightarrow \tan \theta &\approx \frac{x_N}{f} \end{aligned} \tag{2.2}$$

where f is the focal length of the objective (in air) and $x_N \ll f$ has been used.

The origin of the coordinate system will later coincide with the apex of the sample.

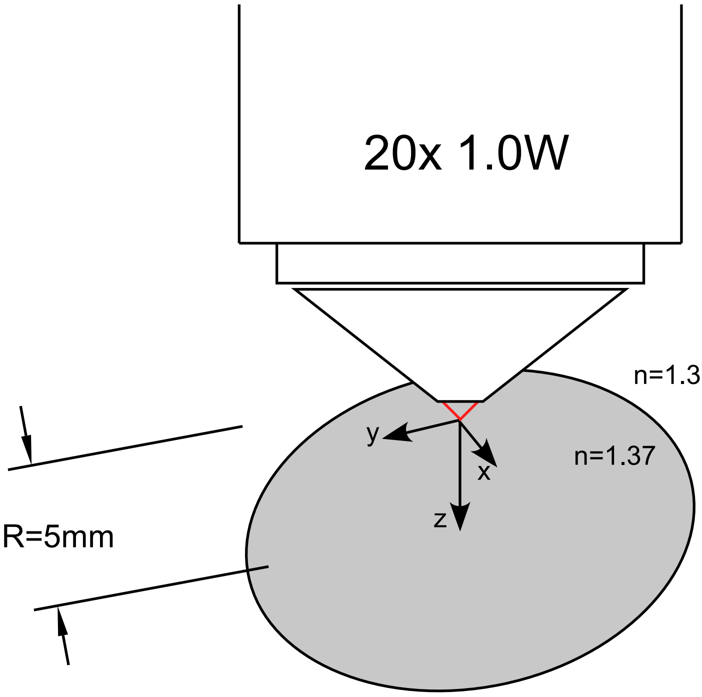

Figure 2.1. – The rodent brain is modeled as an ellipsoid with refractive index n=1.37

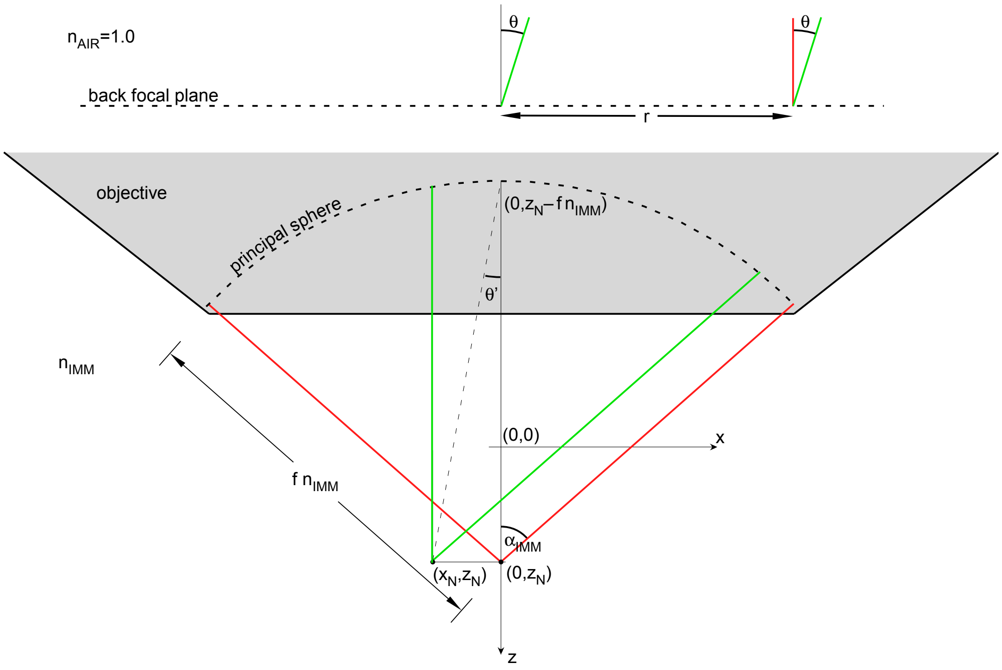

Figure 2.2. – Assumptions made about the objective - essentially the Sine condition.

The focus in the aberration-free case is at the so-called nominal focus position (NFP) with the coordinates $(0, z_N)$. A sample with refractive index mismatch and/or a non-planar incoming wavefront move the focus to the so-called actual focus position (AFP) with the coordinates $(0, z_A)$.

2.3. Ray tracing in 2D

2.3.1. Spherical brain surface

With all the simplifications mentioned above and the notation established in the previous section, we can now start to calculate the actual wavefront for a spherical brain surface. Since the whole system (objective and sample) exhibits rotational symmetry, restriction to the meridional plane is sufficient. The approach will be as follows: to determine the wavefront which will produce a diffraction limited focus at an actual focus position $(0, z_A)$ on the optical axis, we imagine a point source at this position and trace its rays into the back focal plane.

This corresponds to a plane wave expansion of the emanating field; the rays in the back focal plane will therefore be orthogonal to the tangent of the local wavefront at that position. The complete wavefront in the back focal plane (up to an arbitrary piston term) can then be determined by integrating this local tangent over the radial coordinate.

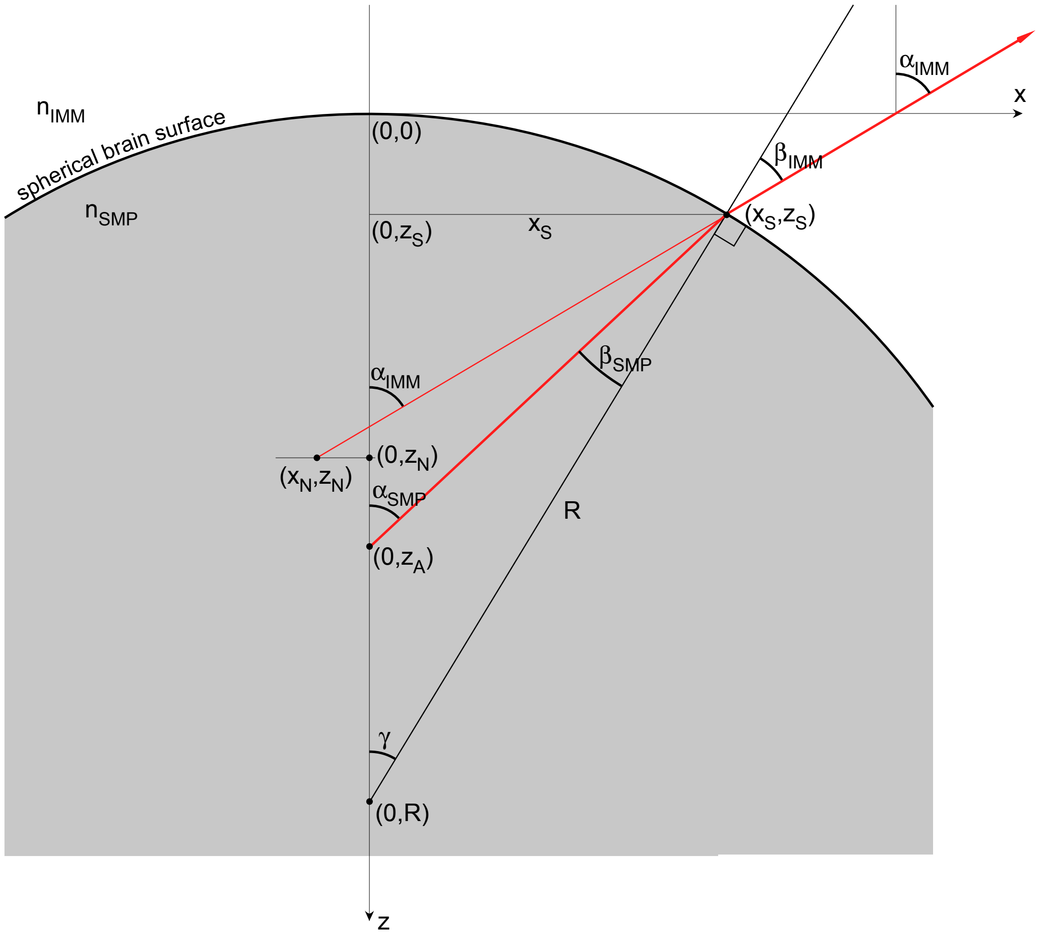

Figure 2.3. – Geometry of schematic for ray tracing. The spherical brain with center at $(0, R)$ refracts a light ray emitted under angle α_{SMP} from the actual focus position $(0, z_A)$ into angle α_{IMM}. This ray is traced back into the nominal focus plane $z = z_N$, where it is found to correspond to point (x_N, z_N).

But first we have to do the actual ray tracing. In figure 2.3 the point source at the AFP inside the sample is shown emitting a light ray in the direction α_{SMP} to the optical axis. It strikes the spherical brain surface under an angle β_{SMP} and gets refracted according to Snellius

$$n_{SMP} \sin \beta_{SMP} = n_{IMM} \sin \beta_{IMM} \tag{2.3}$$

while from geometry we find

$$\alpha_{IMM} = \beta_{IMM} + \gamma \tag{2.4}$$

$$\alpha_{SMP} = \beta_{SMP} + \gamma \tag{2.5}$$

$$\sin \gamma = \frac{x_S}{R} \tag{2.6}$$

$$\tan \alpha_{SMP} = \frac{x_S}{z_A - z_S} \tag{2.7}$$

$$x_N = x_S - (z_N - z_S) \tan \alpha_{IMM} \tag{2.8}$$

[redacted] (2.9)

This system of equations needs to be solved for x_N, expressed in terms of the direction α_{IMM} of the light ray outside the sample and in terms of the parameters n_{SMP}, n_{IMM}, R, z_N and z_A.

Using substitutions to eliminate $\alpha_{SMP}, \beta_{IMM}, \beta_{SMP}, \gamma$ and z_S, we are left with

$$x_N = x_S - \left(z_N - R + \sqrt{R^2 - x_S^2} \right) \tan \alpha_{IMM} \tag{2.10}$$

and

$$\frac{x_S}{z_A - R + \sqrt{R^2 - x_S^2}} = \tan \left\{ \arcsin \frac{x_S}{R} + \arcsin \left[\frac{n_{IMM}}{n_{SMP}} \sin \left(\alpha_{IMM} - \arcsin \frac{x_S}{R} \right) \right] \right\} \tag{2.11}$$

which can only be solved numerically since x_S appears both inside and outside trigonometric functions. Once x_S and thereby x_N is known for a given set of parameters and for a given value of α_{IMM}, this can be translated into a direction θ of the corresponding light ray at radius r in the back focal plane using equations 2.1 and 2.2, see figure 2.2. The wavefront Ψ has the slope

$$\frac{d\Psi}{dr} = -\tan \theta \Rightarrow \frac{d\Psi}{d \sin \alpha_{IMM}} = -n_{IMM} x_N, \tag{2.12}$$

allowing us to determine $\Psi(\rho)$ up to the unimportant constant term (piston) by integration:

$$\begin{aligned}\Psi(\rho) &= \int_0^{\frac{\mathrm{NA}\,\rho}{n_{IMM}}} \frac{d\Psi}{d\sin\alpha_{IMM}} d\sin\alpha_{IMM} \\ &= -n_{IMM}\int_0^{\frac{\mathrm{NA}\,\rho}{n_{IMM}}} \left[x_S - \left(z_N - R + \sqrt{R^2 - x_S^2}\right)\frac{\sin\alpha}{\sqrt{1-\sin^2\alpha}}\right] d\sin\alpha\end{aligned} \tag{2.13}$$

Equation 2.13 has been implemented in Mathematica, using `NIntegrate` for integration and `FindRoot` to solve equation 2.11 for x_S. The wavefront was decomposed into Zernike modes by numerical convolution with the individual Zernike polynomials[28].

2.3.2. A limiting case: flat brain surface

One important limiting case of the geometry treated above is the flat brain surface, i.e. $R \to \infty$. Equation 2.11 then simplifies to

$$\begin{aligned}\frac{x_S}{z_A} &= \tan\left\{\arcsin\left[\frac{n_{IMM}}{n_{SMP}}\sin\alpha_{IMM}\right]\right\} \\ &= \frac{n_{IMM}\sin\alpha_{IMM}}{\sqrt{n_{SMP}^2 - n_{IMM}^2\sin^2\alpha_{IMM}}}\end{aligned} \tag{2.14}$$

which is now trivially solvable for x_S and can be substituted into 2.10 to give a closed form of 2.13:

$$\begin{aligned}\Psi(\rho) &= -n_{IMM}\int_0^{\mathrm{NA}\,\rho/n_{IMM}} \left[z_A\frac{n_{IMM}\sin\alpha}{\sqrt{n_{SMP}^2 - n_{IMM}^2\sin^2\alpha}} - z_N\frac{\sin\alpha}{\sqrt{1-\sin^2\alpha}}\right] d\sin\alpha \\ &= z_A\sqrt{n_{SMP}^2 - \mathrm{NA}^2\rho^2} - z_N\sqrt{n_{IMM}^2 - \mathrm{NA}^2\rho^2} + \mathrm{const}\end{aligned} \tag{2.15}$$

Two special cases of this formula were found in the literature. Equations 5 and 6 of [6] correspond to $z_A = z_N$ (there named d) in 2.15, implying that the focus is kept fixed at the nominal focus position. The case $n_{IMM} = n_{SMP}$ was treated by [17] (equation (3.88)), i.e. the actual focus position was varied, but in an index-matched sample.

In summary, a closed solution for the wavefront is available for a flat surface, while the curved surface can only be solved numerically. For the flat surface, the result presented here generalizes two formulae found in the literature.

2.3.3. Some notes on refocusing

The formula by Feierabend[17] for $n_{IMM} = n_{SMP}$ (see previous section) is rederived by [9], who present it in the context of higher order spherical aberrations caused by moving the focus axially in a sine-condition objective. Their analysis shows that, contrary to statements made in [6], an axial shift of the diffraction limited focus does not, for high NA objectives, correspond to Zernike defocus alone. Instead, it corresponds to a sum of defocus and certain amounts of spherical aberration and all higher order spherical modes; they refer to this sum as “high NA defocus”. Zernike defocus is therefore not completely compensated by refocusing (i.e. moving the objective relative to the sample). Instead, all orders of Zernike spherical aberration have to be modified.

Of course, this argument for the index-matched case also applies to situations with refractive-index mismatch. What does this mean for the calculations presented in [6], where $n_{IMM} \neq n_{SMP}$ but $z_A = z_N$? The aim of their paper was to calculate the amount of signal and resolution that could be regained in a sample with planar refractive index mismatch by compensation of low orders of spherical aberration, while leaving the higher orders uncorrected (corresponding, for example, to correction with a wavefront correction element with limited spatial frequency range).

Their calculation assumes perfect compensation of Zernike defocus (their eq. 15). Since this can not be achieved by refocusing the microscope (different from what is claimed), those calculations are only correct if the wavefront correction element is used for removing Zernike defocus. Because this uses up an unnecessarily high portion of the dynamic range of the correction element, it is preferable to allow refocusing ($z_A \neq z_N$) and to consider the effect it has on the wavefront. Therefore, this is a direct application for the general case of equation 2.15. The free parameter $\Delta z = z_A - z_N$ can, for example, be used to minimize the peak-to-valley wavefront stroke, to minimize the RMS of the wavefront or to set one of the Zernike modes to zero. Since defocus depends a lot more strongly on z_A than the higher modes, setting defocus to zero approximates well the setting for minimized RMS.

As will be shown in the next subsection, refocusing for minimal RMS leads to significantly smaller coefficient values. For example, for a flat brain, comparing equation 2.16 with $\Delta z = 0$ with equation 2.18 shows that spherical aberration is reduced by about 50% while secondary spherical aberration is reduced by 27%. For the refractive indices used in [6], the effect is smaller but still significant, amounting to about 35% and 13% respectively.

2.3.4. Numerical results

All calculations are made for $n_{IMM} = 1.33$, $n_{SMP} = 1.37$ and a numerical aperture (NA) of 1.0. For a spherical brain of 5 mm radius, defocus and the the first two orders of sphercial aberrations were numerically analyzed for depths of up to 1200 μm. Coefficients showed a significant quadratic dependence on actual focus depth, but refocusing entered only linearly:

$$\begin{aligned}
Z5 &\approx 0.038\,\mu\text{m} + 5.180\,\mu\text{m}\frac{z_A}{\text{mm}} - 1.316\,\mu\text{m}(\frac{z_A}{\text{mm}})^2 - 0.130\,\mu\text{m}\frac{\Delta z}{\mu\text{m}}\\
Z13 &\approx 0.018\,\mu\text{m} + 0.705\,\mu\text{m}\frac{z_A}{\text{mm}} - 0.258\,\mu\text{m}(\frac{z_A}{\text{mm}})^2 - 0.007\,\mu\text{m}\frac{\Delta z}{\mu\text{m}}\\
Z25 &\approx 0.005\,\mu\text{m} + 0.102\,\mu\text{m}\frac{z_A}{\text{mm}} - 0.044\,\mu\text{m}(\frac{z_A}{\text{mm}})^2 - 0.001\,\mu\text{m}\frac{\Delta z}{\mu\text{m}}
\end{aligned}$$

For a flat brain, the coefficients depend exactly linearly on both quantities:

$$\begin{aligned}
Z5 &= 5.428\,\mu\text{m}\frac{z_A}{\text{mm}} - 0.130\,\mu\text{m}\frac{\Delta z}{\mu\text{m}}\\
Z13 &= 0.827\,\mu\text{m}\frac{z_A}{\text{mm}} - 0.007\,\mu\text{m}\frac{\Delta z}{\mu\text{m}}\\
Z25 &= 0.137\,\mu\text{m}\frac{z_A}{\text{mm}} - 0.001\,\mu\text{m}\frac{\Delta z}{\mu\text{m}}
\end{aligned} \tag{2.16}$$

Optimizing Δz to minimize RMS wavefront error, the optimal coefficients for a focus in 1000 μm are, for the spherical surface,

$$\begin{aligned} Z5 &= -0.014\,\mu\text{m (defocus)} \\ Z13 &= 0.260\,\mu\text{m (spherical aberration 3rd)} \\ Z25 &= 0.042\,\mu\text{m (spherical aberration 4th)} \end{aligned} \tag{2.17}$$

and for the flat surface

$$\begin{aligned} Z5 &= -0.029\,\mu\text{m (defocus)} \\ Z13 &= 0.540\,\mu\text{m (spherical aberration 3rd)} \\ Z25 &= 0.108\,\mu\text{m (spherical aberration 4th)} \end{aligned} \tag{2.18}$$

– about a factor of two larger. Since the spherical brain surface is curved in the same direction as the converging spherical wavefronts, it causes smaller aberrations than a flat surface. Therefore, the flat brain values can be seen as the maximum values to be expected for this refractive index and depth.

Cover glass

Plane-parallel glass plates are used as cover glass to keep the brain fixed and under pressure in open-skull preparations, even though the objectives used were not designed for the use with a cover glass. Additionally, plane-parallel glass plates are a good way to introduce a defined amount of spherical aberration into the system.

Calculation of aberrations caused by a certain amount of glass is mathematically equivalent to the calculations presented above for aberrations at a certain depth inside a mismatched medium. Even though at first sight two refracting surfaces need to be taken into account for the glass, the result is unchanged. Being parallel, the second refracting surface restores each ray to the direction it had before entering the glass; after leaving the glass, all rays will therefore propagate with a fixed time delay and lateral shift, but without acquiring additional delays relative to each other. Therefore, the previous formulae can be used for this case, where z_A now stands for glass thickness and n_{SMP} for the refractive index of glass (1.51). Per 100 μm glass, a refocusing by 15.4 μm is necessary, optimal Zernike coefficients

$$
\begin{aligned}
Z5 &= -0.009\,\mu\text{m (defocus)}\\
Z13 &= 0.164\,\mu\text{m (spherical aberration 3rd)}\\
Z25 &= 0.029\,\mu\text{m (spherical aberration 4th)}
\end{aligned}
$$

2.4. Geometries without spherical symmetry

Symmetry is a very powerful tool in physics, and we have already used it to treat rotationally symmetric systems by looking at the meridional plane only. For cylindrical and general ellipsoidal brain surfaces, rotational symmetry is broken and only two mirror symmetries are left. We will now analyze to which extend these symmetries are enough to determine the wavefront (WF), expressed by Zernike modes, from ray-tracing in the planes of symmetry only. In the geometry presented in figure 2.1, the mirror symmetries of the system with respect to the x-z and y-z planes correspond to symmetries of the resulting wavefront:

$$WF(x,y) = WF(-x,y) \tag{2.19}$$
$$WF(x,y) = WF(x,-y) \tag{2.20}$$

or, in polar coordinates,

$$WF(\rho,\theta) = WF(\rho,\pi-\theta) \tag{2.21}$$
$$WF(\rho,\theta) = WF(\rho,-\theta) \tag{2.22}$$

This implies that all nonzero Zernike modes (see appendix A) that appear in the expansion of WF must also obey these symmetries. This is true for all $\cos(k\theta)$ terms with $k \in \mathbb{N}$, including the rotationally symmetric terms ($k = 0$). If we neglect terms which have at least ρ^4-dependence, we are left with only Z_5 (defocus) and Z_6 (astigmatism). If we can calculate the wavefront in the x-z and y-z planes, we have enough information to determine the coefficients for these Zernike polynomials, resulting in an exact representation of the 3D wavefront up to second radial order, inferred from wavefront data on the axes.

For a cylindrical surface, the x-z and y-z planes correspond to a spherical and flat geometry, respectively. Using the wavefront data from the previous section for these geometries, Zernike polynomials up to second radial order were fitted. Refocusing allowed to remove the defocus term, while having no influence on the resulting astigmatism:

$$\begin{aligned} Z5 &= 0\,\mu\text{m (defocus)} \\ Z6 &= 0.855\,\mu\text{m (astigmatism)} \end{aligned} \tag{2.23}$$

However, for rotationally symmetric geometries it is well known that Z_{13} (spherical aberration) is actually the main problem, since the defocus term can be compensated relatively well by refocusing, i.e. moving the sample relative to the objective. Since spherical aberration has ρ^4 dependence, we would like to also include this order. However, there are two more terms at this radial order which are not excluded by our symmetry argument, namely Z_{14} and Z_{15} (2nd order astigmatism and quadrafoil).

When restricting the analysis to the axes (x=0 or y=0), where calculations are much simplified, the Zernike modes defocus, quadrafoil and spherical aberration are linearly dependent. In order to separate these terms, information about the off-axis wavefront (i.e. $x \neq 0, y \neq 0$) is needed. Therefore, even when considering lowest order spherical aberration, three-dimensional ray-tracing is needed.

2.4.1. 3D raytracing with Optica3

Three-dimensional ray-tracing for flat, cylindrical and ellipsoidal surfaces was done by Patrick Theer (European Molecular Biology Laboratory, Heidelberg) using Optica3 (Optica Software Inc.). Since no sine-condition objective was available predefined in Optica3, a further simplification was made. Instead of tracing the rays to the back focal plane of the objective, the optical path difference for rays reaching the “front” principal sphere (see figure 2.2) was calculated. This implies ignoring that laterally shifted rays will converge in the back focal plane as long as they reach the principal sphere under the same angle (two rays on the right side of figure 2.2), and instead treating all rays as if they propagated parallel to the optical axis in the objective. This over-simplified model of the objective was used for simplicity, and the results obtained were compared with results from section 2.3.4 to estimate the error made.

Since Optica3 uses a non-standard representation for Zernike modes, results by Theer were converted into standard form using a Mathematica script. The following results were obtained for a depth of 1000 μm and optimal refocus. For a flat surface,

$$\begin{aligned}
Z5 &= -0.033\,\mu\text{m (defocus)}\\
Z6 &= -0.032\,\mu\text{m (spurious astigmatism)}\\
Z13 &= 0.608\,\mu\text{m (spherical aberration 3rd)}\\
Z14 &= 0.0004\,\mu\text{m (spurious secondary astigmatism)}\\
Z15 &= -0.0003\,\mu\text{m (spurious quadrafoil)}\\
Z25 &= 0.115\,\mu\text{m (spherical aberration 4th)}\\
Z26 &= 0.002\,\mu\text{m (spurious tertiary astigmatism)}\\
Z27 &= 0.0001\,\mu\text{m (spurious secondary quadrafoil)}
\end{aligned}$$

contains some amount of astigmatism and quadrafoil even though these coefficients should vanish for symmetry reasons; these entries are therefore marked as "spurious". They indicate that numerical precision is an issue here, and not even the second decimal of these calculations can be trusted. Comparing the values to the "flat brain" values presented in section 2.3.4, deviations of up to 13% are found. This is presumably due to the over-simplification of the treatment of the objective. The results presented below should therefore be considered to be only qualitative.

For a ellipsoidal surface with radii of curvature of 5 mm and 20 mm,

$$\begin{aligned}
Z5 &= -0.02\,\mu\text{m (defocus)}\\
Z6 &= 0.85\,\mu\text{m (astigmatism)}\\
Z13 &= 0.39\,\mu\text{m (spherical aberration 3rd)}\\
Z14 &= -0.13\,\mu\text{m (secondary astigmatism)}\\
Z15 &= -0.02\,\mu\text{m (quadrafoil)}\\
Z25 &= 0.06\,\mu\text{m (spherical aberration 4th)}\\
Z26 &= -0.02\,\mu\text{m (tertiary astigmatism)}\\
Z27 &= 0.00\,\mu\text{m (secondary quadrafoil)}
\end{aligned}$$

which indicates the first two orders of astigmatism together with lowest order spherical aberration dominate the wavefront. Quadrafoil appears about a factor of 20 lower than spherical aberration, even though the exact ratio might be different due to the limited numerical precision of these results.

For a cylindrical surface with radius of curvature of 5 mm,

$$\begin{aligned}
Z5 &= -0.02\,\mu\text{m (defocus)}\\
Z6 &= 1.32\,\mu\text{m (astigmatism)}\\
Z13 &= 0.43\,\mu\text{m (spherical aberration 3rd)}\\
Z14 &= -0.19\,\mu\text{m (secondary astigmatism)}\\
Z15 &= -0.05\,\mu\text{m (quadrafoil)}\\
Z25 &= 0.07\,\mu\text{m (spherical aberration 4th)}\\
Z26 &= -0.04\,\mu\text{m (tertiary astigmatism)}\\
Z27 &= 0.01\,\mu\text{m (secondary quadrafoil).}
\end{aligned}$$

As expected, the values for astigmatism are slightly higher than for the ellipsoidal surface and represent an upper limit on what might be expected. The discrepancy with the calculation presented in equation 2.23 could be due to the systematic error made in the description of the objective in Optica3, as well as the fit error in equation 2.23 caused by the restriction to the lowest order.

2.5. Signal intensity suffers from aberrations

Aberrations cause the point spread function the get wider, decreasing peak fluorescence. For small aberrations ($RMS \ll 1rad$, i.e. $RMS \ll \frac{\lambda}{2\pi} \approx 0.146\,\mu\text{m}$), peak excitation intensity should decrease quadratically with increasing RMS wavefront error $\Delta\Phi$ [8]. Peak excitation efficiency for two-photon excitation should therefore scale as

$$S = (1 - (\frac{2\pi}{\lambda}\Delta\Phi)^2)^2. \tag{2.24}$$

However, for the application in question, aberrations up to one order of magnitude beyond the validity of this approximation were expected. Therefore, point spread functions were calculated for increasing aberrations in all modes up to 6th radial order. A Mathematica script by Markus Rückel implementing the paraxial Debye integral was used for these calculations. Results for peak intensity versus aberration are displayed in figure 2.4. For aberrations below $0.03\,\mu\text{m}$, the peak of the numerical PSF corresponds well to the analytic solution given in Born & Wolf, but already for coefficients in the order of $0.1\,\mu\text{m}$, substantial deviations are found.

Even though peak fluorescence is an important quantity to judge the severity of aberrations, the integrated fluorescence over the whole volume is often easier to measure. Therefore, the integral of the PSFs whose peak values are presented in figure 2.4 are displayed in figure 2.5. It is clear that integrated intensity drops off much slower than peak intensity, and the speed of the drop depends on the aberration mode.

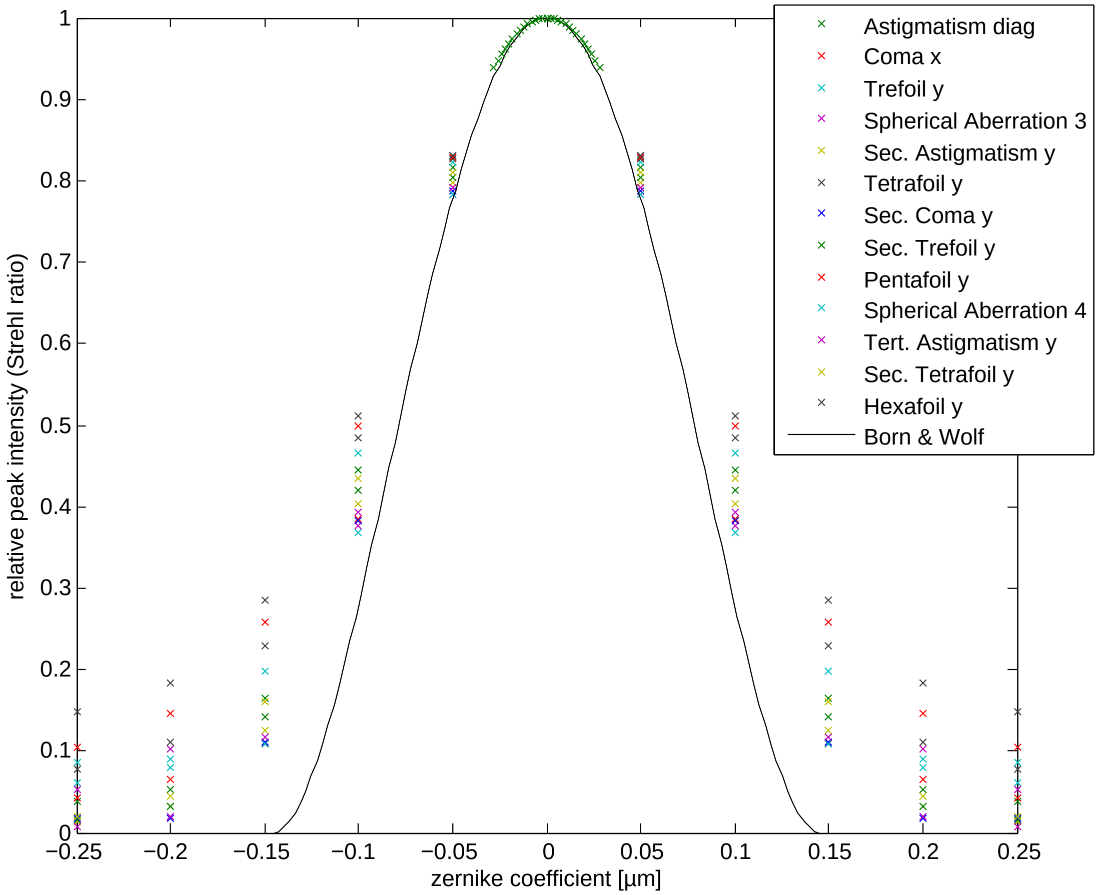

Figure 2.4. – Numerical calculation of peak excitation probability. All Zernike modes up to 6th radial order are shown.

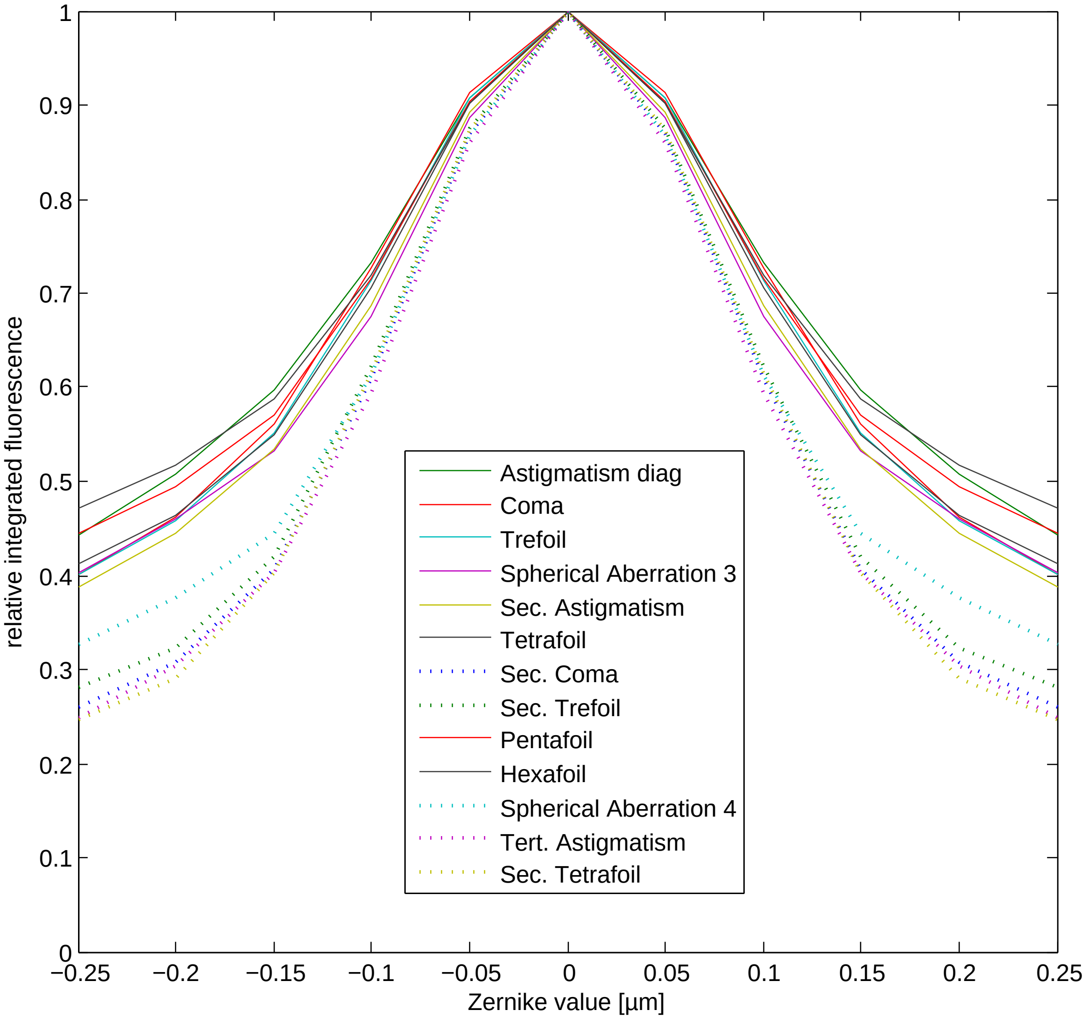

Figure 2.5. – Numerical calculation of spatially integrated excitation probability. All Zernike modes up to 6th radial order are shown.

2.6. Zernike modes are not correctly balanced for large aberrations

While Zernike modes are correctly balanced[2] for small aberrations [8], this must not necessarily be true for larger aberrations. To estimate the size of the effect, point spread functions were calculated for different amounts of spherical aberration, with two higher orders of spherical aberration constant at the values derived in section 2.3.4 ($Z25 = -0.108\,\mu$m, $Z36 = -0.020\,\mu$m). This simulates an experiment where all orders of spherical aberration are introduced by imaging in 1 mm depth inside a flat brain, and lowest order spherical aberration is additionally introduced on the deformable mirror to compensate the aberrations.

Z-profiles of the point-spread functions for different amounts of total lowest order spherical aberration are shown in figure 2.6. It is clear that perfect compensation of the $-0.540\,\mu$m spherical aberration introduced by the sample is not optimal (green solid curve). Instead, some residual negative spherical aberration ($-0.14\,\mu$m, dashed purple curve) is preferable since it compensates to some extend the higher order aberrations present.

Since these theoretical results were obtained after the experiments chapter (chapter 5) had already been finished, they were not taken into account when comparing optimal correction coefficients between experiments and theory. The effect of crosstalk observed here probably explains a large part of the discrepancy between theory and experiment summarized in the table on page 84.

---

[2] Correct balancing here refers to the fact that any aberration basis function of a given order already contains the optimal amount of all lower order aberrations. This implies that no aberration of a fixed order can be compensated (even partially) by introducing lower order aberrations

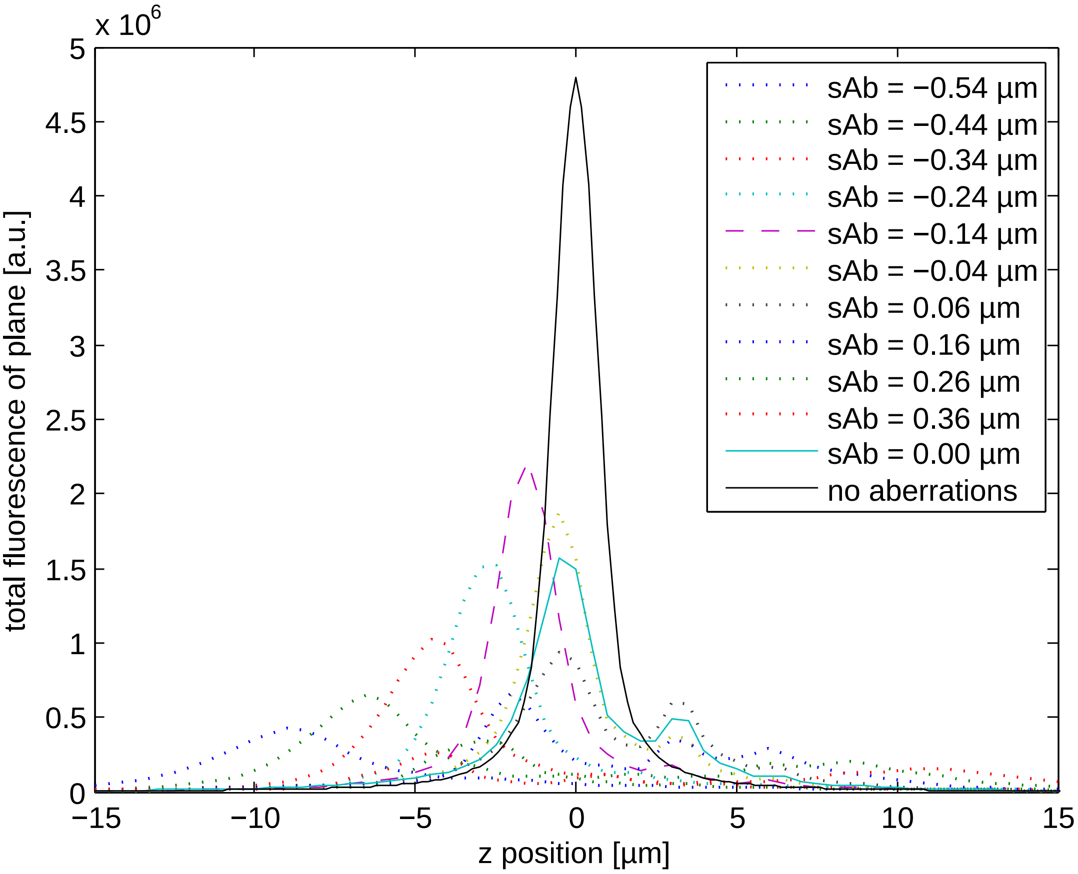

Figure 2.6. – Numerical calculation of laterally integrated excitation probability. Through-focus z-profiles are shown for different amounts of lowest order spherical aberration, while two higher orders of spherical aberration were kept at constant values ($Z25 = -0.108\,\mu$m, $Z36 = -0.020\,\mu$m). The only exception is the black curve (highest peak), which corresponds to the unaberrated PSF. The leftmost blue dotted curve corresponds to $Z5 = -0.540\,\mu$m, $Z25 = -0.108\,\mu$m, $Z36 = -0.020\,\mu$m which are the aberrations calculated for 1 mm depth inside a flat brain. The solid light blue curve corresponds to $Z5 = 0$, i.e. perfect compensation of lowest order spherical aberration. Even though this gives about a factor 3 improvement compared to the unaberrated case, it is not optimal. Even higher peak fluorescence can be reached by slightly under-compensating, see purple dashed curve ($sAb = -0.14\,\mu$m)

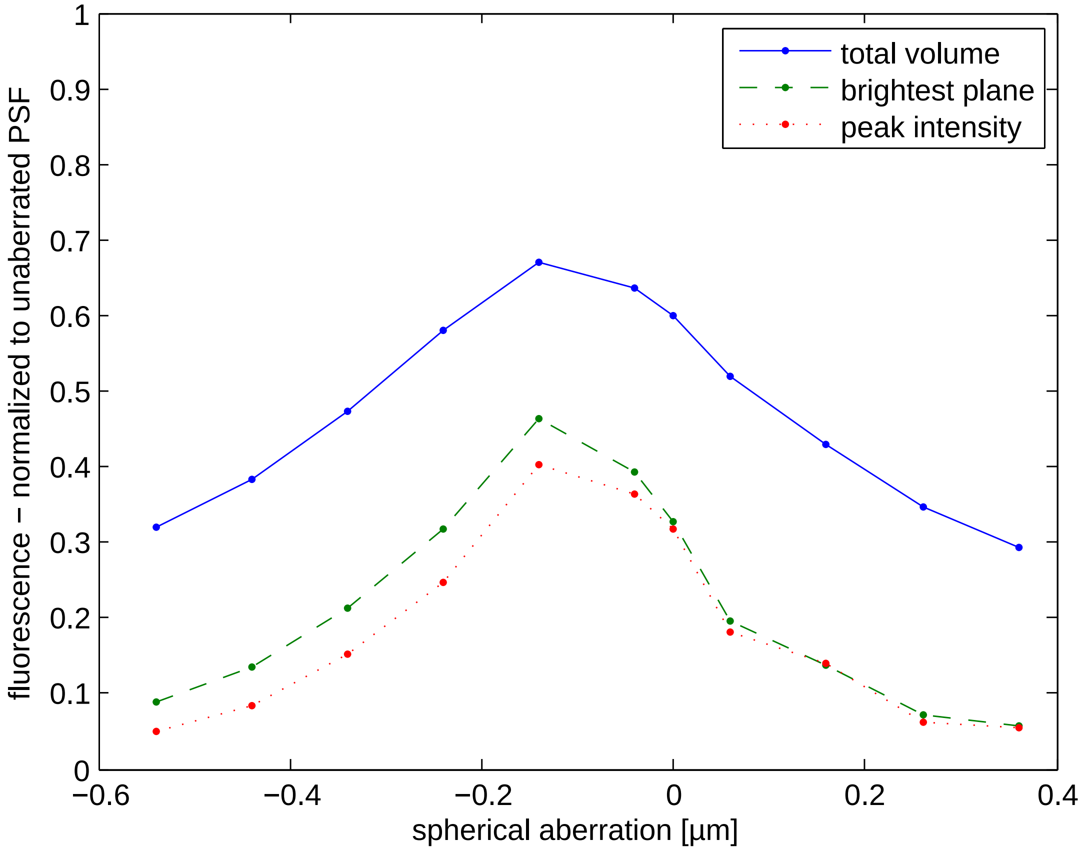

Figure 2.7. – Lowest order spherical aberration is varied between the value introduced by the sample ($-0.540\,\mu$m for 1 mm depth inside a flat brain) and a slightly positive value, while two higher orders of spherical aberration were kept at the constant values introduced by said sample ($Z25 = -0.108\,\mu\text{m}, Z36 = -0.020\,\mu\text{m}$). The three curves correspond to the intensity acquired from a point object, fluorescent plane or homogeneously stained volume. All curves are separately normalized to the intensity resulting from an unaberrated focus. The left end of the curves shows that a point-like object (red dotted curve) in 1 mm depth inside the brain will appear only 5% as bright compared to unaberrated imaging, a fluorescent plane (green dashed curve) will be at 9% fluorescence, while the integrated fluorescence over the whole volume (blue solid cuve) was still at 32%. This implies that large objects can expect a factor 3 improvement in fluorescence from perfect aberration correction, while pointlike objects might appear up to 20 times as bright.

3. Setup

The requirements for the experimental setup were

- two-photon microscopy
- imaging deep inside highly scattering biological samples such as the rodent cortex
- with a microscope objective suitable for pipette access (for staining and possibly electrophysiology)
- with precise control of the excitation laser light wavefront
- synchronization between two-photon image acquisition and wavefront control

To allow deep imaging, an existing setup [40, 38] with regenerative amplifier was used, which was updated with the current version of custom designed two-photon microscope hardware[16] and electronics[41]. For details not mentioned in the following description see those references. A deformable mirror(MIRAO, Imagine Optic, France) for modifying the wavefront was added in the excitation light path of the deep imaging microscope. A Shack-Hartmann wavefront sensor(WFS150, Thorlabs Inc) was used to calibrate the deformable mirror.

Details of the electronics of the setup will be described later. Let us now focus on the optical path.

3.1. Optical path

Since the microscope was not used for retina imaging, some components described by Euler et al. were not implemented, namely the visual stimulator arm and all components beyond the objective. Instead, an extra telescope was inserted between the laser and the scan mirrors to image the deformable mirror onto the scan mirrors and therefore onto the back focal plane of the objective.

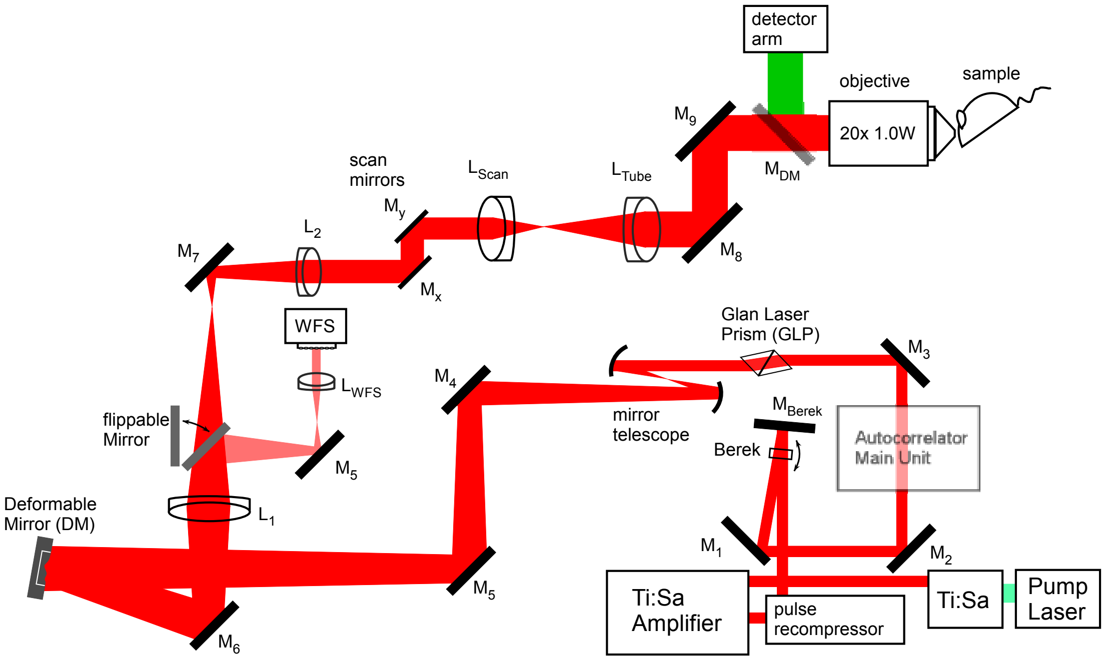

Figure 3.1. – Schematic drawing of the optical light path of the adaptive optics deep imaging (AODI) setup. Elements are as follows: Pump Laser (Verdi V-5, Coherent Inc), Ti:Sa laser (Mira 900, Coherent Inc.), Ti:Sa amplifier (RegA 9000, Coherent Inc.), pulse recompressor (single grating 4-pass pulse compressor), Berek (crystalline quartz plate, used as Berek's compensator), Autocorrelator Main Unit (CARPE, APE GmbH), GLP (Glan Laser Prism), deformable mirror DM (MIRAO, Imagine Optic, France), L_1 (f=300mm NIR doublet, AC254-300-B, Thorlabs Inc), flippable mirror (dielectric mirror in motorized Flipper mount, New Focus Inc), L_{WFS} (f=80mm doublet, LINOS), WFS (WFS150, Thorlabs Inc), L_2 (f=120mm NIR doublet, G322309525, LINOS), scan mirrors, L_{scan} (f=61.4mm Scanokular for 20x/1.0W objective, Leica Microsystems), L_{tube} (f=200mm tube lens, Nikon), M_{DM} (low-pass dielectric mirror for separation of fluorescence light, objective (20x/1.0W electrophysiology objective; similar objectives by Zeiss and Leica Microsystems were used). detector arm (focusing lens, dichroic filters for color separation and 2 photomultiplier tubes). Mirrors M_n not mentioned are folding mirrors.

A detailed schematic drawing of the optical light path can be found in figure 3.1. The description of all components along the light path will now be given, starting in the lower right corner.

A Ti:Sa oscillator provides the seed pulse for the Ti:Sa regenerative amplifier, which produces pulses at a rate of ∼200kHz. These pulses are negatively prechirped by adjusting the recompressor such that the pulses leaving it have the appropriate prechirp to produce the shortest possible autocorrelation FWHM under the microscope objective, measured with the external detector mode of a CARPE autocorrelator (APE GmbH, Berlin).

Intensity control is achieved by rotating the axis of linear polarization of the laser light by a varying angle before selecting only one polarization component. Variable polarization rotation is achieved by a crystalline quartz plate that is mounted onto a galvo-scanner and acts as a Berek's compensator. A high-transmission Glan-Laser prism selectively transmits the rotated polarization while sending the laser light with unrotated polarization into a beam dump (not shown) [12].

Due to the limited size of the Berek's quartz plate and the slightly divergent laser beam, the Berek was placed as early in the beam path as possible. To allow enough space for the main unit of the CARPE autocorrelator, three folding mirrors M_1, M_2 and M_3 were necessary.

To reduce the number of dispersive components in the light path, a mirror telescope in z-configuration was used to control beam diameter and divergence of the laser beam reaching the deformable mirror (MIRAO, Imagine Optics, Orsay, France).

The lenses L_1, L_2 were used to image the DM into the mid-plane between the scan mirrors M_x, M_y, which was in turn imaged by the telescope formed by L_{scan}, L_{tube} onto the back focal plane of the objective. The distance between L_1 and L_2 was adjusted to recollimate the beam to optimize performance of the scan lens. During the experiments, it was found that a collimated beam did not, at the given excitation wavelength of 915nm, produce optimum performance of the objective lens. The divergence of the beam in the back focal plane was therefore optimized by moving L_{scan} to create a divergent (Zeiss objective) or convergent (Leica objective) beam.

Note that the folding mirror M_7 corresponds to M_1 in figure 3 of [16], which is reproduced here in figure 3.2; the lens L_2 is mounted in a special housing inserted into the vertical tube that holds M_7. The length of the upper half of the tube is fixed such that the upper focal point of L_2 is exactly between the two scan mirrors. This means that DM needs to be in the focus of L_1 to be imaged into said position. Changing the distance between L_1 and L_2 will then only influence the divergence of the beam, but the image of DM will stay exactly between the two scan mirrors.

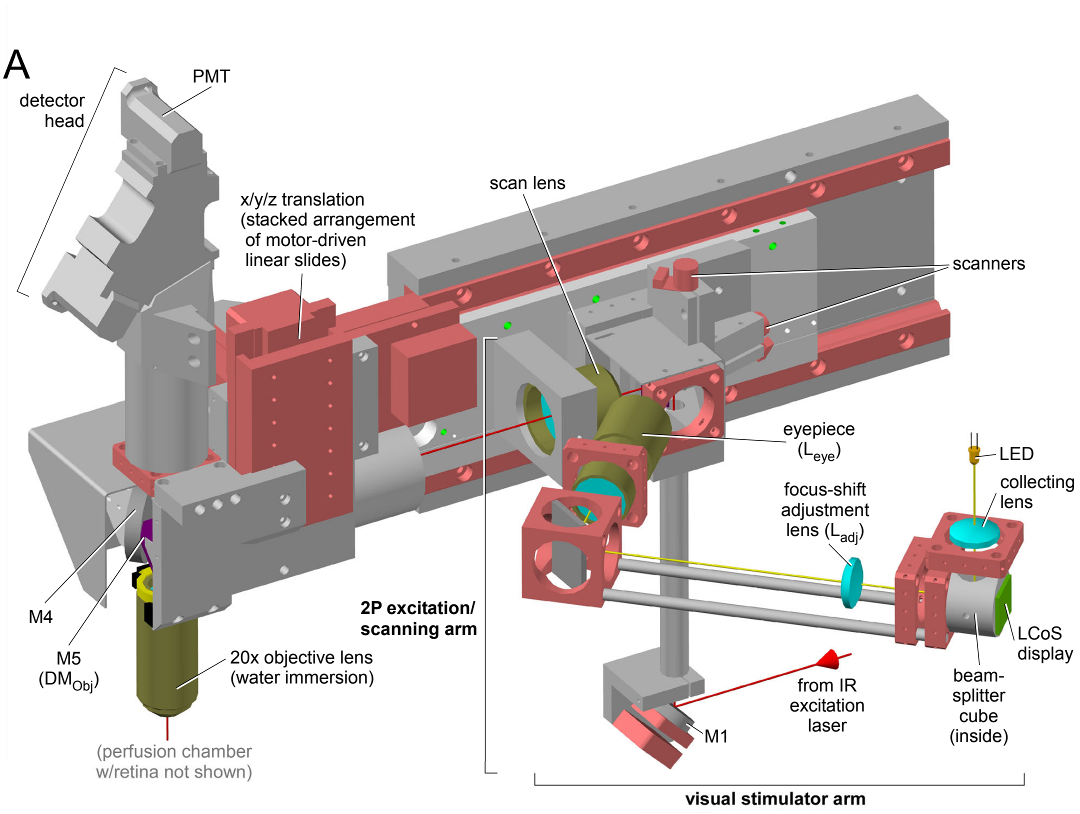

Figure 3.2. – Figure 3 of [16], showing the mechanical arrangements of the parts of the two-photon microscope. Compared to the figure, the microscope described here did not contain a stimulator arm. M_7 of figure 3.1 corresponds to M1 here; L_2 of figure 3.1 sits in a housing (not shown) inserted into the vertical tube above M_7 aka M1.

The focal lengths of the lenses L_1(f=300mm), L_2(f=120mm), L_{scan}(f=61.4mm), L_{tube}(f=200mm) and L_{WFS}(f=80mm) were chosen such that the full aperture of the DM (15mm) completely filled the specified free aperture of the scan mirror arrangement (6mm) and nearly filled the back focal aperture of the Leica 20x 1.0W objective (19.6 of 20mm) and the wavefront sensor (4 of 4.7 mm). For some experiments, a Zeiss 20x 1.0W objective was used, which had a back focal aperture diameter of only 16.2mm; however the magnification was not changed to account for this smaller diameter.

In deep imaging, depth-limiting background fluorescence can be minimized by distributing the excitation light evenly over the available numerical aperture[39].

While this calls for strong clipping of the $sinc^2$-shaped laser intensity profile to approximate a top-hat profile in the objective back aperture, excessive clipping reduces the transmitted laser power below the level needed to reach background-fluorescence-limited depths. The mirror telescope mentioned above could be used to optimize the amount of clipping, once the maximum excitation power necessary is established.

To allow comparison of the performance of the adaptive-optics microscope against a conventional two-photon microscope, the DM could be replaced by a flat silver-coated glass-substrate mirror. To allow exchange during experiments without the need for realignment, both mirrors were mounted on separate kinematic mounts that could be alternately attached to the same magnetic kinematic base plate (SB1, Thorlabs Inc) as shown in Figure 3.3. To avoid confusion between the DM in its best "flat" configuration and the intrinsically flat silver-coated glass-substrate mirror, the latter is referred to as "non-deformable mirror" (nDM) throughout.

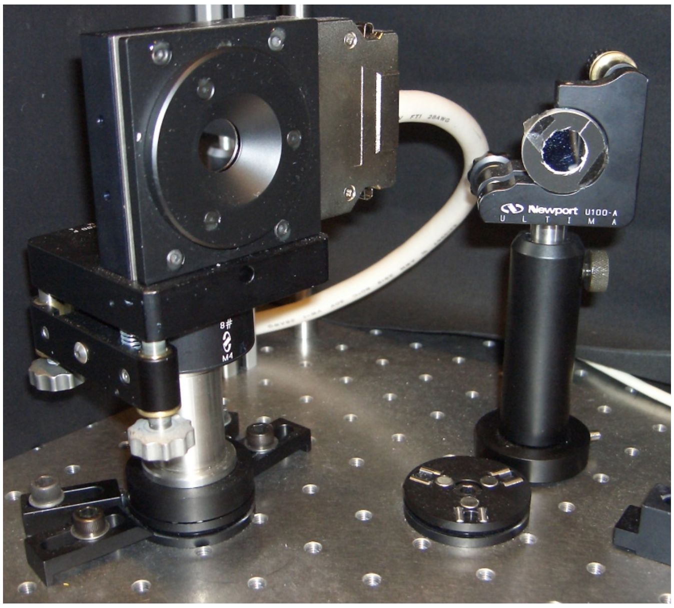

Figure 3.3. – The MIRAO deformable mirror (DM, left) can be quickly replaced by a silver-coated glass substrate mirror (nDM, right) because both are mounted on magnetic kinematic base plates (foreground).

In order to measure the shape of the wavefront emerging from the deformable mirror, a Shack-Hartmann wavefront sensor (WFS150, Thorlabs Inc.) was used. For different experiments, the sensor was placed either in the "objective" or "pre-microscope" positions, each of which has distinct advantages and disadvantages.

In the "pre-microscope" position, a mirror on a motorized Flipper mount behind

L_1 allowed diversion of the beam into the WFS arm, which consists of a steering mirror M_{WFS}, a collimating lens L_{WFS} and the actual wavefront sensor. L_{WFS} thereby takes the role of L_2 in the main path; its focus is where the lenslet array of the WFS should be placed, so that the lenslets are optically conjugate to the DM and thereby to the back focal plane and the wavefront sensor can faithfully report the wavefront in this plane.

The advantage of this configuration is it's flexibility during experiments. The motorized mount can be used the check the wavefront within seconds, without long interruptions to two-photon imaging. The wavefront across the full aperture of the DM can be measured. However, misalignments in the microscope light-path can cause the center of the DM not to be properly aligned with the center of the objective back focal plane. In this case, the determination of the pupil position on the WFS corresponding to the BFP would only be possible indirectly, since both planes are not imaged onto each other. Rather, they are two separate images of the DM, one corresponding to each position of the motorized Flipper mount. To still establish corresponding positions, a smaller aperture can be introduced somewhere before the flipper mount, but this has not been found very practical. To deal with this problem, the "objective" position was used for the wavefront sensor.

In the "objective" position, the microscope objective was replaced by an aperture of the size of the back focal aperture and an additional lens-based telescope ($f_1 = 200\,\mathrm{mm}, f_2 = 40\,\mathrm{mm}$) was added to image the BFP onto the wavefront sensor. This had the advantage that the aperture helps to define the correct pupil; after setting the correct pupil position in the software, the aperture was removed to avoid wavefront sensing problems caused by half-illuminated lenslets at the edge of the pupil. Tthe "objective" position for the WFS also allows the direct measurement of any aberrations created, e.g. by misalignment of optical elements, between M_7 and the objective.

In principle, it would be desirable to measure the wavefront directly in the BFP without an additional imaging telescope, or even the spherical wavefront emanating from the objective. The direct measurement was not possible because the size of the sensor is too small by a factor of 5. A larger sensor or wavefront stitching might be possible solutions to this but were not pursued further. The latter was not possible since the highly defocused wavefront results in most sublens spots leaving the WFS CCD detector area; the remaining spots can not be analyzed by the software. A direct measurement of the wavefront was therefore not possible without the use of additional lenses.

3.2. The alignment procedure

To optimize transmission through the intensity control system, the linear polarization of the input beam needs to be rotated by exactly 90° by the Berek's compensator. Usually this is achieved by aligning the top of its housing horizontally with a level, bringing the galvo-scanner axis to a 45° angle. However, if the quartz is not perfectly aligned with the galvo-scanner, optimum transmission might actually result from rotating the housing by a few degrees to improve the alignment of the quartz plate (in current setup by -8° when viewed from the laser-beam side).

Subsequently, the angle under which the laser beam enters the Glan Laser Prism is optimized. The double prism is cut such that both internal and external surfaces can be crossed at Brewster angle to minimize reflection losses. In the current setup, 9° downwards tilt of the GLP housing maximized transmission.

Next, the mirror telescope needs to be aligned. Astigmatism produced by these spherical mirrors due to non-orthogonal incidence would later reduce the available dynamic range of the adaptive optics system. To minimize this effect, the laser beam should hit the spherical mirrors as close to the edge as possible, with both mirrors positioned so as to produce the flattest z-shape possible. The axial distance between the two mirrors should be slightly less than the sum of their focal lengths to produce a divergent beam, with the exact distance adjusted to sufficiently overfill the aperture of the deformable mirror while not cutting off too much of the laser power. The intensity profile can be viewed[1] with the “Line View” mode of the WFS software, or with a normal CCD camera put into the WFS position.

For the beam alignment beyond the DM, a complexity is added since the deformable mirror should later be replaceable by the nDM without changing the rest of the alignment. For this to work, both mirror surfaces have to be in exactly the same position when mounted on the magnetic kinematic base plate. Parallelity of the surfaces is even more crucial than position of the reflecting plane, since the wavefront sensor is extremely sensitive to tip/tilt. Unfortunately, the mount of the DM does not allow fine control of the rotation of the mirror around its vertical axis. Sufficient control of beam direction is available by rotating the magnetic kinematic base plate, but the parallelity with the nDM can only be ensured by adjusting the mount of the nDM, or by offset voltages on the DM.

To avoid applying offset voltages for tip/tilt correction, the DM with all voltages set to zero is imaged onto the wavefront sensor, and the tip/tilt values are noted down. The nDM is then put into the beam path and its tip and tilt are modified to match the values found for the DM. Both mirror surfaces are now parallel. To

---

[1] once the beam is walked to the wavefront sensor

restrict the aperture of the nDM to the 15mm radius of the DM, an annular mask is attached to it. To ensure correct lateral placement, the WFS is replaced by a normal CCD camera and the position of the image of the DM on the CCD is used as a reference for the beam transmitted through the nDM mask.

With these preparations, the nDM provides a flat reflecting surface which has the same diameter and surface normal as the nDM, which can be used for most subsequent alignment steps.

Unfortunately, the rest of the beam alignment requires some amount of iteration. This is caused by several restrictions of the setup, which require the distance between elements to be fixed starting at the end of the light path, i.e. objective, then scan lens, scan mirrors, L_2 and finally (n)DM.

The distance between tube lens and objective will have to be somewhat flexible later to image different areas of the sample. However, any movement of the objective in x, y or z will cause an axial displacement of the images of scan mirrors and deformable mirror relative to the back focal plane[2]. Therefore, the rough position of the objective during calibration should correspond to the position used later during imaging.

In the wavelength range used (around 915nm), the high-NA electrophysiology objectives do not operate optimally with a collimated laser beam; instead they allow for higher two-photon fluorescence signal at significantly convergent or divergent beams, depending on the objective type. The divergence of the laser beam in the BFP therefore needs to be adjusted while monitoring fluorescence.

For this step, the two-photon setup needs to be sufficiently aligned to do two-photon imaging in a fluorescent soup; in particular, the laser beam at the scan mirrors must be collimated through the appropriate positioning of L_2, and the beam needs to propagate on the optical axis between the scan mirrors and the scan lens.

Changing the divergence is most conveniently achieved by moving the scan lens. However, moving the scan lens changes the position of the image of the objective back focal plane created by tube lens and scan lens, so the scan mirrors need to move to be centered around this new position. To determine where both scan mirrors are imaged, the following steps were used:

- insert an aperture near the DM to reduce the diameter of the beam on the scan mirrors

---

[2] The arrangement of translation stages and mirrors avoids any off-axis movement, see [16] for details

- configure the two-photon software CfNT (Setup/Scan Position) so that the slow scan mirror (M_y) moves over a wide angle (e.g. range 2V and zoom 0.25) to make the movement easily visible while the fast mirror (M_x) moves hardly at all (e.g. range 0.001V).
- determine the plane in which there is no movement; this is the image plane of the slow scan mirror M_y
- configure CfNT to rotate the image by 90°, which causes the fast and slow mirrors to change their roles
- determine the plane in which there is no movement; this is the image plane of M_x. Due to the distance of ~7.5mm between the scan mirrors and the magnification factor of 3.3 in the current setup, this plane should be about $0.75\,\text{cm} \times 3.3^2 = 8\,\text{cm}$ above the image plane of M_y.
- move the scan mirrors along the optical axis so that the center between them is imaged into the back focal plane as shown in figure 3.4.

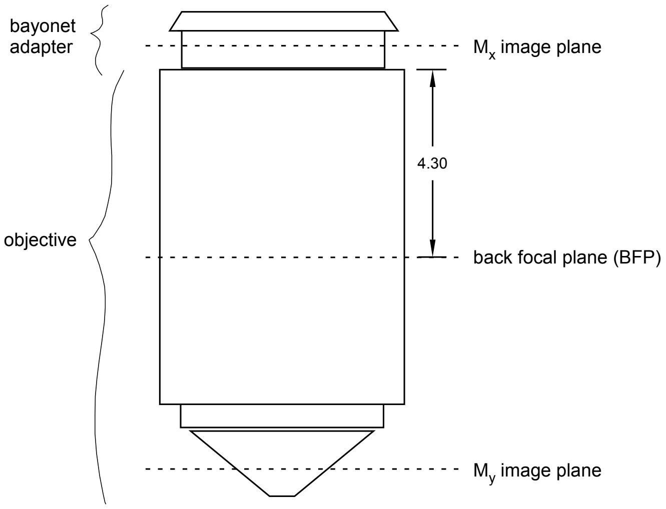

Figure 3.4. – schematic drawing of the 20x NA=1.0 water objective (Zeiss) and the position of the relevant planes. For minimal movement of the laser illumination in the back focal plane(BFP), the scan mirrors should be imaged symmetrically above and below the BFP. This implies that M_x will be imaged 1cm below the bayonet.

Since the back focal planes of both objectives used are 4.7 (Leica) and 4.3 cm (Zeiss) below the objective screw thread, and this corresponds roughly to half the distance between the images of M_x and M_y, a trick can be used for positioning the scan mirrors correctly. The position on top of the bayonet adapter corresponds roughly to the plane into which M_x will be imaged for correct positioning of the BFP. Therefore, it is sufficient to place a piece of cardboard on top of the bayonet adapter[3] and optimize for minimal movement to find a good position for the scan mirrors. Note that M_x ("fast mirror") should be scanned slowly, with M_y essentially stationary. This is achieved by setting the scan range for x (sic!) to near zero, setting a large scan range for y and then interchanging the meaning of the two by applying a 90° rotation.

Positioning the scan mirrors also moves L_2, which sits in the housing directly below the scan mirrors. Therefore, the distance to L_1 has changed, destroying the collimation of the laser beam on the scan mirrors. Therefore, L_1 needs to be movedby the same amount that the scan mirrors were moved.

Finally, the last calibration step is to position the deformable mirror so that it gets imaged into the back focal plane. For this, tilt voltages can be applied to the deformable mirror using `mir_tiptilt_oscil.m`; again the correct image plane is where least movement can be observed. Since the spatial resolution of the SHS is limited by the lenslet array pitch, this calibration step is best performed with a regular CCD camera (without lenslets) placed in the position of the SHS. In the correct imaging plane, the aperture of the DM will not move, and actuators will neither be visible as dark nor as bright spots[4]. After correct axial positioning of the CCD camera, the SHS needs to be placed with the front focal plane of the lenslet array in the plane where the CCD camera had its active surface. Lateral position was controlled by keeping all appearing apertures concentric. Incorrect lateral positioning of the wavefront sensor relative to the back focal aperture of the objective will cause a rotationally symmetric wavefront to be transformed into one containing coma, creating a systematic error in the wavefronts applied.

More precise lateral positioning might possibly be achieved by using this very effect as a test: the lateral position of the wavefront sensor (or rather the pupil defined in the WFS software) is optimized so that a spherically aberrated wavefront produces bead PSFs with the minimum amount of lateral asymmetry. With the current software, this would be a very slow procedure, since a new influence function matrix(IFM) has to be acquired for each new position of the pupil. This could be circumvented if an IFM was acquired based not on the Zernike modes the

---

[3] since the correct plane for M_x is actually about 1 cm below the bayonet top surface, the Sutter can be used to lower the bayonet by this distance to improve this alignment step.

[4] The DM membrane is locally deformed in the spots where the actuators are attached; this deformation is normal according to the manufacturer. Its spatial frequency is too high to be represented by the Zernike modes available from the WFS150 software. However, the local deformation is clearly visible in the wavefront reconstruction error surface, which is calculated by integrating the SHS wavefront slopes directly and substracting the resulting wavefront from the one represented by the Zernike modes.

WFS software calculates for a specific pupil, but on the raw wavefront matrix.For this wavefront matrix, which would cover the whole area of the DM, different pupil positions could later be selected in MATLAB, reducing the time needed per iteration by about twenty minutes.

3.3. Electronics

Compared to a regular two-photon imaging system, two additional components play a mayor role in the electronics used. Firstly, the use of a regenerative amplifier makes triggering issues between excitation and detection important because the number of pulses per pixel is small (1 or 2) [38]. The RegA also requires modifications to the pre-amplification of the PMT signal. Secondly, control of the deformable mirror needs to be synchronized with image acquisition. Both topics will be treated in detail below. In contrast, the wavefront sensor used consisted of a USB device with manufacturer-supplied software, which could be integrated into the system without the need to create any extra hardware.

An overview of the electronics can be found in figure 3.5. The use of two different computers for two-photon imaging and adaptive optics (deformable mirror and wavefront sensor) was necessary due to the limited number of card slots in one computer. This made the synchronization between both computers necessary, which is described below.

3.4. Regenerative amplifier and fluorescence detection require precise timing on the pixel level

This subsection describes work done in close cooperation between Patrick Theer, Wolfgang Mittmann, Jürgen Tritthardt and myself, and is included here for completeness.

Since the pulse rate of the regenerative amplifier (RegA) is in the order of the pixel rate of the two-photon imaging, non-synchronized illumination will lead to a high fluctuation in per-pixel illumination power. Therefore, the RegA is triggered by the pixel clock, ensuring exactly one pulse per pixel [38]. An overview is given in 3.6a-c.

The higher peak intensity of the regenerative amplifier (RegA) infrared pulses compared to normal Ti:Sa pulses at the same average power implies that fluorescence generation and consequently the PMT signal will also show much higher peaks. Updating to the newest version of the two-photon electronics caused some problems with this, since the new digital electronics had a much lower dynamic range than the old analog version. Overflow problems in the analog digital converter (ADC) were the result (see figure 3.6b and c), causing a nonlinear decrease in detected signal.

To overcome this issue, the gain of the PMT pre-amplifiers was lowered and its time-constant increased, figure 3.6d). Lowering the time-constant allowed a better use of the single pixel integration time window by spreading the incoming PMT signal pulse over a longer time interval, thereby already lowering the peak intensity. Lowering the gain decreased the peaks further until clipping was avoided up to signal levels of 300 photons/pixel.

With this slower pre-amplifier, fluorescence created within a few ns after the excitation pulse is relayed to the ADC over the full $6.25\mu s$ pixel integration time window. For a direct triggering of the RegA through the pixel clock as used in [38], there is a delay of about $2\mu s$ between the start of a pixel and the onset of this pixel's PMT signal. (figure 3.6d). This will cause the tail of the exponential

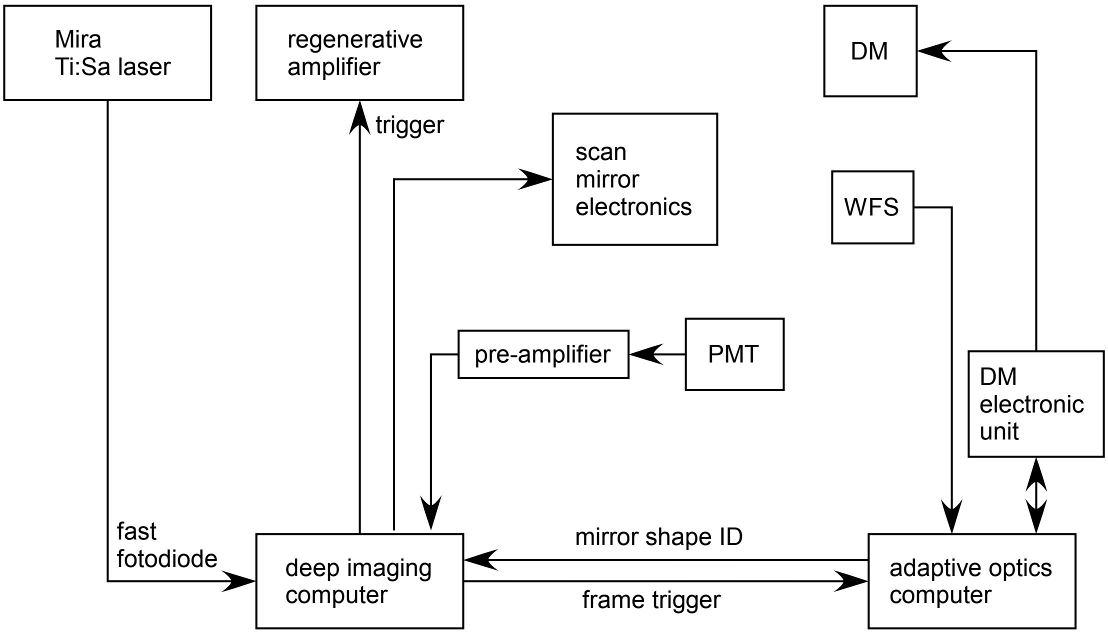

Figure 3.5. – Overview of the electronics used in the AODI setup. Main signal flows between components are indicated by arrows.

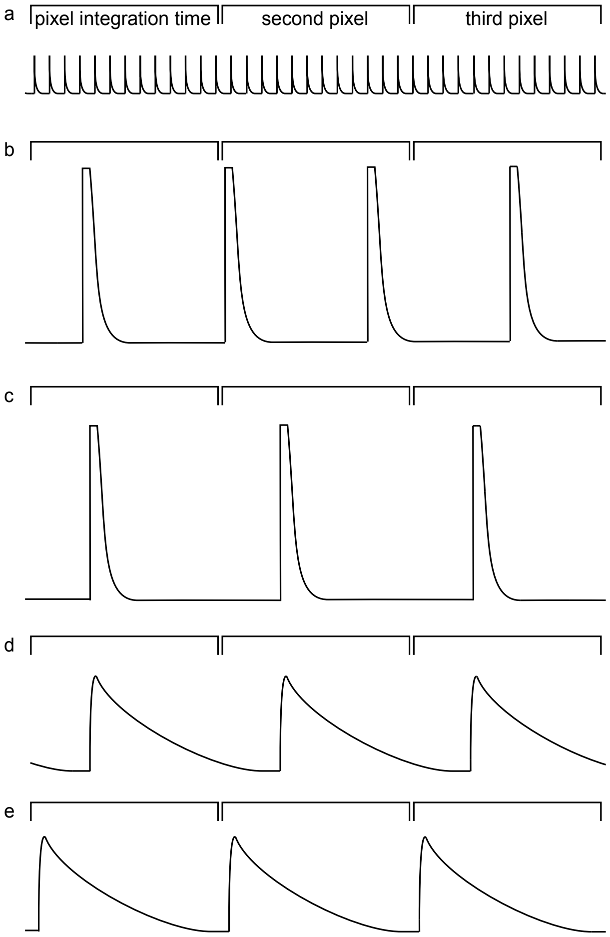

Figure 3.6. – Schematic drawing of pre-amplified PMT fluorescence signal, as sampled by analog-digital converter (ADC). The time course for three consecutive image pixels, corresponding to $3 \times 6.25\,\mu$s is shown. (a) Ti:Sa oscillators create about 500 pulses per pixel, resulting in frequent short PMT signal peaks and negligible synchronization problems (b) unsynchronized regenerative amplifier illumination causes high fractional excitation variation between different pixels, causing stripe artifacts at the beat frequency of pixel and RegA frequencies. Additionally, increased peak intensity causes cropping of high signals due to limited ADC dynamic range, even for moderate photon numbers per pixel. (c) triggering of RegA through pixel clock [38] removes inter-pixel variability. (d) increase of pre-amplifier time constant makes better use of available pixel integration time while decreased gain avoids clipping. (e) an additional time delay between pixel clock and RegA triggering synchronizes the onset of fluorescence PMT signal with the start of the next pixel, removing cross-bleeding from one pixel into the next.

to bleed into the next pixel's integration time window, causing a slight correlation between consecutive pixels. This effect can be minimized if the RegA trigger is delayed by an extra $4\mu s$, so that the fluorescence is generated at the very start of each pixel and the resulting pre-amplified PMT signal is integrated into the same pixel (figure 3.6e).

3.5. Synchronization of deformable mirror and 2P imaging allows inter-frame wavefront modification

The manufacturer of the deformable mirror states the bandwidth with >200Hz; with a two-photon imaging line frequency of 500Hz this should allow mirror shape changes within three image lines. Applying different wavefronts for consecutive 2P images should therefore be possible without modifying the image acquisition, at the expense of a few unusable lines at the upper and/or lower edges of the image.

Speed of implementation and programming flexibility were of high concern in this work. Therefore, synchronization was implemented on the highest software level used, namely in the MATLAB-based user interface. The connection between the two-photon hardware and the adaptive optics computer was realized through simulated serial ports.

The frame trigger provided by the microscope hardware XPG-ADC was fed into a small electronic circuit which ultimately allowed a single character to be read from a virtual COM port of the adaptive optics computer whenever a frame trigger had arrived. For this, a retriggerable monostable multivibrator (SN74LS123, Texas Instruments) was combined with an USB-Parallel FIFO Development Module (UM245R, FTDI Ltd.). The design of the circuit can be found in figure 3.7.

A second similar circuit was designed and implemented by Jürgen Tritthardt, which allows single bytes sent to a second virtual serial port to be expressed as an analog voltage signal proportional to the byte value. The voltage range was selected to be 0 to 1 V to allow the signal to be fed into the Ch2A electrophysiology input channel of the two-photon microscope, allowing the transmission of a “shape ID” value from the adaptive optics setup to the microscope, which would end up directly in one of the first pixel columns of the image data. This shape ID was intended to allow identification of the mirror shape which was applied during the acquisition of that particular image frame.

Unfortunately, the data quality of this transmission channel proved surprisingly low, with only 3-4 bits of data which could be safely transmitted per byte. This seemed to be due to lookup table, rounding and noise issues; the latter possibly caused by an unresolved ground loop. However, it later proved more practical to synchronize image acquisition and off-line data analysis based on frame count alone. For on-line analysis (see "lock-in operation" in chapter 4) the transmission of a single bit per frame was sufficient, so that no time was invested to improve the shape ID transmission.

With these hardware connections in place, the MATLAB interface would wait for a byte on the "frame trigger" virtual serial port, set the deformable mirror to the new shape and then sent out the corresponding shape ID. Of course, neither the USB hardware nor the software used guarantee any maximum processing time. USB is a round-robin polling protocol, which could lead to delays in particular when other USB devices are busy, like the wavefront sensor used. The multitasking operating system (Windows XP SP2) does not guarantee a fixed time slice to any client program, so another time uncertainty is added. MATLAB user interfaces are convenient to code, but are not the optimal choice to minimize processing time.

As a result, the usual response time from frame trigger to mirror shape change lay

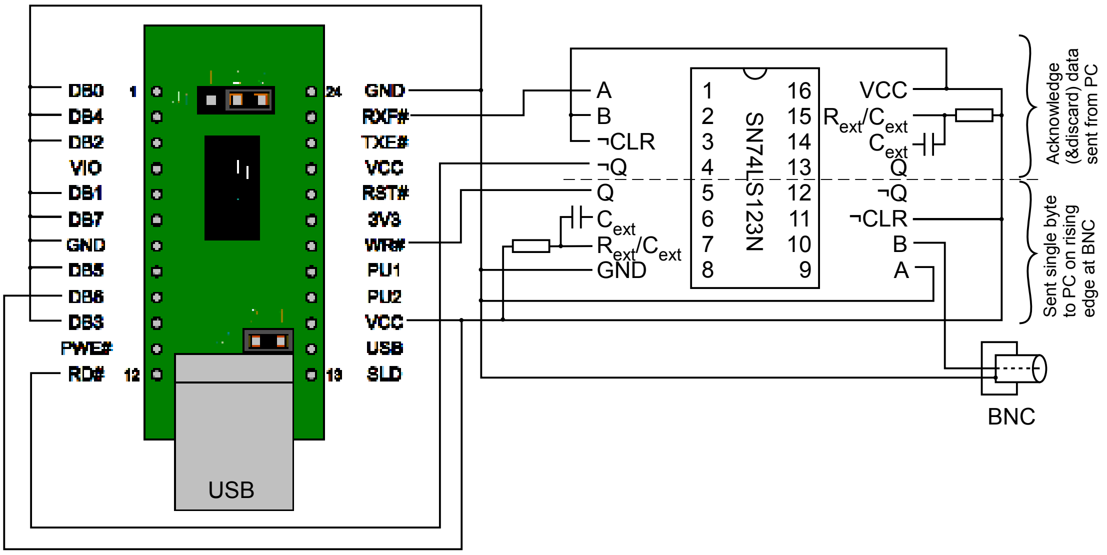

Figure 3.7. – USB frametrigger circuit design. The circuit is connected to the adaptive optics computer via USB, and the the frame trigger of the two-photon hardware through a BNC connector. Every frame trigger causes one character to be sent to the PC, allowing `aodi_gui` to react to the start of the new imaging frame.

in the order of 50 ms, corresponding to 25 lines. Therefore, an additional delay timer was used, delaying the trigger input for the USB frame trigger circuit to the end of the current frame. For a frame time of 512ms for a 256x256 image, a 460ms delay was used. Now only the jitter in the response time remained as a problem. Due to the described hardware and software uncertainties, jitter in the order of 20 ms was observed. As an easiest possible solution, the first and last 20 lines of each frame were discarded.

Of course the shape ID present in each image line could be used to approximate the moment of mirror shape change more exactly, but this was not seen as a priority in the current project. For routine operation of the adaptive optics deep imaging system, a redesign of this triggering mechanism to reduce jitter would probably be desirable. A switch to a non-polling interrupt-based trigger input, combined with more low-level software programming (machine compiled DLL instead of interpreted MATLAB) should be able to reduce the jitter considerably. For the most precise control, a pure hardware solution could be implemented, replacing or modifying the NuDAQ PCI-7200 controller card used by the deformable mirror. However, this would require information about the digital data transfer protocol used at this level and would probably be a project large enough for a complete bachelor's thesis in electronics or computer sciences.

4. Software

On the software side, connecting the different building blocks of the adaptive optics and deep imaging hardware was the first task. An overview of all major components with data flow is presented in figure 4.1, with the "adaptive optics for deep imaging graphical user interface" (`aodi_gui`) at the heart of the system.

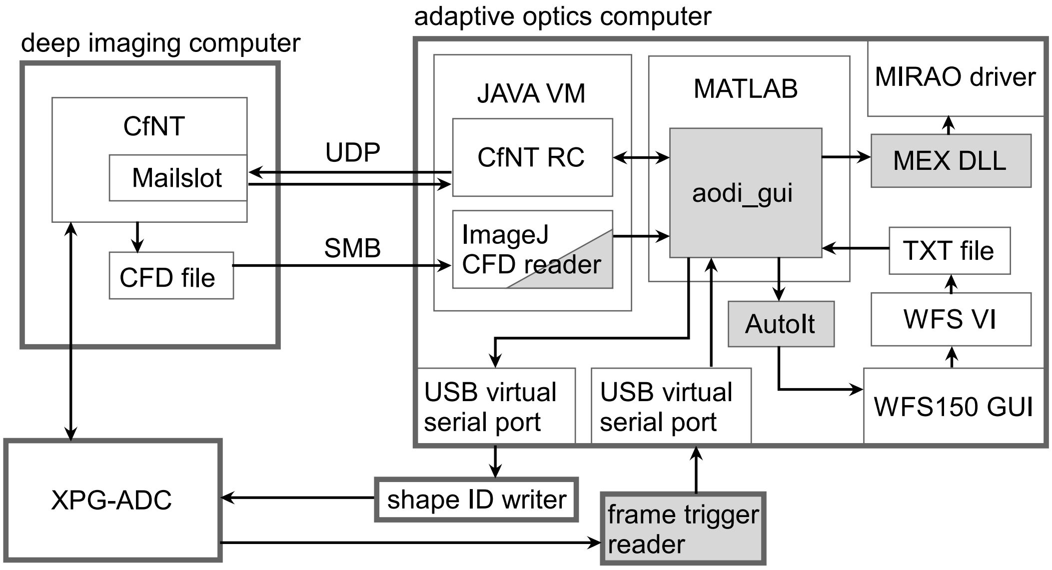

Figure 4.1. – Overview of the major software components on both computers, with data flow represented by arrows. For clarity, the external hardware components XPG-ADC, shape ID writer and frame trigger reader are also included. Components which were created as part of this diploma project are shaded in gray. The graphical user interface (`aodi_gui`) is the central component controlling all other parts of the system.

The deformable mirror MIRAO (Imagine Optic) was delivered with DLL device drivers with C header files, allowing applying an arbitrary voltage vector to the 52 actuators of the mirror. A wrapper DLL implementing the MATLAB MEX interface was written in Visual C to make this functionality available in MATLAB. The

MEX DLL also allowed performing safety checks on the voltages applied, implementing safety precautions given in the MIRAO user manual but not implemented into the mirror electronic unit or device drivers.

The wavefront sensor WFS150 (Thorlabs Inc.) came with a graphical user interface, but no programming interfaces for direct control by other software. Since configuration options could only be modified or documented using the graphical user interface (GUI), the AutoIt v3 (`www.autoitscript.com`) scripting language was used to make "remote control" of the WFS GUI possible from within MATLAB.

Furthermore, the wavefront data and Zernike coefficients calculated by the WFS could only be read out through National Instruments' proprietary and undocumented DataSocket protocol. To make the data available at a higher speed than AutoIt would have allowed, Jürgen Tritthardt implemented a DataSocket Client Application in National Instruments LabView, which writes new wavefront data to a text file whenever it is available. This text file can then be read from within MATLAB.[1]

Having made both the deformable mirror and the wavefront sensor controllable from within MATLAB, it was possible to implement a calibration routine, determining the correct control voltages necessary to produce a desired wavefront. This calibration routine will be described in a subsection below.

To integrate the wavefront control with the two-photon microscope, synchronization of image acquisition and mirror shape changes was necessary. Frame-by-Frame synchronization was achieved by a small electronics circuit called frame trigger reader, which is described in detail in the Electronics chapter. To synchronize the start of data acquisition, the CfNT remote control (CfNT RC) functionality was used, which was created by Michael Müller specifically for this project. The main use of CfNT RC is the possibility to implement automatic z shift compensation and will be described below.

---

[1] As a next step, implementation of the DataSocket Client as a MEX DLL in LabWindows/CVI or even a generic DLL in LabView could allow avoiding the textfile kludge. A speed improvement of a factor two could be expected from such a change, judging from data update rates in the current LabView Client compared to what reaches MATLAB. The textfile kludge is currently limited to 1Hz, since it relies on the file modification date and time to avoid reading the same data twice; a checksum based approach could already speed this up to some extend.

Since reading wavefront data appears to be the speed-limiting step in the calibration process, this could lead to a significant improvement in the time necessary to calibrate the deformable mirror against the wavefront sensor each morning (see main text).

To enable nearly-online[2] data analysis, the ImageJ CFD reader written by Thomas Euler was enhanced to provide image metadata such as real world coordinates and scaling. Through the Java Virtual Machine, ImageJ and the CFD reader were accessed from inside MATLAB. An arbitrary ImageJ Plug-In and possibly in the future even Macro can be used to determine automatically or semi-automatically the optimal z-slice for the next imaging stack. Using the real world coordinates, CfNT RC is then used to adjust the position (normally z, but also x and y if requested) of the microscope objective prior to a new imaging round.

This automatic position adjustment can be helpful for in-vivo imaging to follow slow drifts of the region of interest due to movements of the biological tissue. More importantly, apparent position changes caused by applying strongly aberrated wavefronts to the deformable mirror can automatically be compensated by opposing movements of the objective.

4.1. Calibration of the deformable mirror

As recommended by the manufacturer of the mirror, the linear dependence between individual actuator voltages and resulting Zernike coefficients (as measured by the wavefront sensor) was determined. This was done by applying at least two different voltages to each actuator while keeping all other actuators at 0 V. The Zernike-versus-Voltage slopes were determined using linear regression and stored in a matrix. The inversion of this "characteristic" matrix[3] would in principle allow calculating control voltages from Zernike coefficients, but without any bound on the voltages. To ensure control voltages in the permitted range, quadratic programming was used for their calculation instead of the (pseudo) inverse of the matrix [32].

One-shot calculation of control voltages using this algorithm generally created wavefronts roughly approximating the desired shape. Deviations were probably caused by a slight nonlinearity and hysteresis of the mirror, thermal drifts as well as uncertainties in the determination of the characteristic matrix and in the measurement of the current shape of the wavefront. For details of these measurements, see section 5.2.

Improvements can be achieved by closed-loop optimization as described by [32], with no further improvement after usually three to eight iterations. However, true

---

[2] nearly-online refers to the fact that an image stack is analyzed immediately after it has been written to hard disk, and the knowledge gained from it is used to optimize parameters before acquisition of the next image stack.

[3] in the code, the "characteristic" matrix is referred to as eIFM

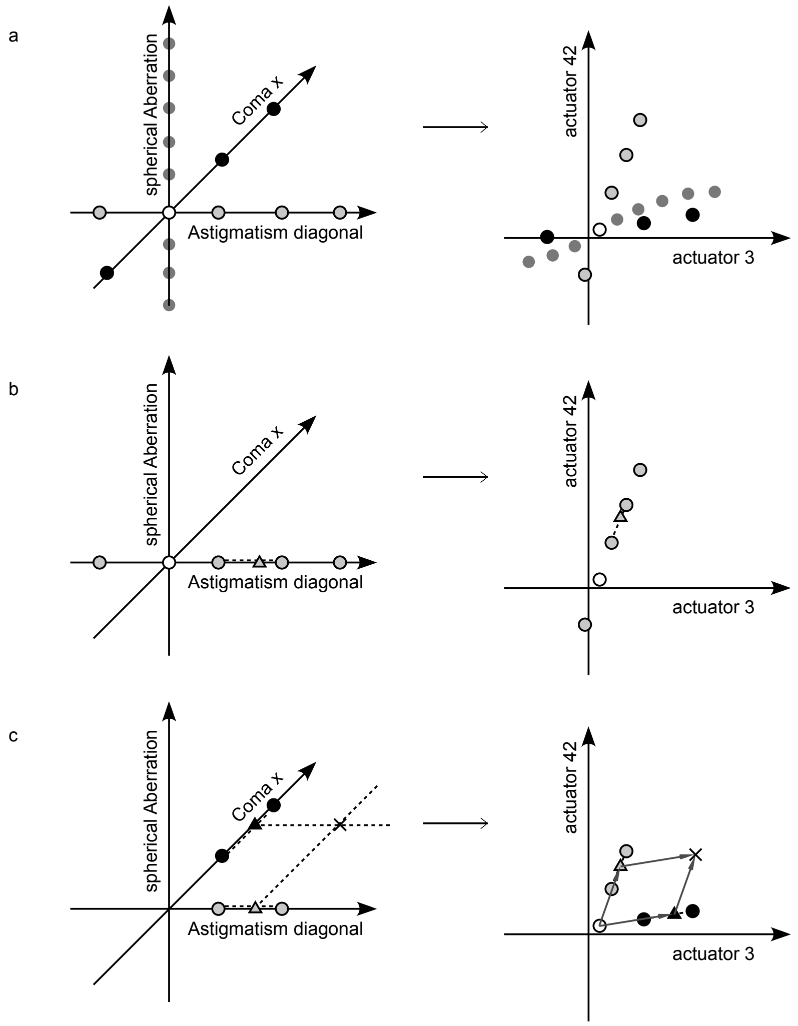

Figure 4.2. – schematic drawing of the second step of the calibration algorithm. (a) The dependence between Zernike vectors (left) and the voltage vectors necessary to create them (right) is sampled. Both spaces are high-dimensional, but only three resp. two dimensions are shown. Circles represent sampling points in Zernike vector space for which the optimal voltages are determined iteratively (not shown). Note that sample points from the same axis (marked by same shading) lie roughly on a straight line in voltage space, signifying the general linear behavior of the mirror. In general, a flat wavefront (white circle) corresponds to non-zero voltages on the mirror. (b) Interpolation for a point on the axis (marked by a triangle) in between sampling points (marked by circles). (c) Extrapolation away from the axes (cross) is done by projecting onto the axes in Zernike space, finding the two closest sample points (circles), interpolating(triangles) and adding the resulting voltage vectors (measured relative to the flat mirror voltages)

closed-loop operation during imaging was not possible with the current setup, where the wavefront sensor could only be used while the objective and sample were removed (for the “objective” wavefront sensor position) or the flipper-mirror diverted the laser beam away from the microscope (for the “pre-microscope” wavefront sensor position). To avoid reactivating the wavefront sensor for each wavefront change, while still achieving more precise wavefronts than through one-shot voltage calculation, a second stage was added to the calibration process.

This second stage consisted of iteratively refining the voltages necessary for certain Zernike vectors, and storing these voltages for later use[4]. It was found that these stored voltages were better than one-shot calculated voltages even hours after their determination.

To keep the calibration procedure reasonably short, the optimized voltages could only be determined for a limited set of Zernike vectors. In fact, the set had to be orders of magnitude smaller than the number of different wavefronts which would later be needed. To make it possible to create all desired wavefronts from a limited set of calibration points, interpolation was used. This was aided by the fact that only wavefronts containing a certain subset of Zernike modes were to be created.

For each Zernike mode in question the optimal voltages were determined (iteratively as above) for certain values of that coefficient, while keeping all other Zernike coefficients zero. In the multidimensional space spanned by all Zernike vectors, this corresponds to sampling along the coordinate axes corresponding to the modes that we are interested in, without sampling any points away from the axes (which would correspond to Zernike vectors with more than one nonzero coefficient).

Voltage vectors for points along these axes could then be determined by interpolation between the two closest sampling points in Zernike vector space, see figure 4.2b. Voltages for arbitrary Zernike vectors[5], i.e. also away from the coordinate axes, were calculated by linear extrapolation from the two closest sampling points on each axis, as shown in figure 4.2c. It was found that this approach yielded better wavefront shapes than one-shot voltage calculation.

In a sense, the function mapping Zernike coefficients to actuator voltages was no longer approximated by the hyper-plane given by the inverse characteristic matrix. Instead, the function was tabulated by sampling it along certain axes in the high-dimensional input space.

---

[4] in the code, the mapping between one such Zernike coefficient vector and its corresponding optimized voltage vector is called IFP (influence function point)

[5] within the subspace sampled

4.2. User Interface

The graphical user interface developed during this diploma project allows flexible control of the wavefront, to facilitate manual optimization of Zernike coefficients for a particular sample during two-photon imaging. In the simplest form, 6 Zernike coefficients can be modified at will either using slider controls or by directly entering fixed values (top left of figure 4.3). To verify the quality of the actual wavefront, the button “Read Zernike Vector” allows taking a wavefront measurement and comparing the result to the Zernike vector defined by the slider controls.

During in-vivo experiments, movement artifacts can mask the improvement caused by slowly adjusting the wavefront. Therefore, an oscillation mode was implemented, which allowed alternating between two wavefronts on a frame-by-frame level, implementing a lock-in amplifier working at half the imaging frame rate. For this lock-in operation, bias voltages selectable on the lower set of sliders(figure 4.3) are alternatingly added to and subtracted from the best-guess voltages selected on the top set of sliders.

The same controls can also be used for automated linear variation of one coefficient. In this case, instead of oscillating between two fixed Zernike vectors, the line in Zernike space with these two vectors as endpoints is sampled in an arbitrary number of equidistant points, which are subsequently applied to the mirror, and repeated in a sawtooth-like fashion. The number of different shapes to be created is defined by the control labeled “Shape Count”. An illustration of manual Zernike coefficient control, oscillation and linear variation is give in figure 4.4. It is clear that the oscillation mode is merely a special case of the linear variation mode with a shape count of two.

In cases where more than one z-slice is to be recorded per wavefront setting, or where averaging is to be used in the image acquisition, “Image Frames per Shape” can be set to a value $n > 1$, causing `aodi_gui` to change the shape only on every n-th frame trigger it receives from the two-photon hardware.

For debugging purposes, mirror voltages can be visualized, showing a bar graph with the highest and lowest voltages currently in use, and a 2d contour plot of all voltages arranged according to the actual positions of the 52 actuators. For speed considerations, these plots are usually deactivated.

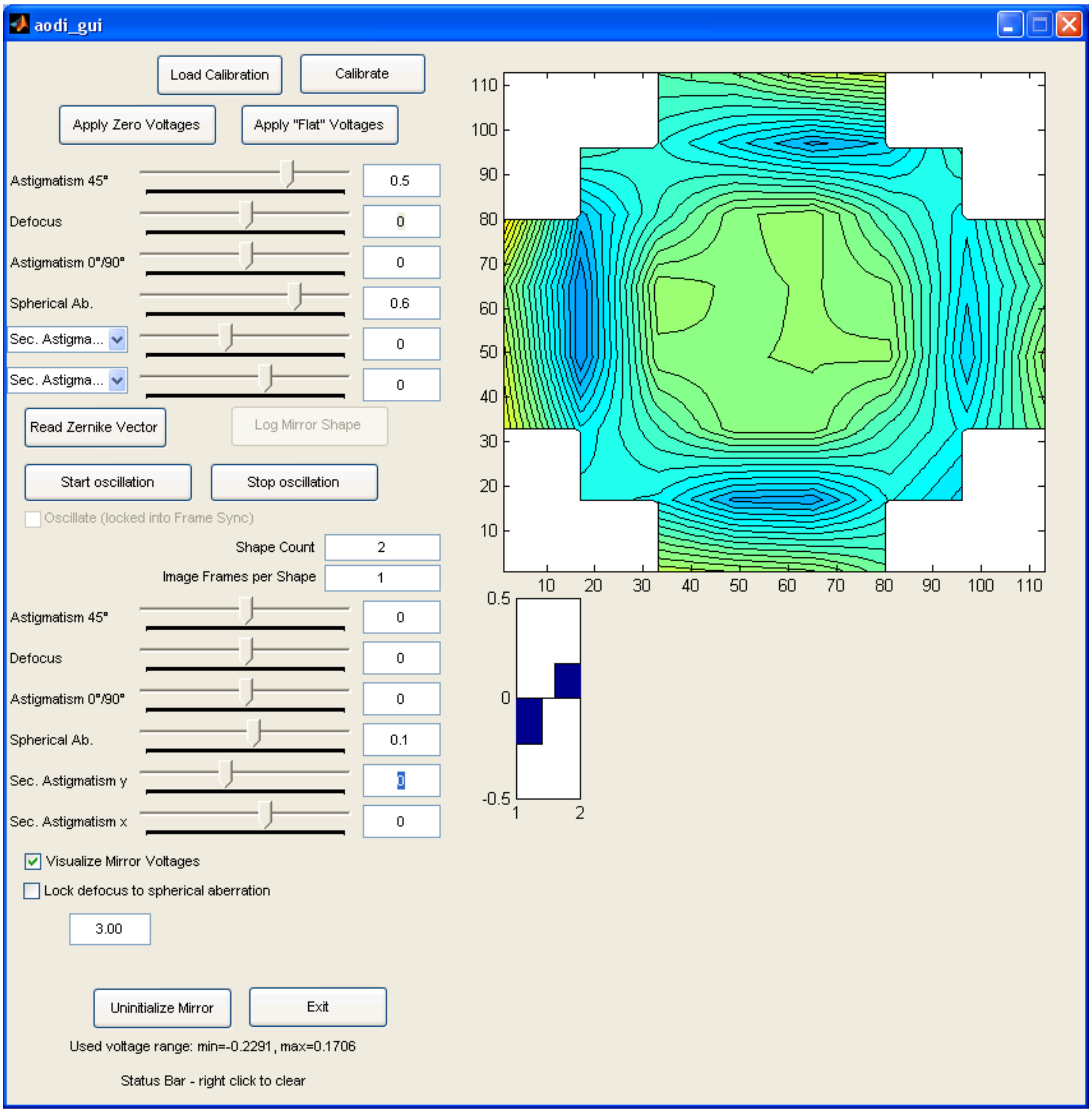

Astigmatism 45° 0.5
Defocus 0
Astigmatism 0°/90° 0
Spherical Ab. 0.6
Sec. Astigma... 0
Sec. Astigma... 0

☐ Oscillate (locked into Frame Sync)

Shape Count 2
Image Frames per Shape 1

Astigmatism 45° 0
Defocus 0
Astigmatism 0°/90° 0
Spherical Ab. 0.1
Sec. Astigmatism y 0
Sec. Astigmatism x 0

☑ Visualize Mirror Voltages
☐ Lock defocus to spherical aberration
3.00

Used voltage range: min=-0.2291, max=0.1706

Status Bar - right click to clear

Figure 4.3. – Screenshot of `aodi_gui`, Version 2008-09-23. A summary of the meaning of the controls is given in the main text.

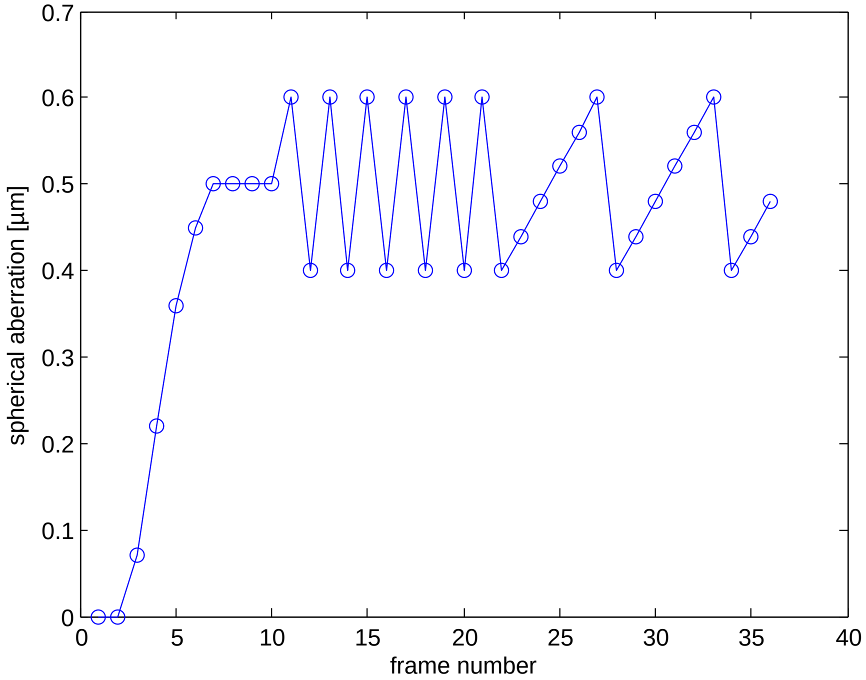

Figure 4.4. – Illustration of the different operation modes of `aodi_gui`. Frames 1-10: spherical aberration is manually increased from 0 to 0.5 μm using the 4th slider in the top half of figure 4.3. Frames 11-21: The oscillation amplitude is set to 0.1 μm in the lower half of figure 4.3, and "Start oscillation" is clicked. Frames 22-36: Shape Count is set to 6, activating linear variation mode. During oscillation and linear variation modes, mirror shape changes are synchronized with two-photon image acquisition on a frame level, causing shape changes to occur at the beginning of each frame.

5. Experiments

5.1. Characterization of the wavefront sensing

According to the manufacturer, the wavefront sensitivity of the Hartmann-Shack-Sensor (WFS150, Thorlabs Inc.) is $0.040\,\mu$m RMS. The repeatability of wavefront measurements in combination with the RegA laser was tested with the WFS in the “pre-microscope” position and the non-deformable mirror (nDM) in the light path. iRMS[1] difference between consecutive measurements was usually as small as $0.005\,\mu$m, with frequent peaks in the order of $0.040\,\mu$m (data not shown).

5.2. Characterization of the deformable mirror

5.2.1. Deformable mirror reflects better than standard silver mirror

Compared to the nDM (standard silver-coated glass substrate mirror), the deformable mirror (MIRAO 52d, Imagine Optics) had a 17% higher reflectivity, as measured by the background-corrected average grey value on the CCD of the WFS. From this, a 37% increase in 2P excitation can be expected. Therefore, excitation intensity adjustments were necessary whenever the fluorescence generation of both mirrors was to be compared.

5.2.2. Linearity of the deformable mirror

To test the linearity of the deformable mirror, a single actuator was deflected by different amounts while the other 51 actuators were kept at 0 volt, and the resulting

---

[1] The term iRMS (imaging-relevant RMS) refers to the root mean square of the Zernike modes mainly relevant for focus quality, i.e. excluding piston, tip/tilt and defocus. In contrast, fRMS (full RMS) also contains contributions from tip/tilt and defocus.

change of all 66 Zernike modes[2] was recorded. This procedure was repeated for each of the 52 actuators. As an example, the dependence of astigmatism on some of the actuators is shown in figure 5.1. It was found that all Zernike modes reacted roughly linearly to all actuators. Least-squares fitting was used to determine the slopes of the reaction; these slopes were stored in the influence function matrix (IFM, see figure 5.2) which was later used as the basis for controlled wavefront modification.

To estimate the amount of nonlinearity, the difference between fit and raw response data was calculated. For astigmatism, this is shown in figure 5.3, where the position

---

[2] The wavefront sensor software can not calculate more than 66 Zernike modes

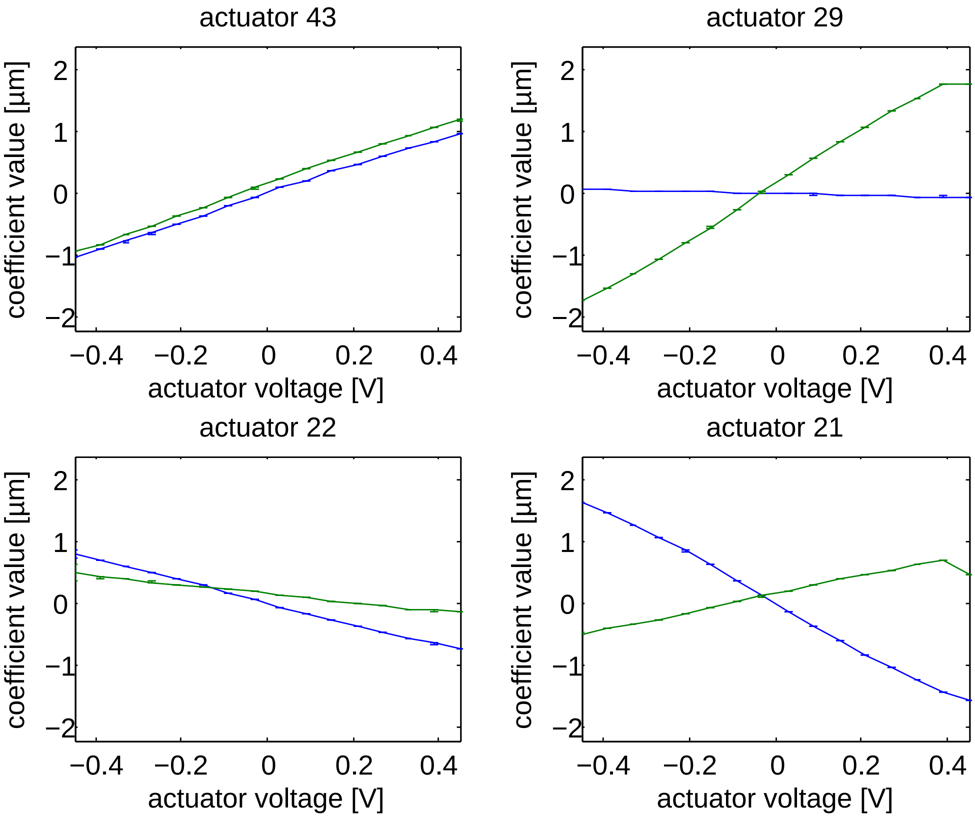

Figure 5.1. – Astigmatism depends roughly linearly on actuator voltages; both astigmatism modes are shown for several actuators. No kinks are seen in the $[-0.3, 0.3]$ V voltage interval. Kinks outside this interval are systematic measurement errors caused by excessive tilt, causing the wavefront sensor software to assign some diffraction spots to the wrong lenslets. Error bars give the standard deviation of ten independent measurements

of the graphs corresponds to the actual arrangement of the 52 actuators. From comparison with figure 5.1, it is clear that the nonlinearity is in the order of 5%, in line with manufacturer specifications. Especially for lower order modes like astigmatism, the nonlinear component did show some structure, which implies that a nonlinear model could possibly improve control of the mirror, leading to better open loop voltage calculations and quicker convergence in closed loop.

Note that in addition to the rather continuous wavelike nonlinear component, some actuators show jumps at very large positive or negative voltages. These jumps are caused by the wavefront sensor rather than by the deformable mirror; they occur when some diffraction spots of the microlens array move far enough to be assigned to the wrong lenslet by the software, leading to incorrect Zernike decomposition.

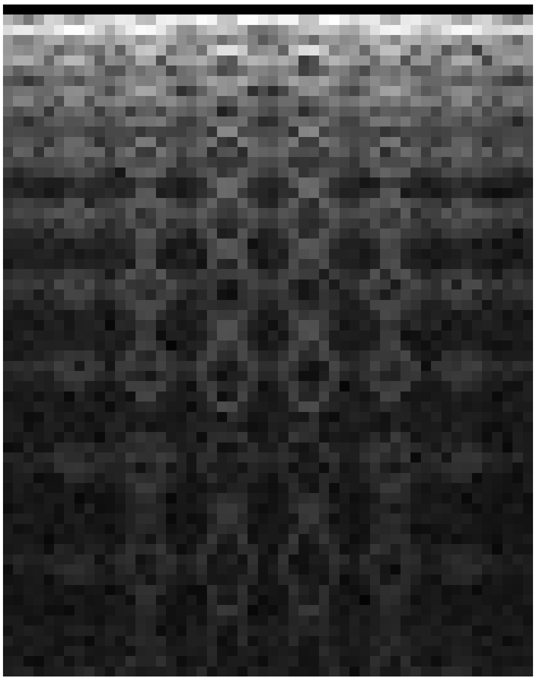

Figure 5.2. – Characteristic matrix showing the influence of the 52 actuator voltages on all 66 Zernike coefficients, with black=0 and white=highest absolute slope, with a gamma factor of 0.25 to account for the large dynamic range of matrix entries. The first row (corresponding to piston) is black because the Shack-Hartmann-Sensor cannot measure this mode and the non-physical values provided by the WFS150 are discarded. Circle-like and ellipsoidal structures arise because of the numbering schemes in both spaces and because Zernike modes with higher azimuthal frequency are more influenced by actuators further away from the center of the mirror.

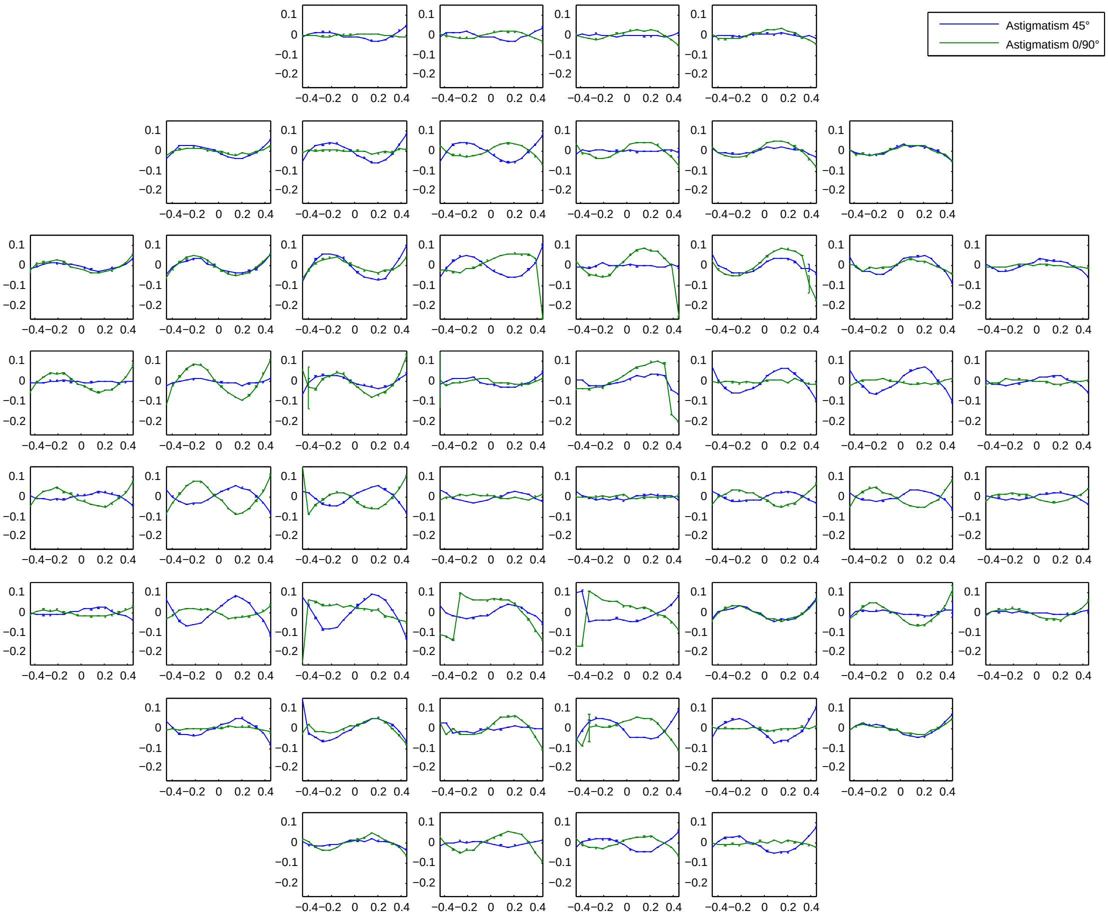

Figure 5.3. – Nonlinearity of dependence of astigmatism on actuator voltages is on the order of 5% (compare with figure 5.1), as claimed by the manufacturer. The 52 graphs and their positions represent the 52 mirror actuators; the x axis from $-.4\,\mathrm{V}$ to $0.4\,\mathrm{V}$ shows the voltage applied to that individual actuator, while all other actuators were kept at $0\,\mathrm{V}$. The y axis shows the nonlinear component of the Zernike astigmatism coefficients with a range of $[-0.2, 0.1]\,\mu\mathrm{m}$.

5.2.3. Creating wavefront shapes

Control voltages for the deformable mirror were calculated from the IFM and iteratively refined as described by [32], see also section 4.1. Two to six iterations were usually beneficial, after which the residual error (iRMS) converged to a value which depended heavily on the desired Zernike value, and on the Zernike mode. Convergence of different coefficient values for astigmatism and spherical aberration can be found in figures 5.4 and 5.5. In most cases, nice convergence was achieved, but iRMS did not always decrease monotonically. For larger desired coefficient values, the initial and final iRMS were usually larger. Higher-order modes generally converged in a smaller coefficient range.

The iRMS of the residual wavefront[3] improved up to 37-fold after 7 iterations (data not shown), compared to the residual after the first iteration (corresponding to open-loop operation). The median improvement factor was 3.5, the mean factor 4.2, i.e. the iRMS after 7 iterations was on average a factor of 4.2 smaller than the iRMS after the first iteration.

Since the wavefront sensitivity of the SHS was $0.04\,\mu$m, this value was also chosen as the maximum allowable iRMS residual, i.e. the RMS difference on imaging-relevant modes (everything except piston, tilt and defocus) had to be below this cutoff after a fixed number of iterations[4] to consider iteration successful. With such a residual RMS of up to $0.04\,\mu$m, a Strehl ratio of $S = 1 - \frac{2\pi}{\lambda}(0.04\,\mu\mathrm{m})^2 = 92.5\%$ should still be reachable[page 522 of 8].

With this criterion, the highest and lowest achievable value for each Zernike coefficient, called the deflection limit, was determined. The deflection limit for the first 27 coefficients (radial orders 1 through 6) is given in figure 5.6.

---

[3] i.e. the difference between the desired and the measured wavefront

[4] at different times, 7, 8 and 12 iterations were allowed for calibration before imaging; for testing purposes, up to 20 iterations were tried

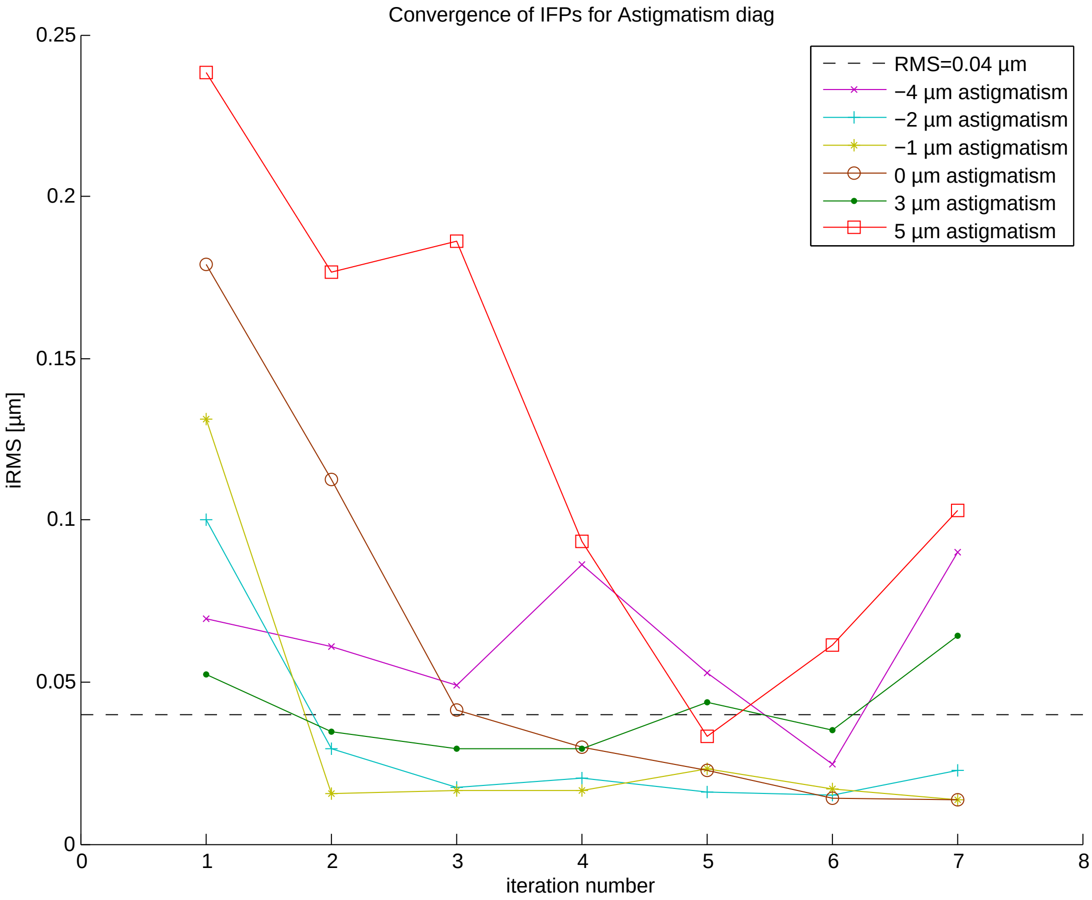

Figure 5.4. – iRMS wavefront error during iterative refinement of control voltages. Curves for different values of desired astigmatism are shown. For smaller desired values, convergence was usually faster and more stable.

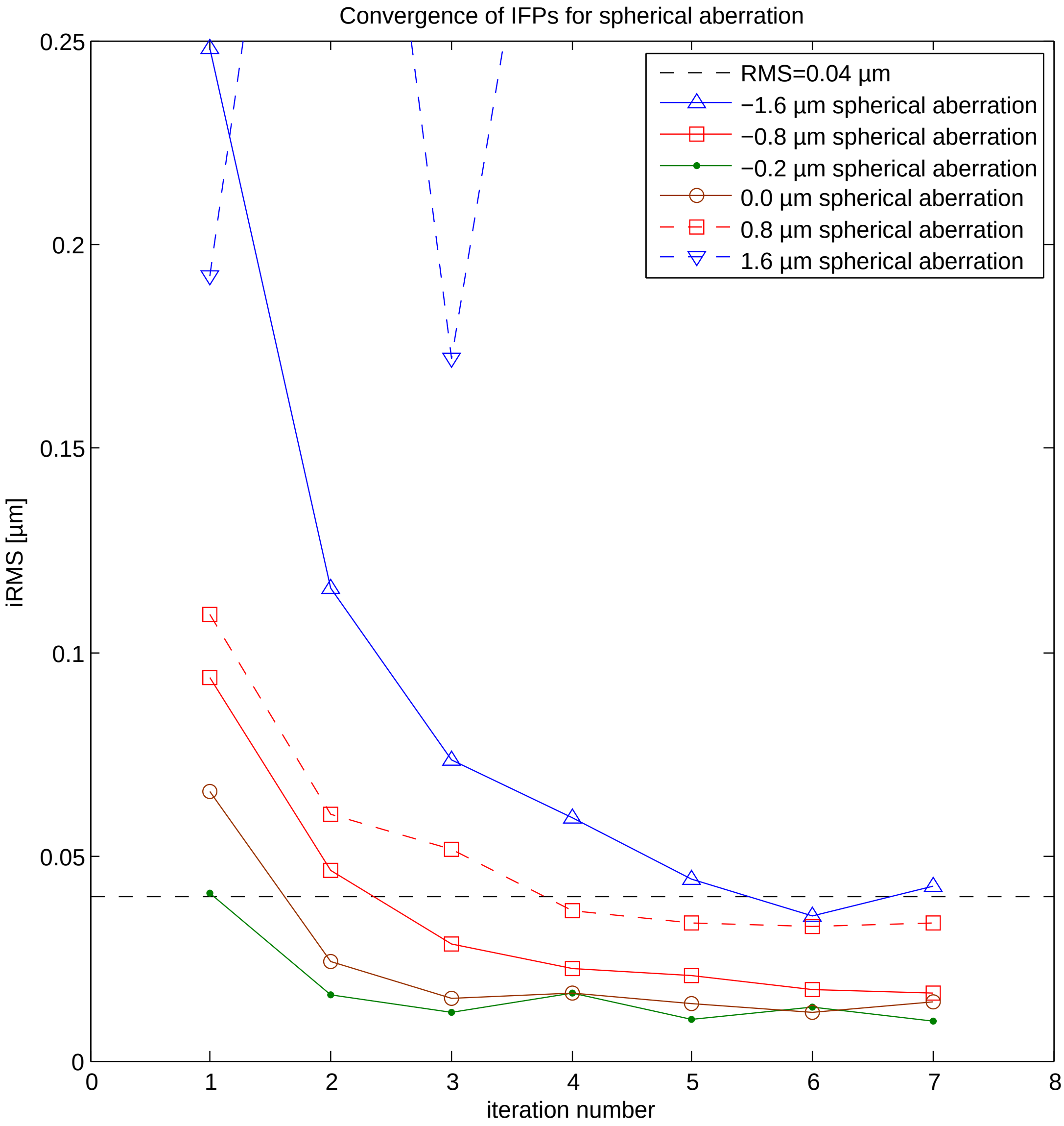

Figure 5.5. – Spherical aberration converges well, but in a much smaller range ($-1.6\,\mu\mathrm{m} \ldots 0.8\,\mu\mathrm{m}$) than astigmatism. For $sAb = 1.6\,\mu\mathrm{m}$, no satisfactory voltages wer found.

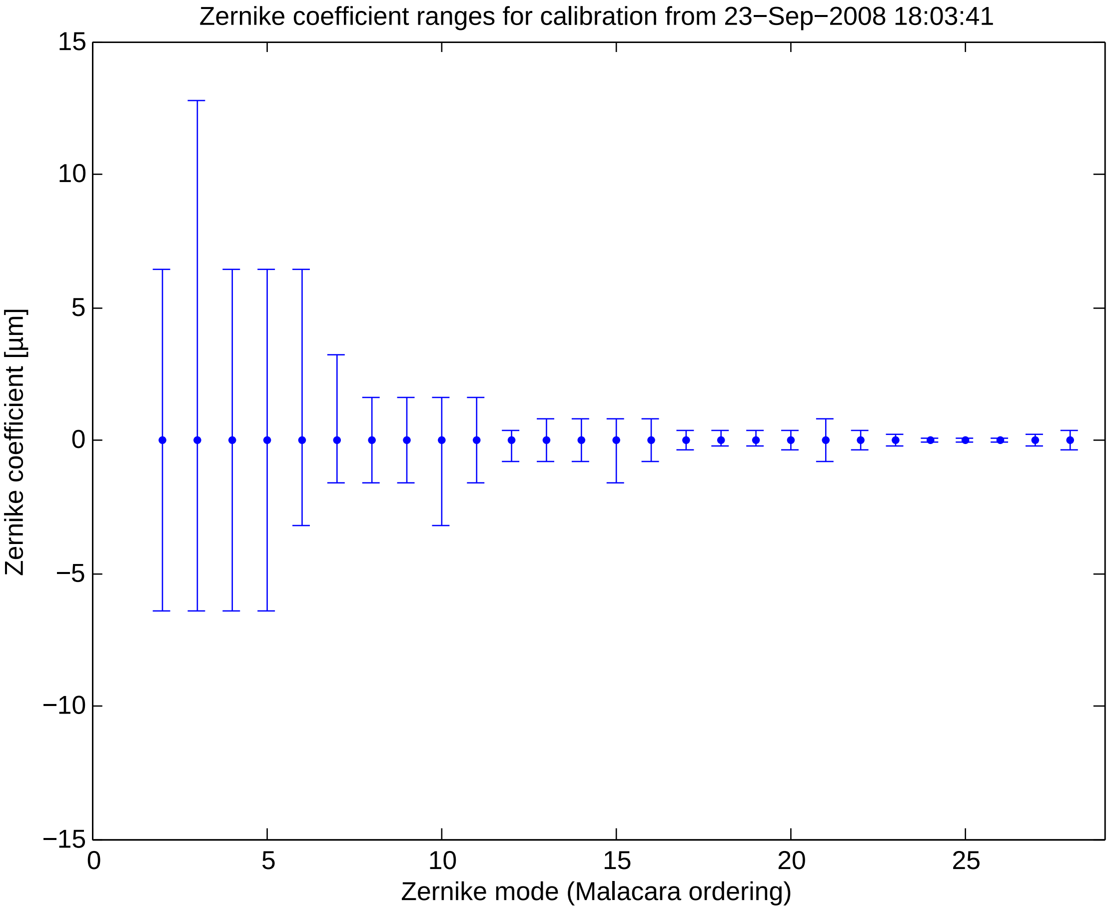

Figure 5.6. – Deflection limit of MIRAO 52-d for a wavefront quality criterion of iRMS$< 0.04\,\mu$m. In this measurement, only coefficient steps of $\frac{2^n}{10}\,\mu$m for increasing n were tried, implying that the actual deflection limits might be up to a factor of 2 larger than indicated here.

Optimizing the convergence stability

A measure for the amount of control the deformable mirror gives over the wavefront is the so-called condition number. In a sense, it is the ratio between the gain of the best-controllable and the worst-controllable system mode. Theoretical considerations [14] show that for optimal alignment of the MIRAO 52-d, condition numbers as low as 250 should be reachable. Even for the worst lateral alignment between lenslets and actuators, the condition number was calculated to be below 600 for systems where the number of lenslets across each actuator[5] lay between 2 and 4.

With the current setup, the number of Shack-Hartmann sensor lenslets across each actuator is around 3, well within the theoretically optimal range. However, from the influence function matrices measured, condition numbers in the order 14000 to 20000 were calculated. It is not clear where this large discrepancy comes from, so this might be a good starting point for further improvement to the system. The reason might well be that the theoretical model is not precise enough; it characterizes the influence functions of individual actuators as Gaussian surfaces and assumes a fill factor of 100% for the SHS lenslet array.

However, it might also be possible that conjugation of the deformable mirror and wavefront sensor needs to be more precise than was possible with the current alignment procedure, where a standard CCD camera was temporarily inserted to find the conjugation plane (see section 3.2). Since no theoretical estimate for the influence of incorrect imaging on condition number is available, one could try to systematically move the SHS along the axis and determine condition number as a function of axial position.

Given the large condition number, it seemed reasonable to try using filtering on the IFM to achieve better stability of the iteration algorithm for the wavefronts. To filter the IFM, a singular value decomposition was performed and all singular values below a cutoff were set to zero. The cutoff was selected as a percentage of the largest singular value, in order to guarantee a certain maximum condition number of the filtered matrix. In figure 5.7, convergence for spherical aberration is compared between the full IFM (condition number 14058, rank 52), and a filtered version where the rank was decreased to 41, with a condition number of 945. It is clear that the filtered matrix allows convergence to a stable residual error with only three iterations, whereas the unfiltered matrix has the tendency to oscillate, especially for larger desired coefficient values.

---

[5] measured along a straight line (personal communication with A. Dubra)

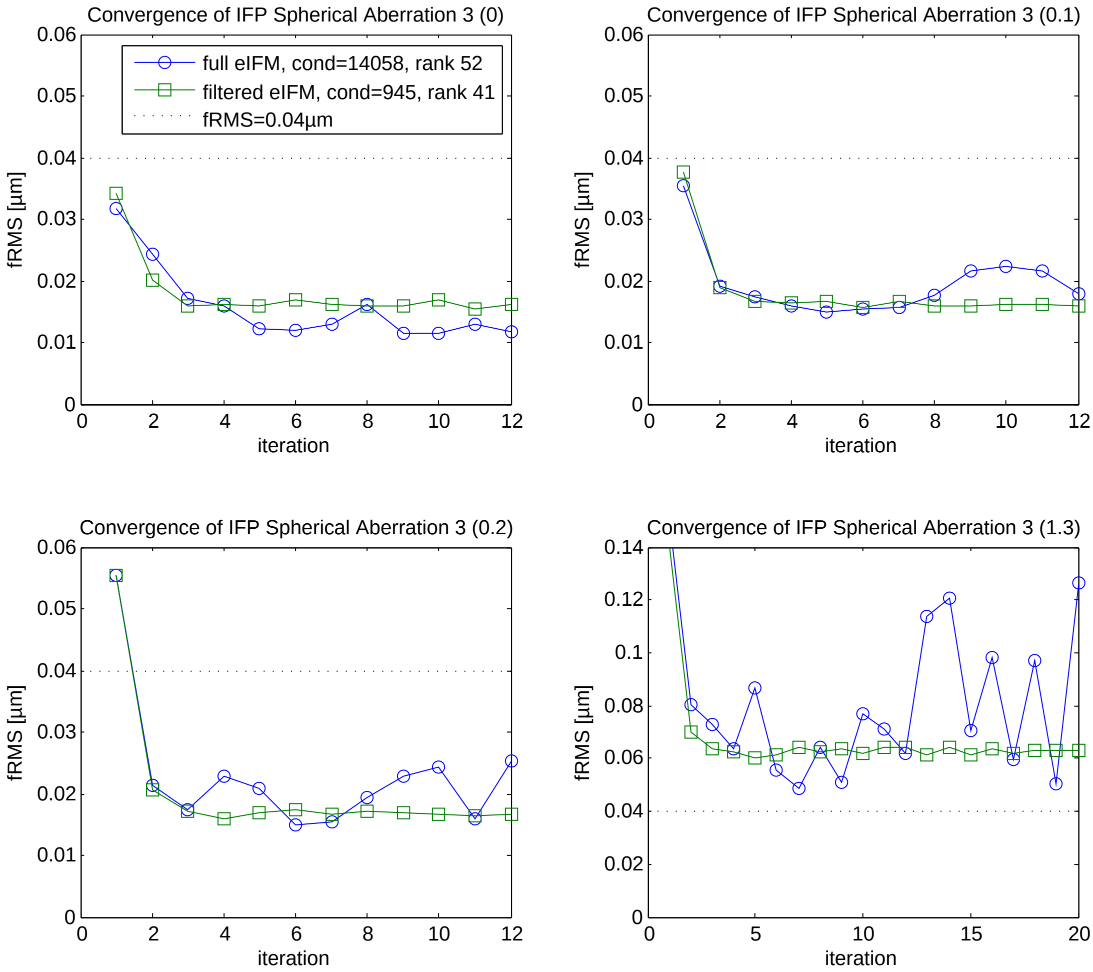

Figure 5.7. – Filtering the influence matrix can improve convergence. Iterations for a flat wavefront (top left) and 0.1 μm, 0.2 μm and 1.3 μm of spherical aberration are shown. Each wavefront was optimized using the full IFM, as well as a filtered one, showing more stable behavior with the filtered IFM.

To test the effect of filtering on the residual RMS achievable after iteration, filtered matrices with different condition numbers were used, see figure 5.8. It can be seen that the condition number can be decreased by one order of magnitude (corresponding to rank 41, i.e. removal of 11 of the 52 system modes) without loosing much control over the wavefront. Stronger filtering (down to condition number 238, rank 30) caused a significant increase in the residual error, indicating that system modes essential for good correction were also removed.

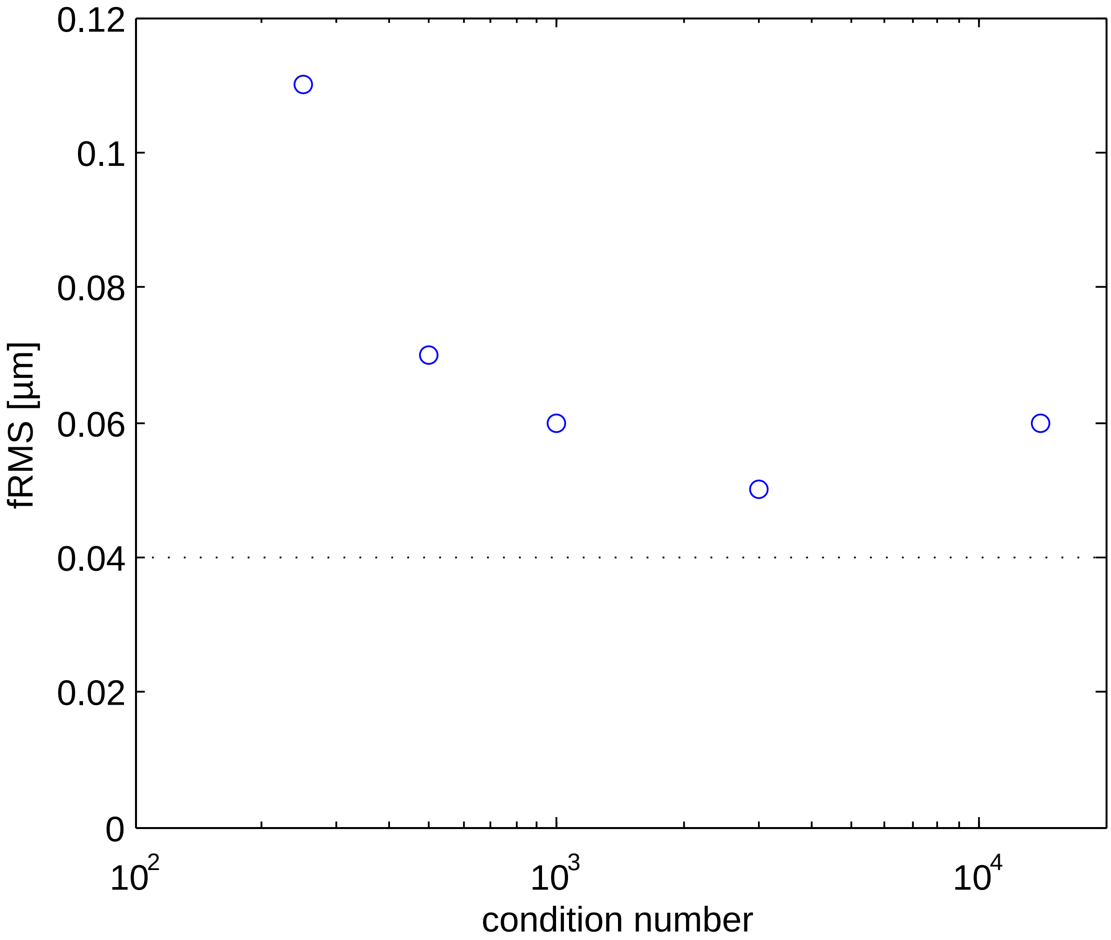

Figure 5.8. – The residual wavefront error achievable after 12 iterations with filtered IFMs depends on the amount of filtering, i.e. the condition number. Excessive filtering of the influence matrix decreases wavefront quality.

Wavefront quality after opening the control loop

As described in chapter 3, the setup did not allow closed-loop optimization during two-photon imaging. Instead, optimized voltages for certain wavefronts were determined in a calibration routine, and used for two-photon imaging several hours and sometimes days later. Due to possible thermal drifts of the system, it is important to check the validity of such pre-acquired voltages.

Reusing pre-acquired voltages In figure 5.9, the quality of wavefronts achieved for several Zernike modes is plotted against the desired coefficient value. The wavefront quality is given as the iRMS of the residual wavefront (difference between desired and measured wavefront). In the left panel, the minimal iRMS after 7 iterations is plotted. The corresponding voltages were stored and re-applied after 60 minutes (the time it took to finish the calibration procedure) and the wavefront quality was again measured; the corresponding iRMS is shown in the right panel.

Even though the iRMS values for many wavefronts increased, an increase beyond the maximum allowed iRMS value of $0.040\,\mu$m was generally only seen for the outermost IFPs, corresponding to the highest desired Zernike coefficient value and consequently the highest actuator voltages. For the coefficient value ranges predicted by theoretical calculations for each Zernike mode (see chapter 2), it does not seem to be a problem to reuse the IFPs after one hour. Other test measurements suggest that in principle, stability over several hours if not days is possible (data not shown). The manufacturer claims that room temperature changes are the main reason for undesired changes in mirror shape.

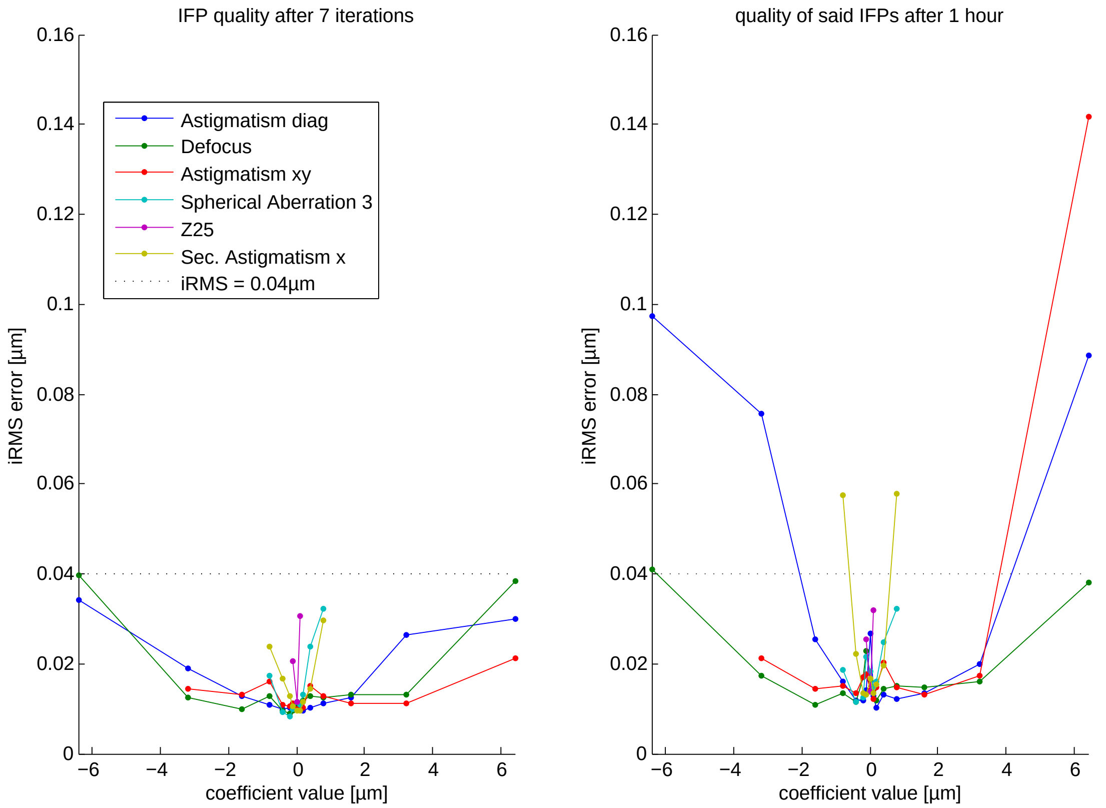

Figure 5.9. – (left panel) iRMS error for wavefronts containing different amounts of one of six Zernike modes. Best iRMS value after closed-loop optimization of control voltages is shown. (right panel) said optimized control voltages were reapplied after one hour to check whether they would still produce the wavefront quality. As can be seen, this was in general the case for small desired aberrations, but less so for large aberrations.

5.3. Interpolating between pre-acquired voltages

Since pre-acquiring voltages for all desired wavefronts would take excessively long[6] interpolation and extrapolation of voltages between IFPs is used. Here interpolation is used to refer to calculating voltages for a wavefront with one nonzero Zernike coefficient, for which IFPs with larger and smaller coefficient values are available. Extrapolation refers to calculating voltages for a wavefront with several nonzero coefficients, even though IFPs are only available for wavefronts were the corresponding modes were created separately instead of simultaneously (see section 4.1).

In figure 5.10, interpolation between astigmatism IFPs is demonstrated. On the x-axis, the desired Zernike coefficient (diagonal astigmatism, Malacara mode Z4) is plotted. Large rectangles and squares show the residual iRMS for IFPs acquired for this mode. Interpolation of voltages between neighboring IFPs was used to calculate voltages corresponding to coefficient values on a tighter grid; the iRMS for these wavefronts generated from interpolated voltages is shown as small circles and squares. For the circles, the distance between neighboring IFPs increased with distance from 0; more precisely, IFPs for $Z4 = \frac{2^n}{10}\,\mu$m were acquired. For the squares, the IFPs had a constant spacing of $1\,\mu$m along the Zernike coefficient axis.

It is clear that interpolation worked well for $1\,\mu$m spacing; for the variable spacing, wavefronts beyond $\pm 3.2\,\mu$m astigmatism were not generated faithfully. This is a sign of nonlinearities in the system[7] ; it still needs to be tested if this problem is equally serious for small desired Zernike values. Possibly a variable spacing where IFPs are closely spaced at high coefficient values, but more widely spaced near

---

[6] ~ 300 hours, calculated as follows: Assume we want to pre-acquire wavefronts which approximate a given wavefront down to $0.04\,\mu$m. If 3 modes (e.g. Z4, Z6 and Z13) are involved, that means that the errors $\Delta Z4, \Delta Z6, \Delta Z13$ have to have a RMS smaller 0.04, i.e. each has to be smaller than $\sqrt{.04^2/3} = .023\,\mu$m. To have maximum distance of .023 along one mode axis, the spacing has to be at most $2 * .023\,\mu\text{m} = .046\,\mu$m.

Covering $[-.9, .9]$ of sAb and $[-1.4, 1.4]$ in both astigmatisms, $(2*.9/.046)*(2*1.4/.046)^2 = 744188$ IFPs would have to be acquired.

Given the speed of 200 Hz of the mirror and assuming only 3 iteration steps, this would take 3 hours. Since our speed limit is the data transfer from the wavefront sensor to MATLAB (1Hz), a calibration would take at least 300 hours.

[7] For a linear system, the residual Zernike vector for interpolated voltages between two IFPs should be the interpolation of the residual Zernike vectors for the two IFPs. Since the quality criterion (iRMS) is an euclidean norm, it is convex and should give a quality of the interpolated wavefront which is no worse than the linear interpolation of the iRMS values of the IFPs.

zero, could improve the results. For the time being, constantly spaced IFPs were used.

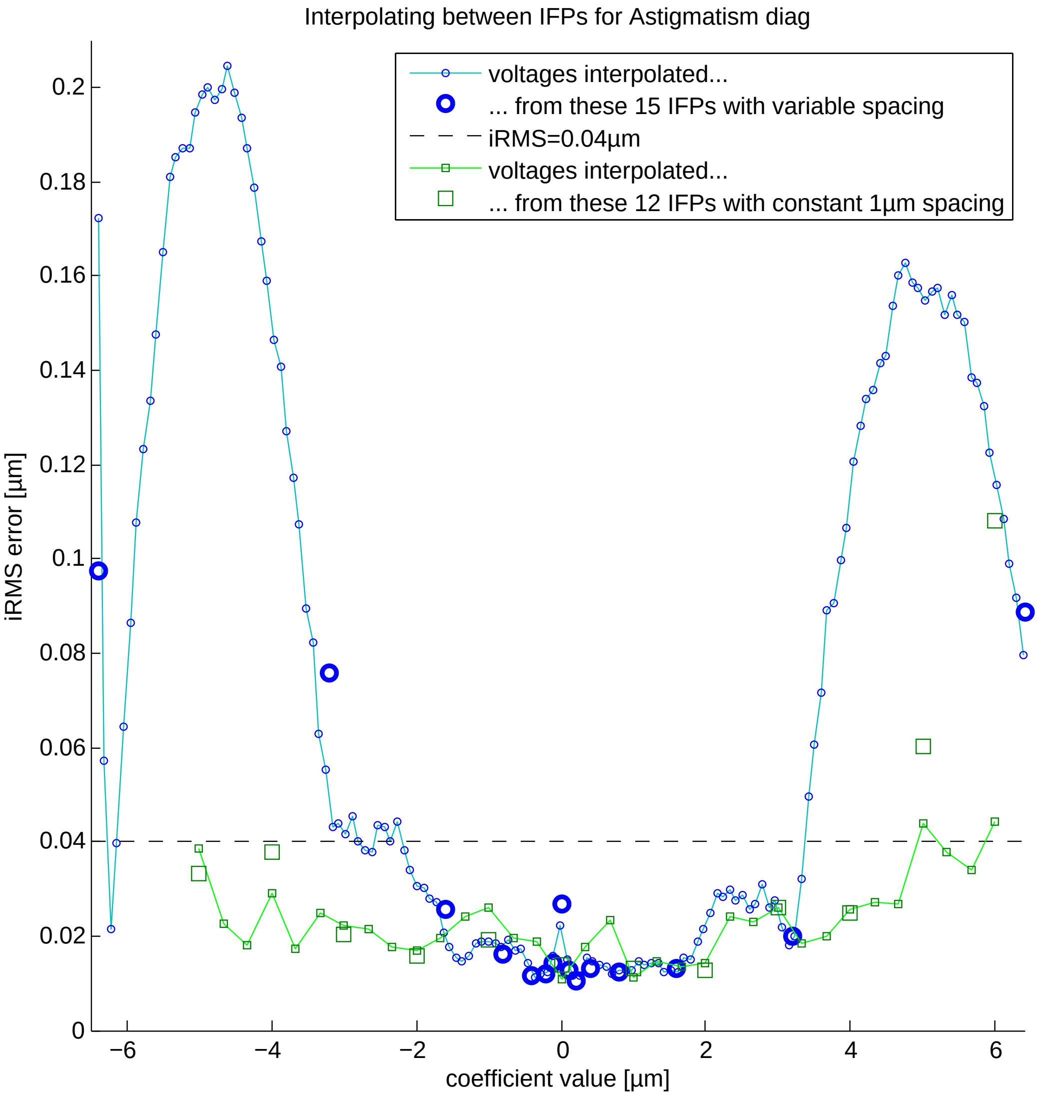

Figure 5.10. – Interpolation between IFPs is possible, but their spacing must not be too wide. A detailed discussion is found in the main text.

Extrapolating from pre-acquired voltages For wavefronts with more than one nonzero coefficient, extrapolation was used (see section 4.1). In figure 5.11, it is shown that this leads to catastrophic results if large coefficient values are generated. For example, a wavefront with only diagonal astigmatism of $-4\,\mu$m could be created with an iRMS below $0.04\,\mu$m($x = -4$ on dotted curve); a wavefront with only astigmatism along xy of 2 μm could be created equally well ($x = 0$ of thick solid curve). However, if these voltages were added[8] to get a wavefront with both diagonal astigmatism of $-4\,\mu$m and xy-astigmatism of $2\,\mu$m, the residual iRMS reached $0.17\,\mu$m (thick solid curve at $x = 4\,\mu$m). In comparison, the thin solid curve shows the residual iRMS for actual IFPs created for the wavefronts corresponding to the thick solid curve, i.e. with closed-loop iteration instead of open-loop extrapolation. The large discrepancy between both curves is due to errors introduced by extrapolation.

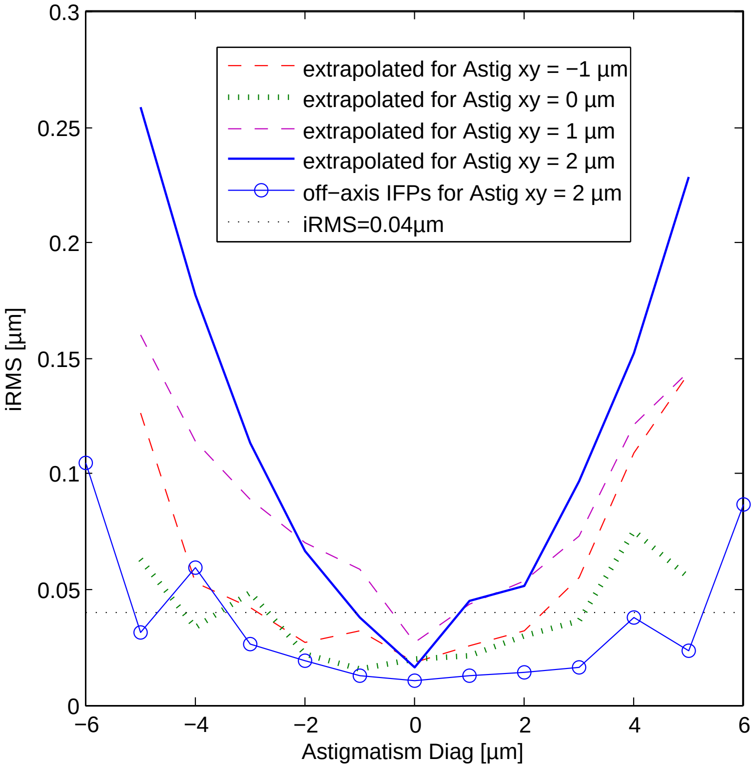

Figure 5.11. – Extrapolation at distance $2\,\mu$m from IFPs does not work, but at smaller distances it can work.

While extrapolation for large coefficient values is therefore not a good idea, for extrapolation between smaller coefficient values the results are mixed. For example, astigmatism xy $= -1\,\mu$m (lower dashed curve) could be combined with diagonal astigmatism of up to $\pm 2\,\mu$m without problems, while astigmatism xy $= 1\,\mu$m (upper dashed curve) did not quite satisfy the quality criterion. It is assumed that tighter spacing of IFPs and use of IFPs with more than one nonzero coefficient will allow this problem to be solved.

---

[8] taking into account the offset voltages for a flat wavefront

Settling time depends on change in power dissipation To analyze the effects of hysteresis and temporal stability, wavefront measurements over time were done with essentially the same voltages applied to the mirror, but different voltage history. Five situations were compared, according to the following scheme:

1. "last iteration voltages"
    - iterative optimization of voltages for a specific wavefront (7 iteration steps)
    - 30-100 seconds wavefront measurement for the voltages used in the 7th iteration step
2. "best voltages"
    - application of the optimal voltages (i.e. voltages from the iteration step which gave the best wavefront, which was not always the 7th step)
    - 30-100 seconds wavefront measurement
3. "best voltages after random voltages"
    - application of completely random voltages in the interval $[-0.5\,\mathrm{V}, 0.5\,\mathrm{V}]$
    - 2 second pause
    - application of the optimal voltages
    - 30-100 seconds wavefront measurement
4. "best voltages after inversed best voltages"
    - application of sign-inversed optimal voltages
    - 2 second pause
    - application of the optimal voltages
    - 30-100 seconds wavefront measurement
5. "best voltages after doubled best voltages"
    - application of doubled optimal voltages
    - 2 second pause
    - application of the optimal voltages
    - 30-100 seconds wavefront measurement

The five resulting trains of wavefront measurements are plotted in figure 5.12. The upper panel corresponds to a wavefront were one astigmatism was set to $2\,\mu$m and the other to $-2\,\mu$m; the two lower panels were both made for astigmatism coefficients of $4\,\mu$m and $-4\,\mu$m respectively. The experimental conditions for the lower two panels are identical except for the measurement time.

The curves for "last iteration voltages" and "best voltages" behaved quite as expected. In the first and third plot, they are almost identical, since the iRMS for

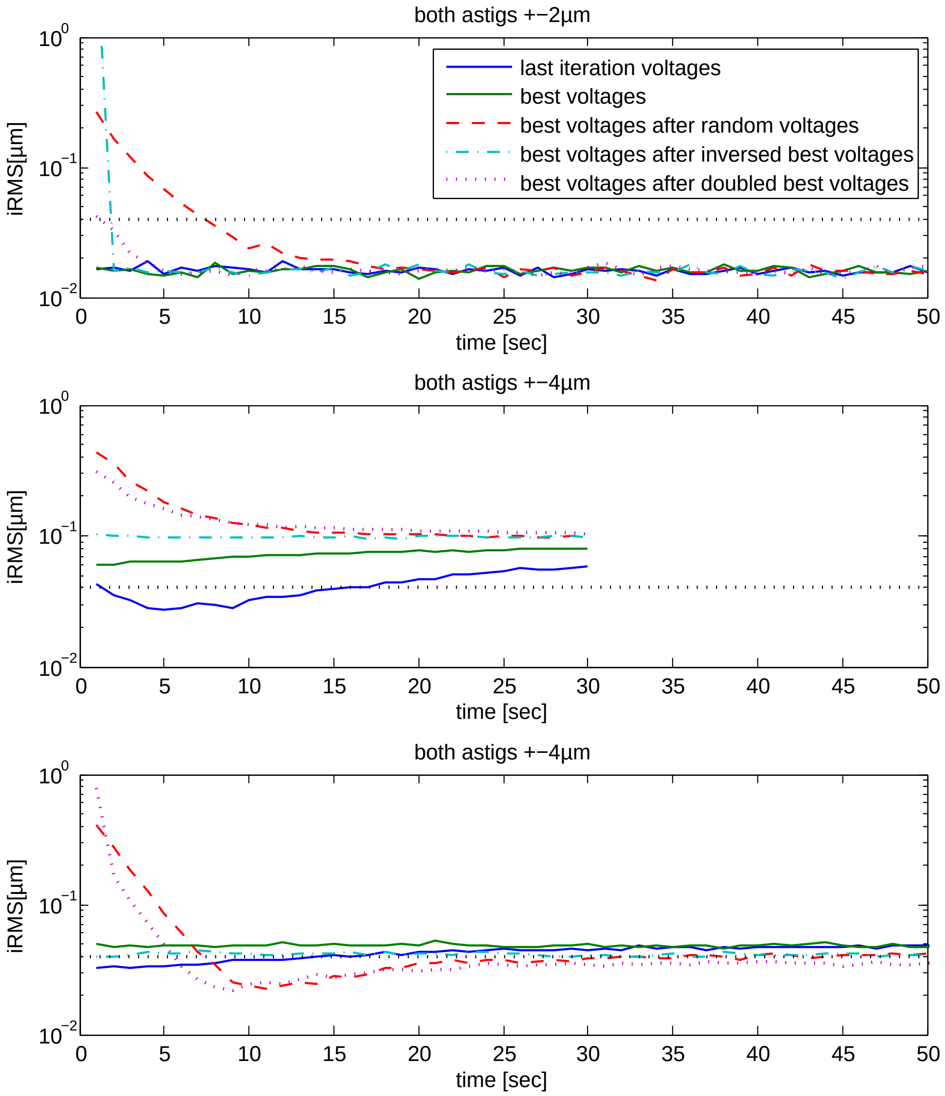

Figure 5.12. – iteration-based voltages have large settling time, if largely different voltages were applied before

the last iteration was not much different from the iRMS of the best iteration. In the middle panel, the 30 second measurement time seemed too short to reach an equilibrium state; the “best voltages” trace continues at the iRMS level where the “last iteration voltages” curve ended, which makes sense since these correspond to nearly identical voltages and measurement was continued with a pause of only one second.

In contrast, the dashed plots were rather disheartening: the previous application of random voltages for only two seconds caused the best voltages to give suboptimal wavefront quality for at least the next seven seconds; an effect caused mostly by slight overshooting of the nonzero coefficients (data not shown).

However, not all voltage changes cause such a long settling time. After two seconds with sign-inversed voltages (dash-dotted line), the optimal voltages perform as if nothing happened in all three measurements. The only exception, the very first data point in the top panel, is completely off the mark and is probably a measurement error[9].

Doubling the optimal voltages, on the other hand, has a similar effect as random voltages. It is notable that for the top panel, where the maximum doubled voltages lay in the range of 0.3V, the effect is a lot less pronounced than in the lower panels, where the limit of 0.5V was reached for some actuators.

In summary, it seems that the magnitude of the voltages applied plays a role. Since sign-inversed voltages produced no effect, but increased voltages did, it seems probable that the absolute value plays a role. This could mean that the power dissipation, proportional to the squared current, is the relevant quantity. A change in dissipation would cause the temperature of the coil to change, leading to a shape change of the mirror membrane.

While measurements with a fixed wavefront would not be affected by this, it is potentially a great problem for oscillation experiments, where the optimal Zernike coefficients for a given position in a sample are optimized by alternating between two different mirror shapes with fixed difference but variable mean. As long as the two wavefronts are symmetric around zero (in Zernike space), the voltages will also be roughly symmetric around zero; this corresponds to the dash-dotted line in figure 5.12 and poses no problem. However, as soon as the mean wavefront is

---

[9] This was most likely caused by unfortunate timing between mirror and wavefront sensor, causing the sensor to use data acquired even before the mirror has changed its shape. In most cases, discarding one measurement after sending new voltages to the mirror is enough to circumvent this problem, but due to the processing time needed by the WFS software, sometimes a second measurement is also affected.

in the order of the difference between the two wavefronts, the dotted line becomes relevant, meaning there can be a significant settling time.

If the shape oscillations are quick compared with the settling time, the coil temperature will presumably remain constant at a value corresponding to the average dissipation. However, this temperature will not correspond to the steady-state temperature of either mirror shape, but will be in between the two. Consequently, neither mirror shape will reach the precision it had originally.

Looking at the scale of the effect, the dotted trace in the upper panel shows that for the oscillation amplitude of $2.8\,\mu$m[10] used there, the initial iRMS is barely above the desired limit of $0.04\,\mu$m. Since realistic oscillation amplitudes are a factor of two to five and realistic mean wavefronts at least a factor of two smaller, it can be expected that this effect will not make the use of oscillation impossible[11].

Summary In closed loop, the system is able to generate the necessary mirror shapes, which are stable over at least 20 minutes. Storing the optimal voltages for later use is possible, even though large voltages tend to not reproduce the desired mirror shape as well. Interpolation between IFPs is possible in the coefficient range needed, in contrast to extrapolation, which has failed in some cases. Creation of IFPs in the whole relevant multidimensional Zernike coefficient volume instead of only on the axes can hopefully solve this problem. A settling time of up to 15 seconds needs to be considered when large changes are made to the mirror voltages.

---

[10] $\sqrt{(2\,\mu\mathrm{m})^2 + (-2\,\mu\mathrm{m})^2}$, since the two astigmatism coefficients add quadratically

[11] For a reliable quantification of the effect on the relevant sub-second timescale, the wavefront data acquisition needs to be sped up, see footnote on page 47.

5.4. Two-photon microscopy measurements

While characterization of the deformable mirror in terms of wavefronts generated is an important stepping stone, the real benchmark for the current project has to be the imaging quality and signal level achievable in two-photon microscopy. Unfortunately, most of the two-photon experiments have been done before some of the characteristics of the adaptive optics system had been correctly measured. In particular, the measure used to judge "good" wavefronts had been too lax while at the same time taking into account tip/tilt and defocus, which play a minor role for image quality on the relevant scale.

While the mirror characterization measurements presented in the previous section were all repeated with the more strict quality measure (iRMS $< 0.04\,\mu$m), time did not permit to repeat all 2P experiments. Data in this section has therefore to be considered preliminary in the sense that iRMS wavefront quality is not known in most cases; where it is known, the iRMS was in some cases a factor of 7 too high, but the contribution from non-optimized modes was still below $0.07\,\mu$m[12].

5.4.1. Aberration-free sample

The effect of wavefront manipulations in an aberration-free sample was tested. As a simplest possible system, the objective was immersed in fluorescein dissolved in water, which allows the measurement of the spatially integrated excitation efficiency. Since the absolute fluorescein concentration was not determined, only relative measurements were possible.

In figure 5.13, the influence of individual Zernike modes (second to sixth radial order) on total fluorescence level was investigated. Three groups of curves can be distinguished: Defocus has nearly no effect on fluorescence in the coefficient value range shown; low order aberrations show a moderate dependence, while higher order aberrations (with radial order at least 5, but angular order of at most 4) show a much stronger dependence. When applying sufficiently large aberrations

---

[12] The reasoning is that any mode which was optimized in a particular experiment should not be considered for the calculation of the residual error: even though the value displayed on screen might not be the same as the one actually applied, what counts is that a continuous and monotonous change of the actual value was possible to find the optimum. In a sense, the precision with which the optimum for each coefficient was determined gives the error for that coefficient. This error value should therefore be included in the calculation of iRMS, not the difference between displayed and actual coefficient value. For non-optimized modes, an optimum of zero is assumed, so that any non-zero measured coefficient value would have to be considered part of the iRMS error.

(1...3 μm), all aberration modes (except defocus) can cause a decrease of the signal level to below 20% of the peak (data not shown).

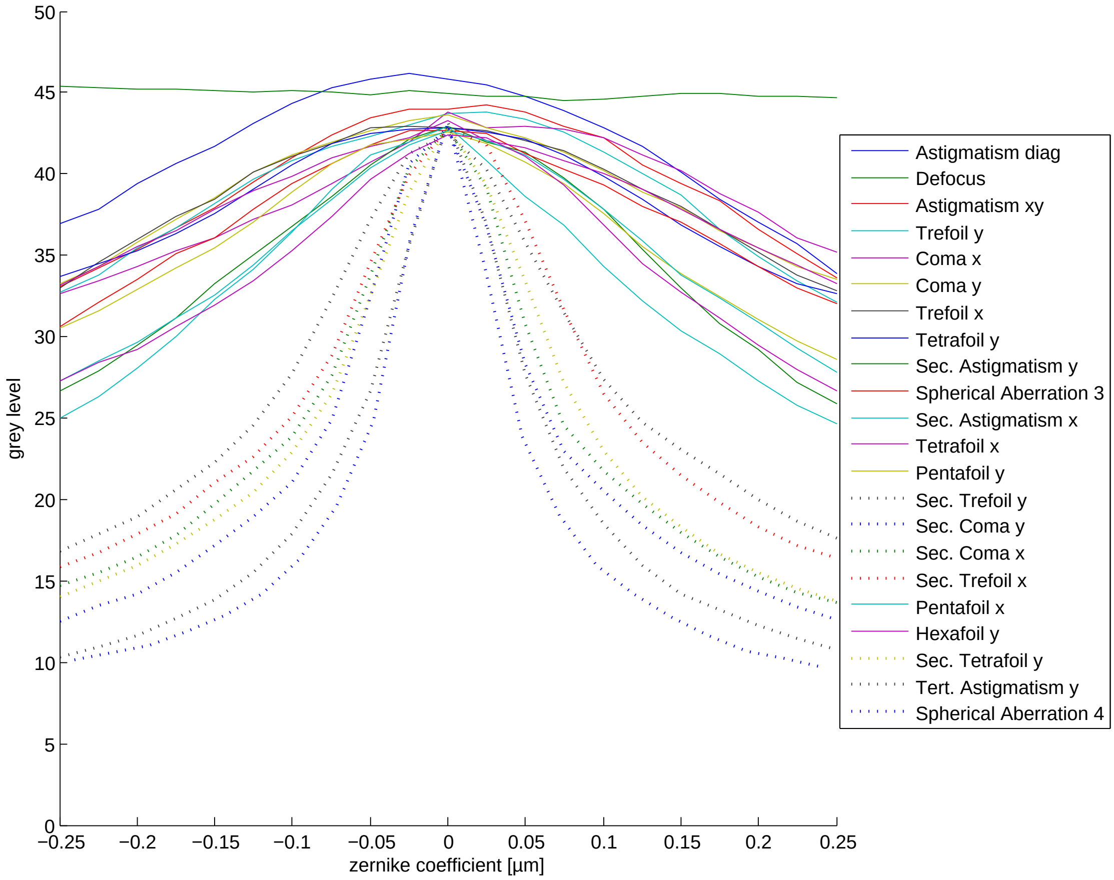

Figure 5.13. – fluorescence in fluorescein for different Zernike modes. The fact that not all curves show the same intensity at x=0 (corresponding to a flat wavefront) indicates that there is some measurement error involved; either due to settling time or hysteresis of the mirror, or due to laser intensity drifts. The Zernike mode calibration used had been defined for a back focal aperture diameter of 17.5mm, even though the objective (Zeiss 20x 1.0W) only had an aperture diameter of 16.2mm.

5.4.2. Astigmatism in a fluorescein-filled glass capillary

To test the ability of the setup to correct astigmatism, a sodium borosilicate glass capillary (outer diameter 1mm, nominal wall thickness 0.150mm) was filled with fluorescein. Both astigmatism modes as well as spherical aberration were varied continuously, and the resulting fluorescence recorded (figure 5.14. A slight improvement of fluorescence for both astigmatism modes[13] was found when they were optimized separately (× and + curves). However, when astigmatism xy (90°) was set to its optimal value and diagonal astigmatism (45°) optimized again ($*$ curve), a much stronger peak was found.

This illustrates nicely the problem when optimizing multiple coefficients: Aberrations present in one mode will not only decrease signal, but also make the effect of any other aberration mode a lot less pronounced. In biological samples, where data quality is expected to be a lot worse than in this fluorescein sample, this might make it very difficult to correct properly. When several coefficients are far from their optimum, the intensity curves might end up flat enough to disappear in the noise.

With astigmatism uncorrected, introducing spherical aberration (empty circles) had a rather weak effect on fluorescence with a slightly tilted plateau around zero. Once the astigmatism coefficients were set to their optimized values, spherical aberration produced a very steep curve (empty triangles), with a pronounced peak at $0.06 \pm 0.06\,\mu$m. If the wall of the capillary (nominal thickness 150 μm) had been flat, around $0.25\,\mu$m spherical aberration would have been expected. It is surprising to have such a large discrepancy, but the curvature of the glass is in the correct direction to decrease the effect of spherical aberration.

To illustrate the fact that astigmatism under a curved surface depends on depth, fluorescence depth profiles were taken at the center of the glass capillary for different values of astigmatism. For this experiment, the capillary was aligned to correspond well to one of the astigmatism modes, so that only a one-dimensional optimization was necessary. The depth profiles are found in figure 5.15, where a depth of $\sim 50\,\mu$m corresponded to the upper glass-fluorescein interface, $400\,\mu$m corresponded to the center of the capillary and $\sim 750\,\mu$m corresponded to the lower fluorescein-glass interface.

Since the effect of depth on detection efficiency has not been investigated, it is not straightforward to compare the intensity acquired at different depths. Looking at a fixed depth, some aberration values produce more fluorescence than others. Which

---

[13] The capillary had not been oriented in any special way relative to the x-y-axes of the adaptive optics.

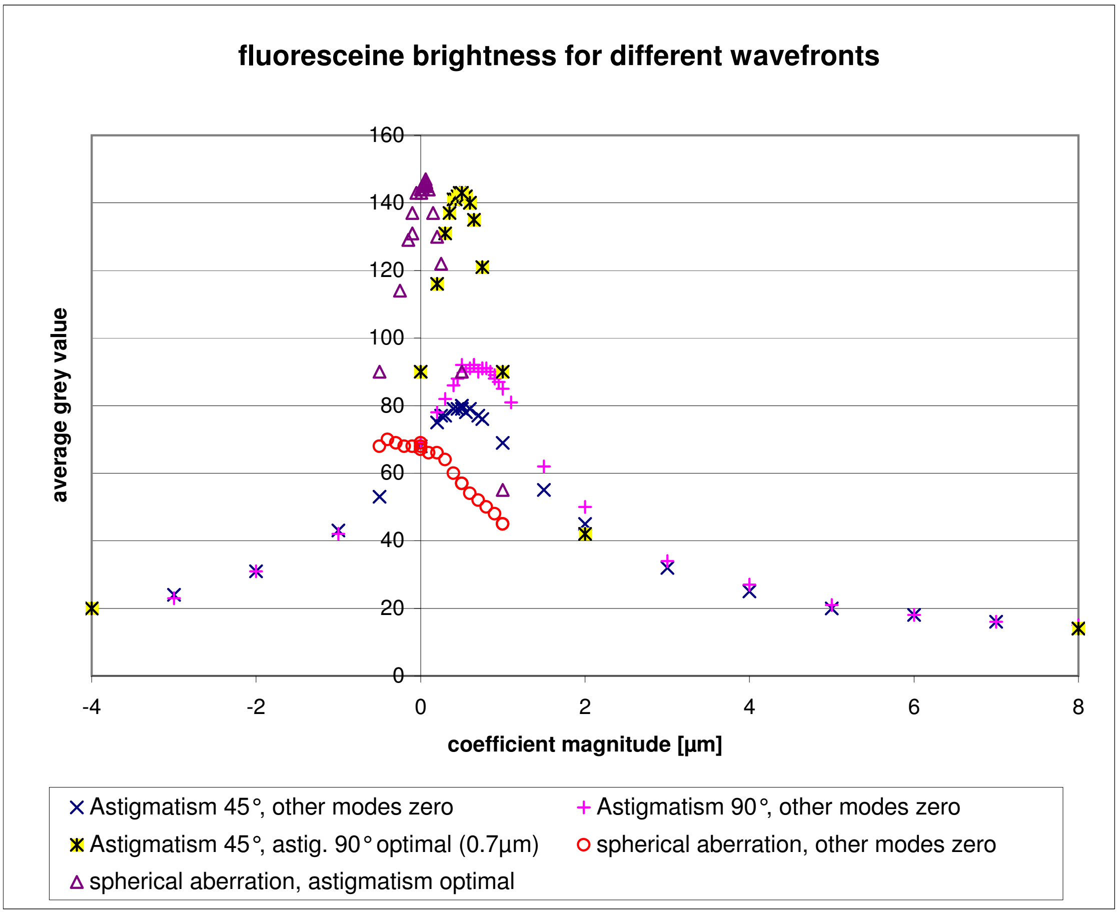

Figure 5.14. – Fluorescence of fluorescein inside a glass capillary can be improved by preempting aberrations. The data points labelled +, × and ∘ correspond to independent variation of either one astigmatism mode or spherical aberration, with all other coefficients zero. The data points labeled with ∗ correspond to variation of astigmatism 45° with astigmatism 90° fixed at its optimal value. Similarly, Δ data points correspond to variation of spherical aberration with both astigmatism coefficients fixed at their optimal values ($Z4 = 0.5\,\mu$m, $Z6 = 0.7\,\mu$m).

amount of aberration correction is optimal changes with depth: For positions close to the glas surface (both top and bottom), -0.5 μm were optimal. A bit further in, this low amount of correction was not very helpful any more, and a value of -0.86 μm was optimal. In the central part of the capillary, -1.1 μm provided the best correction. In total, looking at the envelope of all curves, it seems that almost constant signal level from different depths of the capillary could be obtained if the correction was adjusted continuously. Only a 10% drop with depth over 750 μm was observed, which could be caused by changes in detection efficiency, or residual uncorrected aberrations. For the center of the capillary, an estimation of the astigmatism coefficient[32] is $\sim 2.6\,\mu$m, which is more than a factor of two larger than the value $1.1 \pm 0.4\,\mu$m found here.

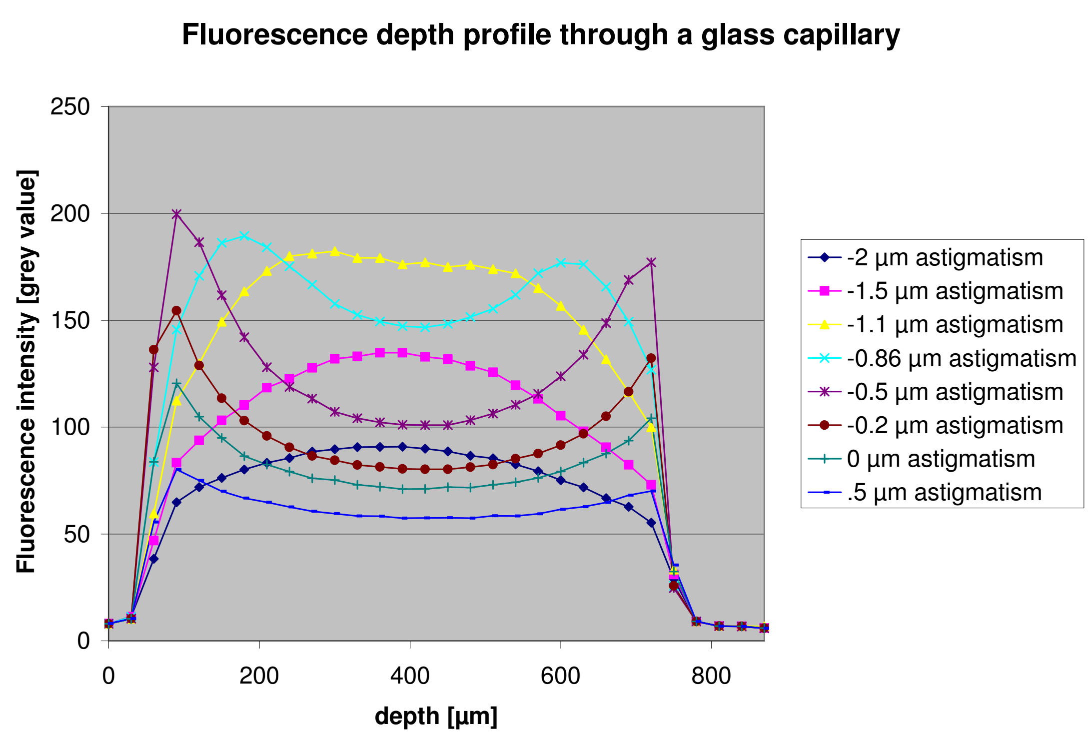

Figure 5.15. – Depth profiles through the center of a glass capillary for different amounts of astigmatism.

5.4.3. Compensation of spherical aberration caused by glass

Fluorescein

Next, the ability to correct for spherical aberration was investigated (figure 5.16). Due to its higher radial order, this proved to be more difficult than the correction of astigmatism, in the sense that proper alignment of the wavefront sensor with the back focal plane had to be performed more carefully. Using a microscope slide as an aberrating glass layer of 1mm thickness, the introduction of 0.52 μm spherical aberration increased fluorescence by 50% over the value found for a flat wavefront. For comparison, applying 0.25 μm or 0.75 μm only provided about 15% signal improvement. Apart from signal level, the point spread function of the system should also be improved by correcting spherical aberration. Scanning across the edge of the glass slide, from glass into fluorescein, showed a steeper edge when spherical aberration was corrected than in the uncorrected configuration. This illustrates an improvement in z resolution, as expected.

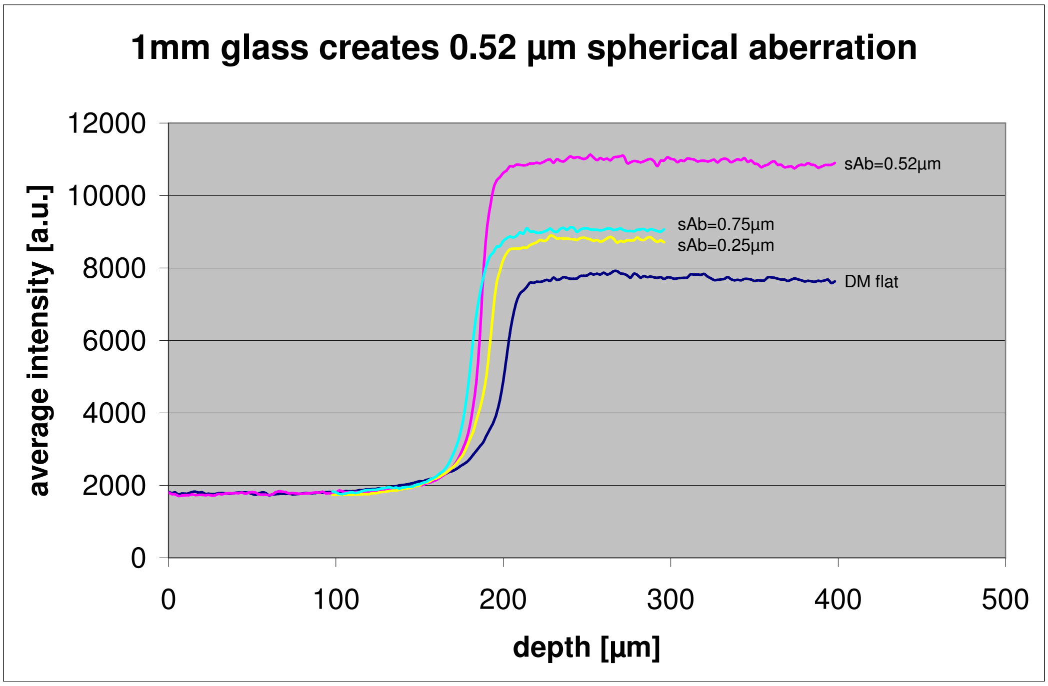

Figure 5.16. – Depth scans across the interface between aberrating glass layer and fluorescein solution, for different amounts of spherical aberration. $sAb = 0.52\,\mu$m gave optimal fluorescence; for illustration, curves for a flat wavefront as well as over- and under-correction are also shown.

The dependence of the optimal Zernike coefficient on the amount of aberrating glass was determined in a separate experiment, as shown in figure 5.17. Even though theory predicts a linear increase of spherical aberration with glass thickness, a leveling off of this effect is observed. Not even the initial slope (experimentally around 1 μm/mm gets close to the theoretical value of 1.6 μm/mm.

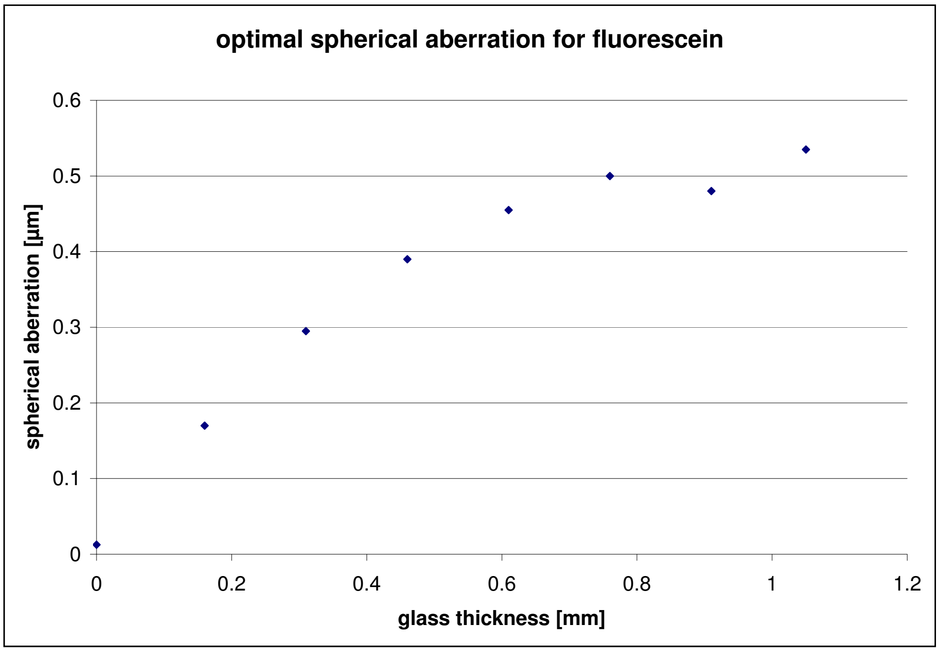

Figure 5.17. – Spherical aberration versus glass thickness. For different amounts of glass, the optimal wavefront with respect to bulk fluorescence in fluorescein was determined.

To compare the improvement the adaptive optics system can bring, the performance was compared between deformable and non-deformable mirror (figure 5.18). It can be seen that the “flat” deformable mirror produces slightly lower signal than the nDM[14]. However, under 1mm of glass, the optimization of the wavefront shape produced up to 100% signal improvement over the nondeformable mirror. Once the glass was removed, this optimized wavefront “DMopt1” performed nearly a factor of three worse than a flat wavefront, illustrating that the wavefront indeed corrected for aberrations created by the glass.

Comparing the signal level after aberration compensation with the unaberrated case, it is clear that the full signal level has not been restored. The decrease

---

[14] ...for constant total power under the objective, achieved by adjusting the laser intensity to compensate for the different reflectivity of DM and nDM.

might be due to residual wavefront error, as well as reflection of excitation and fluorescence light at the two glass-water interfaces.

One problem which also became evident during this and other measurements is an effect introduced by the objective. In fact, the flat wavefront from the nDM is not the optimal shape to maximize fluorescence when an excitation wavelength above 800 nm is used. Some amount of defocus could actually increase fluorescence beyond the level achievable with a flat wavefront (data not shown). The objective manufacturers confirmed that at 915 nm, as in this experiment, a slight improvement in fluorescence can be achieved by illuminating the objective back focal plane with a non-collimated rather than a collimated laser-beam[15].

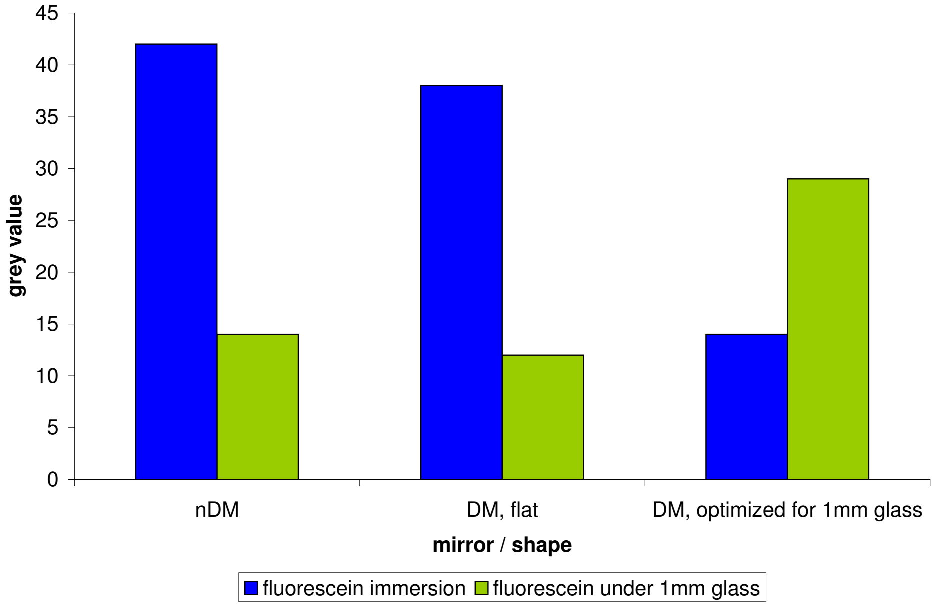

Figure 5.18. – Comparing the signal level achievable in fluorescein with the nDM and the deformable mirror, with and without aberrating glass layer (1mm). For the DM, two different wavefront shapes are analyzed, the best achievable flat wavefront and the wavefront optimized for signal level in the presence of 1mm glass.

---

[15] For the Zeiss objective, a divergent wavefront was experimentally determined to be optimal; no quantitative answer from the manufacturer has been received so far. For the Leica objective, a slightly convergent beam is optimal; according to the manufacturer, the beam waist should be 23m from the objective mounting surface, which will produce a residual RMS of $0.012\lambda = 0.011\,\mu$m.

Beads

In figure 5.19, the influence of spherical aberration on the fluorescence of 1 μm beads under 750 μm of glass was investigated. To estimate the peak intensity while decreasing noise, the grey value of a region of interest centered on the bead was averaged. It can be seen that the brightest fluorescence can be found around 0.4 μm spherical aberration, with a 33% to 50% improvement over a flat wavefront for three different beads from three different sets of z-stacks. Comparing with integrated fluorescence (figure 5.17; both measurements were done on the same day and with the same mirror calibration and beam path alignment), the optimum for peak fluorescence is found at a smaller Zernike coefficient value.

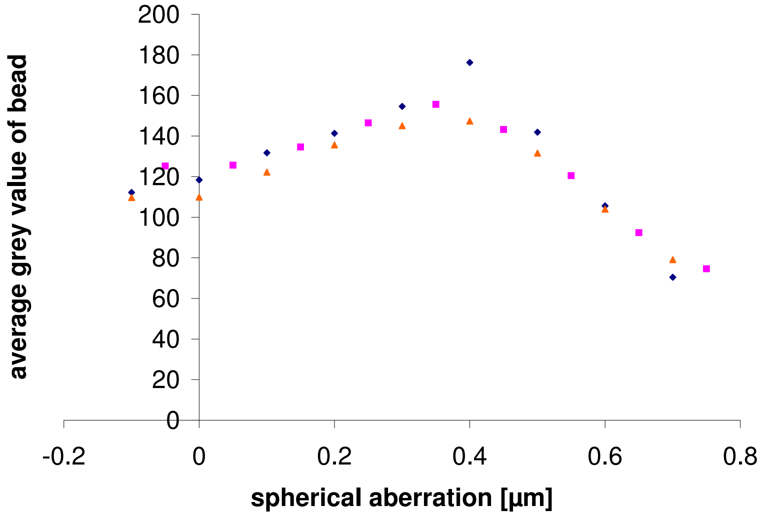

Figure 5.19. – Three beads under 750 μm glass show significantly increased fluorescence for positive spherical aberration of 0.4 ± 0.1 μm.

Since higher order modes were not corrected, it is in principle possible that the optimum for peak and integrated fluorescence are found at different values. However another reason could be that all three data stacks were recorded with monotonically increasing spherical aberration values, so that bleaching could give a bias towards smaller coefficient values. Even though bleaching did not appear to be a major problem with the 1 μm beads used, it is certainly more significant than with the fluorescein solution, where diffusion from the large total volume ensures long-term stability of fluorophore concentration.

5.4.4. Compensation of spherical aberration caused by refractive index mismatched sample

For brain tissue, the expected refractive index mismatch is at the second decimal (see section 2.1). To illustrate experimentally the theoretical finding that even such small mismatches can cause significant aberrations, 1 μm beads in agarose gel were studied. Enough sucrose was added to reach a refractive index of $n = 1.37$, corresponding to 30g sucrose per 100ml gel. The dependence of peak bead intensity on depth below surface was studied. To separate the $n = 1.37$ gel from the $n = 1.33$ immersion medium, a cover glass (150 μm) had to be used. According to figure 5.17, a single cover glass adds 0.17 μm spherical aberration. Assuming linear summation of the optical path differences caused by glass and gel, 1000 μm of gel contribute the remaining 0.13 ± 0.1 μm of the fluorescence peak found (figure 5.20) at 0.3 μm spherical aberration. Comparing this value of 0.13 μm to the theoretical prediction of 0.54 μm, the experimental value is again too small, by about a factor of 4.

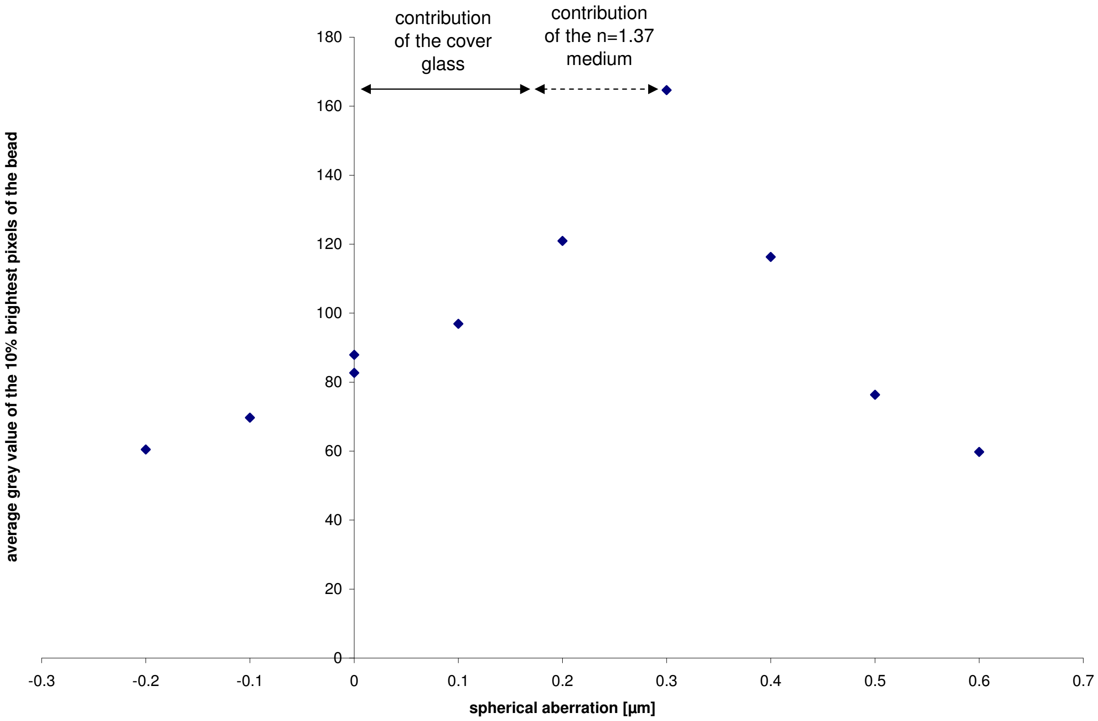

Figure 5.20. – Beads embedded in sugar-containing agarose gel with n=1.37, at a depth of 1000 μm under a 150 μm cover glass, imaged with different amounts of spherical aberration. Peak fluorescence is optimal at spherical aberration of 0.3 ± 0.1 μm.

5.4.5. Summary

The optimal correction values for spherical aberration and astigmatism in a variety of systems has been measured. Either fluorescein solved in water or 1 μm beads were used as samples. Aberrations were introduced by a curved layer of glass (capillary), plane-parallel glass (cover glasses or object slides) and sugared agarose gel with refractive index of 1.37. The experimental results (c_{ex})of all these measurements are summarized here and compared with theoretical calculations (c_{th}).

mode	**sample**	**aber. src.**	c_{ex} [nm]	c_{th} [nm]	c_{th}/c_{ex}	**see fig.**
sAb	fluorescein	capillary	60 ± 60	246	4	5.14
astig	fluorescein	capillary	1100 ± 400	2600	2.4	5.15
sAb	fluorescein	glass	106	160	1.5	5.17
sAb	fluorescein	glass	540	1600	3	5.17
sAb	beads	glass	400 ± 100	1230	3	5.19
sAb	beads	n=1.37 gel	130 ± 100	540	4.2	5.20

6. Discussion

6.1. Refocusing reduces aberrations

There exists extensive literature[15, 35, 36] treating the effect of refractive index mismatched samples, generally assuming a flat sample surface. However, most of these publications are concerned with quantifying the effects in terms of Strehl ratio or resolution, but only few[6, 3, 42] with the actual wavefront which corresponds to the aberrations. Such a representation, for example in the form of Zernike coefficients, only became relevant with the advent of adaptive optics in microscopy. Here, it is the basis for correction of aberrations by introducing a conjugated phase profile in the incoming light path.

Due to the limited spatial frequency capabilities of most correction elements, it is of interest to know the amount improvement which can be achieved when correcting only low order aberrations. [6] quantified this effect for water-based samples under an oil-immersion objective. However, moving the actual focus position relative to the objective was assumed to correspond to Zernike defocus in that publication, whereas recent results present a somewhat refined picture. [9] coined the term “high-NA defocus”, which refers to the wavefront necessary for an axial shift of actual focus position, and which was found to contain not only Zernike defocus, but all orders of spherical aberration. They presented high-NA defocus in the context of fast remote refocusing, independent of adaptive optics.

We were unable to find a synthesis of high-NA defocus and aberrations caused by a planar refractive index mismatch in the published literature. Equation 2.15, which represents such a synthesis, is derived here as a special case of an implicit formula for calculating the wavefront aberrations for a spherical refractive index mismatched surface. It allows calculation of aberration-preemption wavefronts containing an arbitrary amount of high-NA defocus. Since high-NA defocus contains all orders of spherical aberration, it can in fact be used to partially compensate aberrations. Instead of fixing the actual focus position at the nominal focus position or at the paraxial shifted focus position, this free parameter is optimized to minimize wavefront RMS, reducing expected coefficient values for spherical aberration by 35% to 50% depending on the system (refractive indices, NA) studied.

Extending beyond sample geometries with rotational symmetry[34], attempts were made to calculate Zernike coefficients for cylindrical and ellipsoidal sample geometries. Two approaches were used, namely fitting to data from two-dimensional ray traces and 3D ray traces created with Optica3. In compilation of this written report, systematic problems with both approaches were found, which were discussed in section 2.4. The obtained values are therefore only order-of-magnitude approximations. More precise results could be obtained by straightforward three-dimensional ray tracing, taking the full model of a sine-condition objective into account.

In terms of improvements to be gained from adaptive optics for two-photon imaging in 1mm depth, figure 2.7 suggests that there is considerable intensity improvement to be expected. For point-like objects, up to a factor of 20 can be expected, while for objects much larger than the point spread function, a gain of factor 3 can still be expected for perfect correction of all orders of aberration. Correction of lowest order spherical aberration alone should already bring a factor 2 improvement. In conclusion, it should in principle be worthwhile to implement adaptive optics into a deep-imaging two-photon microscope setup.

6.2. Experimental wavefront control

A deformable mirror for wavefront control and a wavefront sensor for calibration of the deformable mirror were integrated into a two-photon microscope. Electronics and software were created or modified to allow smooth interaction of all components.

The wavefront quality of other publications[4, 32] was not achieved, partly due to the low-cost wavefront sensor used. Nonetheless, the residual wavefront error achieved ($0.04\,\mu$m) is one order of magnitude lower than expected aberrations and should allow a Strehl ratio of 92% to be reached.

A mayor drawback of the setup is the inability to operate the wavefront sensor and deformable mirror in closed loop during microscopy. Control voltages for different mirror shapes need to be determined in a calibration step, before switching to two-photon imaging. Interpolation between control voltages determined for different mirror shapes was successfully used to reduce the number of calibration points necessary.

Extrapolation[1] was also used, but was found to cause prohibitively large wavefront errors in a recent control measurement. Further measurements are necessary to decide whether calibration data points on the Zernike vector space axes are really sufficient, or whether calibration points need the be distributed more evenly over the relevant Zernike vector space subvolume.

A second issue which is still unresolved is the ability to use pre-acquired voltages for quick oscillation between two wavefront shapes, for operation in lock-in amplifier mode. Recent measurements (figure 5.12) suggest that such an operation mode will increase residual wavefront error, most likely due to temperature changes caused by the different power dissipation at different voltage levels. Restriction of oscillation amplitude (and thereby voltage difference between wavefront shapes) might be a feasible way to reduce this problem, but more measurements are necessary.

6.3. Even in theory, fluorescence has complicated dependence on aberrations as they get large

It has been shown (sections 2.3.4 and 2.4) that aberrations beyond 0.25 μm and up to about 1.3 μm are to be expected in the biological system of interest, corresponding to $\frac{\lambda}{4}$ up to 1.4λ. For aberrations of this size, peak excitation intensity does not fall of quadratically with the RMS of the aberrated wavefront any more (figure 2.4), as is the case for small aberrations in accordance with [8]. A different formula for intensity drop has been suggested in the literature[43], claiming validity over a wider range of aberrations. Whether this formula would be sufficient to describe the dependence of fluorescence on aberrations found here still remains to be investigated.

Total fluorescence falls off even slower than peak fluorescence (figure 2.5). Interestingly, total fluorescence reacts differently to the same amount of aberration, depending on which Zernike mode is used. For peak fluorescence, this effect was also present, but less significant, making it possible that it was caused by numerical inaccuracy. For total fluorescence, it seems that aberration modes can be separated into two groups, some with stronger and others with weaker influence on fluorescence. These groups were marked by solid and dotted lines respectively.

---

[1] Extrapolation has a slightly non-standard meaning here; it refers to calculation of voltages for wavefronts with more than one nonzero Zernike coefficient, on the basis of calibration data where only single Zernike coefficients were nonzero. Technically, this should only be called extrapolation for cases where the desired wavefront lies outside the convex hull of the calibration points used, which is usually, but not always, fulfilled here. For details, refer to section 4.1, in particular figure 4.2c.

The normalization used (according to [27]) was defined precisely to make the effect of all modes equal, in this case the effect on the RMS. The reasoning was that RMS provides a metric for wavefront quality. As we have seen, the same RMS in different modes does not, for two-photon microscopy, have the same effect on bulk fluorescence. Since we are ultimately interested in the effects on fluorescence, it would in the future be preferable to use a different normalization of individual modes. If optimization for structures large compared to the point spread function(for example, soma) is desired, a scaling should be used where the total fluorescence is affected similarly by all modes. If, on the other hand, fluorescence from point objects (like individual stained synapses) are to be optimized, the normalization would need less modification, since this property is affected similarly by all modes according to figure 2.4.

Before such a renormalization based on theoretical calculations of fluorescence signal is attempted, one issue should however be addressed. All calculations presented here were based on the (scalar) Debye integral. According to [29, chapter 11], for marginal ray angles beyond 30°, the full vectorial theory[31] should be used. In the present case (NA 1.0 water objectives), marginal ray angles are at 48.8°.

The same flaw also affects calculations for the interaction between different orders of spherical aberration presented in figures 2.6 and 2.7. The size of a few orders of spherical aberration was calculated without low-angle approximations. The resulting wavefronts were then used to calculate point spread functions, again using the Debye integral. Crosstalk between the effect of different orders on fluorescence was found on the aberration scale relevant for deep imaging in the brain, implying that the Zernike modes are not correctly balanced. It is unlikely that PSFs calculated with the vectorial theory[31] will by a miracle compensate this crosstalk, since the derivation of correct balancing is based both on the paraxial approximation and the assumption of small amounts of aberrations[8]. Nonetheless, a significant modification in the strength of crosstalk by the vectorial theory is likely.

Some work on cross-talk between different Zernike modes has been done as early as 1963[22]. [11] give a general scheme for deriving correctly balanced (crosstalk free) aberration modes for particular imaging techniques, presented in the context of structured illumination microscopy. It was realized too late in the course of this project that cross-talk plays a significant role in two-photon microscopy at the scale of aberrations present here. Correct treatment of this issue is one of the mayor open points of this project.

6.4. Experimental results differ from theory

Influence of Zernike modes on fluorescence was not analyzed correctly

The effect of individual Zernike modes on total fluorescence was investigated theoretically (figure 2.5) and experimentally (5.13). The pupil size of the objective used in the experiment was a factor of 0.93 smaller than the pupil used in the calibration of the deformable mirror. This was done deliberately to ensure precise control of the wavefront at the edge of the objective pupil. However, it was neglected to correct for the differing pupil radius by rescaling the Zernike coefficients according to [10]. The result is that the actual aberrations applied over the objective pupil radius in the experiment are smaller by a factor of 0.86 (second order) to 0.63 (sixth order) than claimed, and that they also contained some contribution of lower order order aberrations of the same angular order. While the former effect increases the discrepancy between the shapes of the experimental and theoretical curves, the latter effect could possibly compensate this.

Even though quantitative comparisons between both curves are not possible in the current presentation, it is remarkable that the experimentally found split of modes into two groups with strong and weak influence on total fluorescence is also found in the theoretical simulations. These groups do not, however, correspond directly to different radial orders. Instead, modes with radial order at least 5, but angular order of at most 4 belong to the group with strong influence on fluorescence.

Experimentally optimal aberration correction means under-correction

As summarized in the table on page 84, the experimentally determined optima for spherical aberration and astigmatism determined in several different experiments are generally lower by a factor between 1.5 and 4 than the corresponding theoretical coefficients.

It can be seen that the measurement with the smallest theoretical coefficient estimate (effect of a single cover glass on spherical aberration, third row) shows the smallest discrepancy, suggesting that part of the problem might be a violated small-aberrations assumption.

This effect has already been mentioned in section 2.6, which is the cross-talk between different Zernike modes. The presence of uncorrected higher order spherical aberration causes non-zero lowest-order spherical aberration the improve (both peak and total) fluorescence. The assumption of independence of different Zernike modes is therefore violated for these large amounts of aberration.

While this effect of interdependence between modes had also been found experimentally when looking at the effect of defocus and spherical aberration (data not shown), it was originally attributed to deviations from the sine condition for excessive amounts of defocus, an effect suggested by the microscope manufacturer (Christian Schulz, Leica Microsystems – private communication).

There are other reasons which could explain why experimental optima are always smaller than theoretical predictions. Firstly, as has been shown in figure 5.9, the quality of wavefronts generated generally decreased with increasing coefficient values. Decreasing wavefront quality will decrease fluorescence, giving a bias towards less curved wavefronts, i.e. smaller coefficients.

Secondly, incorrect imaging of the wavefront sensor into the objective pupil or incorrect centering of both elements relative to each other could cause cross-talk between modes. If only some of these modes are optimized, this would also create an undetected bias towards smaller coefficients.

Another reason for discrepancy, as well as differences between different measurements, is the critical dependence of aberrations on the pupil radius over which the Zernike polynomials are defined[10].

6.5. Adaptive optics can improve fluorescence

There is no question that the system is capable of improving signal and z-resolution for samples creating large amounts of aberration. In figure 5.14, an improvement of fluorescence by 50% was achieved, in 5.15 by 60 to 150%, in 5.16 by 50%, in 5.18 by 100% in 5.19 by 50% in 5.20 by 90%. In figure 5.18 it is also clear that fluorescence is not restored completely to the unaberrated case, but this might in part be due to reflection of excitation and fluorescence light at the aberrating layer of glass used, as well as uncorrected higher order aberration modes.

6.6. Open questions

As can be seen from the discussion of results above, this project is still very much work in progress.

The characterization of the wavefront control in the experimental setup for wavefronts with multiple nonzero coefficients still needs to be performed, possibly replacing any extrapolation from voltages with interpolation. Characterization of performance in oscillation mode also has to be repeated. Both measurements were originally done with too lax a criterion for good wavefront control.

Zernike modes were found to be incorrectly balanced. Therefore, new aberration basis modes need to be determined, experimentally or theoretically, which have independent influence on fluorescence in the aberration range relevant. This will make non-iterative optimization of the correction values of different orders of the same aberration possible and allow comparison of theoretically calculated aberration coefficients with values found experimentally.

Calculations for the point spread function should be repeated with the full vectorial theory, to have more reliable theory curves against which to test experimental data.

Both microscope objectiv manufacturers (Zeiss and Leica) cautioned[2] that it might not be straightforward to treat their objectives as perfect sine condition objectives to calculate the correction coefficients necessary to optimize the point spread function. Leica suggested to enter the Olympus or Zeiss 20x objective patents into an optical systems design software like ZEMAX to more correctly approximate the behavior of these objectives. Apart from doing such a calculation ourselves, a cooperation with one of the objective manufacturers might be a possibility, to have them perform the necessary calculations for us.

A second issue in terms of description of the objective arises from the fact that at least the Leica objective is not completely corrected by itself, but only together with the corresponding tube and scan lenses. Since a Leica scan lens and a Nikon scan lens were used in the current setup, this could result in a systematic error. Of course the effect of scan and tube lens could be quantified by comparing the wavefront measurement in the wavefront sensor “objective” and “pre-microscope” positions for several different fixed shapes of the deformable mirror. This would allow to estimate the order of magnitude of this effect. If a significant effect is found, the question would remain open whether the correct scan and tube lens would not produce a significantly different effect. The only way to find out would be to use the correct lens combination, i.e. all three lenses from the same manufacturer.

---

[2] private communication with Ulrich Kühnapfel and Ulrich Kohlhaas, Carl Zeiss MicroImaging GmbH, as well as Christian Schulz, Leica Microsystems CMS GmbH

A. Zernike Polynomials

Every author laments over the variety of Zernike polynomial numbering schemes in use. An overview is given in table A.1.

In this lab, Noll [27] has been followed so far[17, 32], who was the first to suggest orthogonal, but non-orthonormal Zernike polynomials where the variance had been normalized. His single-index numbering scheme j_{Noll} is given here for comparison.

However, the wavefront sensor used in this project uses the single index numbering scheme $r_{Malacara}$ from [23], combined with the Noll normalization (Jürgen Hartmann, Thorlabs Inc, private communication). For convenience, this scheme was followed here. Theory papers from Oxford tend to use yet another single index scheme i_{Neil} [25], which is essentially the Noll style, except swapping some of terms which are identical to each other up to a 45° rotation. For these pairs of polynomials, Neil et al. chose to put the Cosine version first, whereas Noll chose to always give Cosine terms even indices.

Apart from the single index numbering schemes, the double index numbering also shows slight variations. While everyone agrees on the radial order index n, the azimuthal frequency index m comes in three versions:

$$-m_{Neil} = n_{Malacara} - 2m_{Malacara}$$

$$m_{Noll} = |m_{Neil}|$$

j_{Noll}	$r_{Malacara}$	i_{Neil}	**n**	m_{Neil}	$m_{Malacara}$	**Zernike Mode (Noll Norm)**
1	1	1	0	0	0	1
2	3	2	1	1	1	$2\rho\cos\theta$
3	2	3	1	-1	0	$2\rho\sin\theta$
4	5	4	2	0	1	$\sqrt{3}(-1+2\rho^2)$
5	4	6	2	-2	0	$\sqrt{6}\rho^2\sin 2\theta$
6	6	5	2	2	2	$\sqrt{6}\rho^2\cos 2\theta$
7	8	8	3	-1	1	$2\sqrt{2}(-2\rho+3\rho^3)\sin\theta$
8	9	7	3	1	2	$2\sqrt{2}(-2\rho+3\rho^3)\cos\theta$
9	7	10	3	-3	0	$2\sqrt{2}\rho^3\sin 3\theta$
10	10	9	3	3	3	$2\sqrt{2}\rho^3\cos 3\theta$
11	13	11	4	0	2	$\sqrt{5}(1-6\rho^2+6\rho^4)$
12	14	12	4	2	3	$\sqrt{10}(-3\rho^2+4\rho^4)\cos 2\theta$
13	12	13	4	-2	1	$\sqrt{10}(-3\rho^2+4\rho^4)\sin 2\theta$
14	15	14	4	4	4	$\sqrt{10}\rho^4\cos 4\theta$
15	11	15	4	-4	0	$\sqrt{10}\rho^4\sin 4\theta$
16	19	16	5	1	3	$2\sqrt{3}(3\rho-12\rho^3+10\rho^5)\cos\theta$
17	18	17	5	-1	2	$2\sqrt{3}(3\rho-12\rho^3+10\rho^5)\sin\theta$
18	20	18	5	3	4	$2\sqrt{3}(-4\rho^3+5\rho^5)\cos 3\theta$
19	17	19	5	-3	1	$2\sqrt{3}(-4\rho^3+5\rho^5)\sin 3\theta$
20	21	20	5	5	5	$2\sqrt{3}\rho^5\cos 5\theta$
21	16	21	5	-5	0	$2\sqrt{3}\rho^5\sin 5\theta$
22	25	22	6	0	3	$\sqrt{7}(-1+12\rho^2-30\rho^4+20\rho^6)$
23	24	24	6	-2	2	$\sqrt{14}(6\rho^2-20\rho^4+15\rho^6)\sin 2\theta$
24	26	23	6	2	4	$\sqrt{14}(6\rho^2-20\rho^4+15\rho^6)\cos 2\theta$
25	23	26	6	-4	1	$\sqrt{14}(-5\rho^4+6\rho^6)\sin 4\theta$
26	27	25	6	4	5	$\sqrt{14}(-5\rho^4+6\rho^6)\cos 4\theta$
27	22	28	6	-6	0	$\sqrt{14}\rho^6\sin 6\theta$
28	28	27	6	6	6	$\sqrt{14}\rho^6\cos 6\theta$

Table A.1. – Zernike Modes up to 6th radial order with different numbering schemes

Bibliography

[1] A. Ascenzi and C. Fabry. Technique for dissection and measurement of refractive index of osteones. *J. Biophys. and Biochem. Cytol.*, 6(1):139–142, 1959.

[2] F. P. Bolin, L. E. Preuss, R. C. Taylor, and R. J. Ference. Refractive-index of some mammalian-tissues using a fiber optic cladding method. *Applied Optics*, 28(12):2297–2303, 1989.

[3] M. Booth and T. Wilson. Strategies for the compensation of specimen-induced spherical aberration in confocal microscopy of skin. *J. Microsc.*, 200(1):68–74, 2000.

[4] M. Booth, T. Wilson, H. B. Sun, T. Ota, and S. Kawata. Methods for the characterization of deformable membrane mirrors. *Applied Optics*, 44(24):5131–5139, 2005.

[5] M. J. Booth. Adaptive optics in microscopy. *Philosophical Transactions of the Royal Society a-Mathematical Physical and Engineering Sciences*, 365(1861):2829–2843, 2007.

[6] M. J. Booth, M. A. A. Neil, and T. Wilson. Aberration correction for confocal imaging in refractive-index- mismatched media. *Journal of Microscopy-Oxford*, 192:90–98, 1998.

[7] M. J. Booth and T. Wilson. Refractive-index-mismatch induced aberrations in single-photon and two-photon microscopy and the use of aberration correction. *Journal of Biomedical Optics*, 6(3):266–272, 2001.

[8] M. Born and E. Wolf. *Principles of Optics.* Cambridge University Press, Cambridge, U.K., 7th (expanded) edition edition, 1999.

[9] E. Botcherby, R. Juskaitis, M. Booth, and T. Wilson. An optical technique for remote focusing in microscopy. *Optics Communications*, 281(4):880–887, 2008.

[10] G. Dai. Scaling zernike expansion coefficients to smaller pupil sizes: a simpler formula. *Journal of the Optical Society of America A*, 23(3):539–543, 2006.

[11] D. Débarre, E. J. Botcherby, M. J. Booth, and T. Wilson. Adaptive optics for structured illumination microscopy. *Opt. Express*, 16(13):9290–9305, 2008.

[12] W. Denk. Optical beam power controller using a tiltable birefringent plate (patent no. 6249379), 2001.

[13] W. Denk, J. H. Strickler, and W. W. Webb. Two-photon laser scanning fluorescence microscopy. *Science*, 248(4951):73–76, 1990.

[14] A. Dubra. Wavefront sensor and wavefront corrector matching in adaptive optics. *Optics Express*, 15(6):2762–2769, 2007.

[15] A. Egner and S. W. Hell. Equivalence of the huygens-fresnel and debye approach for the calculation of high aperture point-spread functions in the presence of refractive index mismatch. *Journal of Microscopy*, 193(3):244–249, 1999.

[16] T. Euler, S. Hausselt, D. Margolis, T. Breuninger, X. Castell, P. Detwiler, and W. Denk. Eyecup scope – optical recordings of light stimulus-evoked fluorescence signals in the retina. *Pflügers Arch./Europ. J. Physiol.*, under revision, 2008.

[17] M. Feierabend. Coherence-gated wave-front sensing in strongly scattering samples. *phd thesis*, 2004.

[18] K. B. J. Franklin and G. Paxinos. *The Mouse Brain in stereotaxic coordinates.* Elsevier, Amsterdam, 3rd ed. edition, 2008.

[19] S. W. Hell, G. Reiner, C. Cremer, and E. H. K. Stelzer. Aberrations in confocal fluorescence microscopy induced by mismatches in refractive index. *Journal of Microscopy*, 169:391–405, 1993.

[20] J. Lai, Z. Li, C. Wang, and A. He. Experimental measurement of the refractive index of biological tissues by total internal reflection. *Applied Optics*, 44(10):1845–1849, 2005.

[21] N. Lue, J. Bewersdorf, M. D. Lessard, K. Badizadegan, R. R. Dasari, M. S. Feld, and G. Popescu. Tissue refractometry using hilbert phase microscopy. *Opt. Lett. Optics Letters*, 32(24):3522–3524, 2007.

[22] W. Lukosz. Der einfluß der aberrationen auf die optische Übertragungsfunktion bei kleinen orts-frequenzen. *Journal of Modern Optics*, 10(1):1 – 19, 1963.

[23] D. Malacara. *Optical Shop testing.* Wiley Series in Pure and Applied Optics. John Wiley & Sons, Inc., New York, second edition, 1992.

[24] G. e. Müller and A. e. Roggan. *Laser-Induced Interstitial Thermotherapy*, volume PM25. SPIE, Bellingham, WA, 1995.

[25] M. A. Neil, M. J. Booth, and T. Wilson. New modal wave-front sensor: a theoretical analysis. *J Opt Soc Am A Opt Image Sci Vis*, 17(6):1098–107, 2000.

[26] M. A. A. Neil, R. Juskaitis, M. J. Booth, T. Wilson, T. Tanaka, and S. Kawata. Adaptive aberration correction in a two-photon microscope. *Journal of Microscopy-Oxford*, 200:105–108, 2000.

[27] R. J. Noll. Zernike polynomials and atmospheric-turbulence. *Journal of the Optical Society of America*, 66(3):207–211, 1976.

[28] B. Patterson. Circular and annular zernike polynomials for mathematica, 2002.

[29] J. B. E. Pawley. *Handbook of biological confocal microscopy.* Handbook of biological confocal microscopy. Springer, New York, NY, 3. ed. edition, 2006.

[30] B. Rappaz, P. Marquet, E. Cuche, Y. Emery, C. Depeursinge, and P. Magistretti. Measurement of the integral refractive index and dynamic cell morphometry of living cells with digital holographic microscopy. *Opt. Express Optics Express*, 13(23):9361–9373, 2005.

[31] B. Richards and E. Wolf. Electromagnetic diffraction in optical systems .2. structure of the image field in an aplanatic system. *Proceedings of the Royal Society of London Series a-Mathematical and Physical Sciences*, 253(1274):358–379, 1959.

[32] M. Rueckel. *Adaptive wavefront correction in two-photon microscopy using coherence-gated wavefront sensing.* Phd-thesis, Ruperto-Carola University of Heidelberg, 2006.

[33] M. Rueckel, J. A. Mack-Bucher, and W. Denk. Adaptive wavefront correction in two-photon microscopy using coherence-gated wavefront sensing. *Proceedings of the National Academy of Sciences of the United States of America*, 103(46):17137–17142, 2006.

[34] M. Schwertner, M. J. Booth, and T. Wilson. Simulation of specimen-induced aberrations for objects with spherical and cylindrical symmetry. *Journal of Microscopy-Oxford*, 215:271–280, 2004.

[35] C. Sheppard and C. Cogswell. Effects of aberrating layers and tube length on confocal imaging properties. *Optik(Stuttgart)*, 87(1):34–38, 1991.

[36] C. J. R. Sheppard and M. Gu. Aberration compensation in confocal microscopy. *Applied Optics*, 30(25):3563–3568, 1991.

[37] G. J. Tearney, M. E. Brezinski, J. F. Southern, B. E. Bouma, M. R. Hee, and J. G. Fujimoto. Determination of the refractive-index of highly scattering human tissue by optical coherence tomography. *Optics Letters*, 20(21):2258–2260, 1995.

[38] P. Theer. *On the fundamental imaging-depth limit in two-photon microscopy.* Phd-thesis, Ruperto-Carola University of Heidelberg, 2004.

[39] P. Theer and W. Denk. On the fundamental imaging-depth limit in two-photon microscopy. *Journal of the Optical Society of America a-Optics Image Science and Vision*, 23(12):3139–3149, 2006.

[40] P. Theer, M. T. Hasan, and W. Denk. Two-photon imaging to a depth of 1000 mu m in living brains by use of a ti : Al2o3 regenerative amplifier. *Optics Letters*, 28(12):1022–1024, 2003.

[41] J. Tritthardt. *Entwicklung der Aufnahmeelektronik eines Laser-Scanning-Mikroskops.* diploma thesis, Fern-Universität-Gesamthochschule Hagen, 2002.

[42] P. Török, P. Varga, Z. Laczik, and G. R. Booker. Electromagnetic diffraction of light focused through a planar interface between materials of mismatched refractive-indexes - an integral-representation. *Journal of the Optical Society of America a-Optics Image Science and Vision*, 12(2):325–332, 1995.

[43] A. van den Bos. Aberration and the strehl ratio. *Journal of the Optical Society of America a-Optics Image Science and Vision*, 17(2):356–358, 2000.

[44] T. e. Vo-Dinh. *Biomedical Photonics Handbook.* CRC Press, Boca Raton, 2003.

Danksagung

Ich möchte mich bei Herrn Professor Dr. Winfried Denk bedanken, von dem ich im vergangenen Jahr sehr viel gelernt habe, unter anderem den Weitblick zu behalten.

Wolfgang Mittmann danke ich für die gute Zusammenarbeit auf dem gemeinsamen Projekt, auch wenn der Laser nicht immer nett zu uns war.

Markus Rückel und Patrick Theer, die mir in der Optik zu etwas mehr Durchblick verholfen haben, und immer als telefonische Feuerwehr zur Verfügung standen.

Christa Hörner-Ehm, die besser als sonst irgendwer den Überblick behält und bei Problemen immer Rat weiß. Wenn sie das Problem nicht schon vor einem selbst erkannt und behoben hat...

Jürgen Tritthardt und Michael Müller, die beide eine unüberschaubare Zeit damit zugebracht haben, meine Sonderwünsche an Elektronik- und Softwaremodulen zu befriedigen.

Manfred Hauswirth und sein Werkstatt-Team, ohne die so manches Bauteil des Mikroskops durchsichtig wie Klebeband wäre.

Ramon Granadillo, Stefanie Terbeck, Wulf Kaiser and particularly Chris Roome for digging up any computer part, book or CD I asked for, where ever in Germany they could find it.

Soojin Ryu and Andrea Dörfel for supplying zebrafish for some in-vivo tests.

Christian Schulz (Leica), Ulrich Kohlhaas (Zeiss) und Jürgen Hartmann (Thorlabs), die mir am Telefon oder per E-Mail viel geholfen haben, ihre Produkte besser zu verstehen.

Falko, Thomas, Gesa, Jan Uwe und Steffi, die für mein Gleichgewicht sorgen.

Camille, mon bonheur.

Meinen Eltern, der besten WG-Besetzung der Welt.

Allen Mensagängern der BMO. Morgen, 12:05 Uhr an der Pforte?

Erklärung

Ich versichere, dass ich diese Arbeit selbständig verfasst und keine anderen als die angegebenen Quellen und Hilfsmittel benutzt habe.

Heidelberg, den 15. Oktober 2008 ______________________________

Jonas Binding